

MODELING THE EFFECTS OF GEOLOGIC HETEROGENEITY AND
METAMORPHIC DEHYDRATION ON SLOW SLIP AND SHALLOW
DEFORMATION IN SUBDUCTION ZONES

by

ROBERT M. SKARBEEK

A DISSERTATION

Presented to the Department of Geological Sciences
and the Graduate School of the University of Oregon
in partial fulfillment of the requirements
for the degree of
Doctor of Philosophy

June 2015

DISSERTATION APPROVAL PAGE

Student: Robert M. Skarbek

Title: Modeling the Effects of Geologic Heterogeneity and Metamorphic Dehydration on Slow Slip and Shallow Deformation in Subduction Zones

This dissertation has been accepted and approved in partial fulfillment of the requirements for the Doctor of Philosophy degree in the Department of Geological Sciences by:

Alan Rempel	Chair
John Logan	Core Member
David Schmidt	Core Member
John Toner	Institutional Representative

and

Scott L. Pratt	Dean of the Graduate School
----------------	-----------------------------

Original approval signatures are on file with the University of Oregon Graduate School.

Degree awarded June 2015

© 2015 Robert M. Skarbek

DISSERTATION ABSTRACT

Robert M. Skarbek

Doctor of Philosophy

Department of Geological Sciences

June 2015

Title: Modeling the Effects of Geologic Heterogeneity and Metamorphic Dehydration on Slow Slip and Shallow Deformation in Subduction Zones

Slow slip and tectonic tremor in subduction zones take place at depths (~ 20 - 50 km) where there is abundant evidence for distributed shear over broad zones (~ 10 - 10^3 m) composed of rocks with marked differences in mechanical properties and for near lithostatic pore pressures along the plate interface where the main source of fluids must be attributed to chemical dehydration reactions. In Chapter II, I model quasi-dynamic rupture along faults composed of material mixtures characterized by different rate-and-state-dependent frictional properties to determine the parameter regime capable of producing slow slip in an idealized subduction zone setting. Keeping other parameters fixed, the relative proportions of velocity-weakening (VW) and velocity-strengthening (VS) materials control the sliding character (stable, slow, or dynamic) along the fault. The stability boundary between slow and dynamic is accurately described by linear analysis of a double spring-slider system with VW and VS blocks. In Chapter III, I model viscoelastic compaction of material subducting through the slow slip and tremor zone in the presence of pressure and temperature-dependent dehydration reactions. A dehydration fluid source is included

using 1) a generalized basalt dehydration reaction in subducting oceanic crust or 2) a general nonlinear kinetic reaction rate law parameterized for an antigorite dehydration reaction. Pore pressures in excess of lithostatic values are a robust feature of simulations that employ parameters consistent with the geometry of the Cascadia subduction margin. Simulations that include viscous deformation uniformly generate traveling porosity waves that transport increased fluid pressures within the slow slip region. Slow slip and tremor also occur in shallow (< 10 km depth) accretionary prism sections of subduction zones. In Chapter IV, I examine how geologic heterogeneities affect the mechanics of accretionary prisms in subduction zones by showing how spatial variations in pore pressure, porosity, and internal friction coefficient affect predictions of basal shear stress, taper angle, and internal slip surface geometry. My results suggest that assuming average porosity throughout the prism may be a good approximation in many cases, but assuming an average value for the pore pressure can cause significant errors.

This dissertation includes previously published and unpublished coauthored material.

CURRICULUM VITAE

NAME OF AUTHOR: Robert M. Skarbek

GRADUATE AND UNDERGRADUATE SCHOOLS ATTENDED:

University of Oregon, Eugene, OR
Penn State University, State College, PA

DEGREES AWARDED:

Doctor of Philosophy, Geological Sciences, 2015, University of Oregon
Master of Science, Geosciences, 2008, Penn State University
Bachelor of Science, Physics, 2006, Penn State University

AREAS OF SPECIAL INTEREST:

Mechanics of Subduction Zones

PUBLICATIONS:

Skarbek, R. M. and Rempel, A. W. (2013). Thermal consolidation with chemical dehydration reactions: Pore pressure generation in the slow slip region of subduction zones. C. Hellmich, B. Pichler, & D. Adam (Eds.), *Poromechanics V: Proceedings of the Fifth Biot Conference on Poromechanics* (pp. 499-506). American Society of Civil Engineers, Reston, VA.

Skarbek, R. M., Rempel, A. W., & Schmidt, D. A. (2012). Geologic heterogeneity can produce aseismic slip transients. *Geophys. Res. Lett.*, 39.

Skarbek, R. M. and Saffer, D. M. (2009). Pore pressure development beneath the decollement at the Nankai subduction zone: Implications for plate boundary fault strength and sediment dewatering. *J. Geophys. Res.*, 114.

TABLE OF CONTENTS

Chapter	Page
I. INTRODUCTION	1
II. GEOLOGIC HETEROGENEITY CAN PRODUCE ASEISMIC SLIP TRANSIENTS	6
2.1. Introduction	6
2.2. Methods	8
2.3. Results and Discussion	14
2.4. Double Spring-Slider System	17
2.5. Conclusions	22
2.6. Linear Stability of a Two Block Spring-Slider System	23
2.7. Bridge	30
III. GENERATION AND TRANSPORT OF EXCESS FLUID PRESSURE BY DEHYDRATION REACTIONS IN THE SLOW SLIP REGION OF SUBDUCTION ZONES	31
3.1. Introduction	31
3.2. Model Overview	35
3.3. Elastic Limit and Prescribed Dehydration	44
3.4. Viscous Limit and Reaction Kinetics	53
3.5. Discussion and Conclusion	74
3.6. Model Derivation	76

Chapter	Page
3.7. Bridge	85
 IV. HETEROGENEOUS COULOMB WEDGES: INFLUENCE OF PORE PRESSURE, POROSITY, AND INTERNAL FRICTION	 87
4.1. Introduction	87
4.2. Wedge Analysis	89
4.3. Results	92
4.4. Conclusions	106
4.5. Model Derivation	108
4.6. Simplified Solutions	114
4.7. Proofs	118
 V. CONCLUSION	 127
 REFERENCES CITED	 130

LIST OF FIGURES

Figure	Page
<p>2.1. (a) Model geometry for a simplified two-dimensional subduction zone, the free surface is not included in the model. (b) Boundary conditions along the subduction plate-boundary fault. (c) Frictional parameters along the fault.</p>	10
<p>2.2. Normalized maximum sliding velocities from simulations with $W/h^* = 6$ and $(a/b)_{vs} = 1.05$. Each point on the graph represents an individual simulation; with different symbols referring to the values of η indicated in the legend. Vertical bars show the onset of dynamic sliding for each η. Horizontal bars along the x-axis delineate values of $(a/b)_{vw}$ that produce periodic slow events, which are shown in the lower panel. Higher values of $(a/b)_{vw}$, relative to horizontal bars for a given value of η, produce steady sliding and are not shown. In order to illustrate the model behavior, maximum slip velocities are included in the upper panel from simulations that produced dynamic sliding events; however, we note that the absolute magnitude (but not the dynamic behavior) of dynamic slip velocities is only approximated by our modeling procedure.</p>	13
<p>2.3. (a) Static stress drop $\Delta\tau$ and (b) propagation velocity v_{prop} for slow events from simulations with scaled fault length $W/h^* = 6$ and velocity-strengthening component characterized by $(a/b)_{vs} = 1.05$, with the values of η noted in the legend. Each point represents an individual event from the simulations presented in Figure 2.2 of the main text. Note that multiple events occurred during each simulation (i.e. points with identical $(a/b)_{vw}$).</p>	15
<p>2.4. Normalized maximum sliding velocities from simulations with $(a/b)_{vw} = 0.8$ and $(a/b)_{vs} = 1.05$. Each point represents a different simulation, using values of η chosen to search for the sliding behavior transitions, with the onset of dynamic events marked by the vertical colored lines. The corresponding colored symbols mark simulations run with the different values of W/h^* that are noted in the legend. Bars along the x-axis delineate ranges of η that produce periodic slow events.</p>	18
<p>2.5. Schematic illustration of a double, spring-block slider system, with spring constants k_1 and k_2 and load-point velocity v_0.</p>	19

Figure	Page
2.6. Stability field for double spring-slider system. The solid line indicates the stable-unstable boundary; the dashed line indicates this boundary for $k_2 \rightarrow \infty$ from equation (5). The motion of the blocks is stable when k_1 is greater than the critical value shown by the solid black line. The discontinuity where the two stability conditions overlap marks the minimum stability condition that is plotted with the solid curve on Figure 2.7; the dotted lines show the extension of each stability condition to stiffnesses that are beneath the critical stability predicted by the other condition. $\sigma = 240$ kPa, $(a/b)_{vw} = 0.83$, $(a/b)_{vs} = 1.05$, $d_c = 40$ μ m, and $\eta = 0.6$	20
2.7. Stability field for elastic model. For the elastic model, slow sliding events occur within the gray shaded region, unstable (stable) sliding occurs below (above) this region. The dashed black line marks the stability boundary predicted by equation (6) (i.e. k_{1crit}^∞) and corresponds to the dashed line in Figure 2.6. The solid black line marks the theoretical stability boundary calculated by methods discussed in the text and the auxiliary information. The red cross marks the location of the point $(k_{2crit}^{min}, k_{1crit}^{min})$ from Figure 2.6.	21
3.1. Subduction of a column of rock (black and green grids) is initiated at a known depth below the locked zone. Material crossing the equilibrium boundary (red line, green grid points) of a relevant dehydration reaction loses its chemically bound water at a prescribed rate, or at a rate controlled by the local offset from the equilibrium curve in $p - T$ space.	39
3.2. Pressure-temperature space showing the location of a generalized reaction boundary (red line), estimated from <i>Fagereng and Diener (2011)</i> for the breakdown of chlorite and glaucophane to form hornblende and epidote, and the equilibrium boundaries for reaction (3.11) (black dashed line) and the shifted reaction (solid black line). The blue shaded region shows the path of the subducting column path assuming lithostatic pore pressure and temperature as described in the text.	43
3.3. Pressure profiles for three values of permeability and values of Γ indicated by the legends. The colors in panel (b) correspond to those in panel (c). All simulations were run for 14 months, with hydrostatic initial conditions, a hydrostatic upper boundary, and a no-flow lower boundary. Hydrostatic and lithostatic pressure profiles are shown by the dashed and solid black lines.	49

Figure	Page
3.4. Results for simulations varying the permeability of the column k_0 as well as that of the cap k_{cap} . In all simulations shown here the cap thickness is set to $z_{\text{cap}} = 10$ m. Colored lines show the minimum depth below the upper boundary to negative effective stress within the subducting column. The grey shaded region shows the fraction of the column that has crossed the reaction boundary and dewatered.	51
3.5. Results for simulations varying the permeability of the column k_0 and the thickness of the cap z_{cap} . In all simulations shown here the cap permeability is set to $k_{\text{cap}} = 10^{-24}$ m ² . Colored lines show the minimum depth below the upper boundary to negative effective stress within the subducting column. The grey shaded region shows the fraction of the column that has crossed the reaction boundary and dewatered.	52
3.6. Plot of the relationship, equation (3.27), between permeability and viscosity for a compaction time $\tau_0 = 1$ year. The grey shaded region shows this relationship for porosities 0.01 to 0.1. The blue shaded region shows viscosities calculated using the results of <i>Hilairret et al.</i> (2007), for strain rates corresponding to plate interface thicknesses of 1 to 1000 m.	58
3.7. Evolution of a porosity step at $z = 80$ for (a) $\phi_1 = 0.2$ and (b) $\phi_1 = 0.8$. Viscous resistance to volume changes causes the initial step to propagate as a dispersive train of solitary waves. Panels (a) and (b) show porosity profiles with increasing time. The separation between adjacent profiles corresponds to a porosity of 1.5 (a) and 0.2 (b). (c) Contours of the pressure anomaly $z - p_{\text{tot}}$ for $\phi_1 = 0.8$, for comparison with Figure 3.10.	60
3.8. Initial profiles of effective pressure p_e (blues lines), fluid flux q (red lines), and $\partial\phi/\partial t$ (green lines), for the initial porosity profiles shown by the black lines.	62
3.9. (a) Amplitude of dispersive wavetrains as a function of the porosity step ϕ_1 . Circles and squares show the maximum and mean amplitudes, respectively, of the leading porosity wave. The dashed line is the amplitude predicted by the physical argument relating to the McKenzie equations, the solid line is the same predicted for the system considered here (equation (3.47)). (b) Phase velocity of the leading porosity wave as a function of the amplitudes shown in panel (a). The dashed line corresponds to the dispersion relation given by equation (3.40), the solid line shows the prediction of the dispersion relation given by equation (3.54), both appropriately re-scaled. Green circles and squares show the maximum and mean amplitude of the leading wave for simulations that include dehydration.	66

3.10. Evolution of initially uniform (a) porosity and (b) pressure anomaly for a simulation including dehydration with $\lambda K = 12.5$. The separation between adjacent profiles in panel (a) corresponds to a normalized porosity of 1.3. (c) The amount of released water m_d within the reaction zone for time $t = 75t_o$. This corresponds to the third porosity profile in panel (a). The horizontal black lines show the numerically determined reaction zone, defined by the depth where $\Delta G = 0$ and the depth where $m_d = 0.99m_d^0$	68
4.1. Coordinate system and cross section cartoon of a heterogeneous wedge.	90
4.2. (a) Normalized basal shear stress resulting from a linear increase in pore pressure ratio with depth (solid line), compared with that for the depth-averaged state (dashed line), and (b) the corresponding correction. Other parameters: $\alpha = 2^\circ, \beta = 3^\circ, \bar{\phi} = 0.3, \bar{\mu} = 0.6$	99
4.3. (a) Normalized basal shear stress over the frontal 30 km resulting from an exponential decrease in porosity with depth (solid line), compared with that for the depth-averaged state (dashed line), and (b) the corresponding correction for a single wedge calculation with $b = 6.5 \times 10^{-4} \text{ m}^{-1}$. (c) Normalized basal shear stress averaged over the frontal 30 km for the exponential (solid line) and depth-averaged (dashed line) states and (d) the corresponding correction. The boxes correspond to the simulation shown in (a) and (b). Other parameters: $\alpha = 2^\circ, \beta = 3^\circ, \bar{\lambda} = 0.5, \bar{\mu} = 0.6$	102
4.4. Corrections to the equilibrium basal dip angle resulting from (a) linear pore pressure with $\bar{\phi} = 0.3$, and (b) exponential porosity with $\bar{\lambda} = 0.5$. Other parameters: $\alpha = 2^\circ, \beta = 3^\circ, \bar{\mu} = 0.6$	103
4.5. Example equilibrium wedge profiles and slip surfaces for linear pore pressure ratio (blue lines $\beta = 4.5^\circ, \lambda_b = 0.9, \bar{\phi} = 0.3$) and exponential porosity (red lines $\beta = 3.6^\circ, b = 6.6 \times 10^{-4} \text{ m}^{-1}, \bar{\lambda} = 0.5$). Black lines show the corresponding depth-averaged state $\alpha = 2^\circ, \bar{\beta} = 3^\circ, \bar{\lambda} = 0.5, \bar{\phi} = 0.3, \bar{\mu} = 0.6$	105

LIST OF TABLES

Table	Page
2.1. Nominal parameter values used in model simulations. Ranges are given for those parameters that are varied to explore the different regimes of model behavior.	11
3.1. Parameter definitions and nominal values used in model simulations. . . .	45
4.1. Symbols and definitions. Values are given only for parameters that are held constant throughout this paper. Other parameter values are assigned in the text where appropriate.	91

CHAPTER I

INTRODUCTION

The discovery of slow slip phenomena has revealed that the majority of fault zones worldwide are capable of accommodating deformation through multiple mechanisms that occur over a range of timescales, with different sensitivities to local conditions and properties (*Beroza and Ide, 2011*). These events have broadened the spectrum of fault slip observed by geodetic and seismic instruments, and introduced a new set of research questions for the scientific community to pursue. As a testament to the ubiquitous nature of the underlying processes, slow transient events have now been documented on most subduction zones around the world, as well as in other tectonic settings, including segments along the San Andreas fault and in Hawaii (*Schwartz and Rokosky, 2007*).

Episodic tremor and slip (ETS) occurs as large scale (~ 10 s of kilometers) aseismic deformation, accompanied by much smaller scale (~ 100 s of meters) low frequency earthquakes (LFEs). These events typically have slip velocities 10-100 times larger than the plate convergence rate, durations of days to months, and recurrence intervals of months to years. Slip and tremor in subduction zone environments typically propagate along the plate interface at velocities of ~ 10 km/day and are largely confined to the region known as the transition zone, located down-dip of the locked subduction thrust (*Beroza and Ide, 2011*).

In Cascadia, the transition zone is immediately down-dip of the area that is known to have ruptured in past $\sim M9$ earthquakes. It is currently unclear whether slip in future $M9$ events can penetrate into the region that regularly hosts slow slip events (SSEs). The depth extent of coseismic slip is of fundamental importance for ground

motion prediction and earthquake hazard because the transition zone is the part of the megathrust closest to the major population centers in the Pacific Northwest, such as Seattle and Portland, and will profoundly influence the ground motion that those regions experience (*Petersen et al.*, 2014). The existence of ETS indicates that brittle behavior extends into the transition zone. Additionally, both observational and theoretical evidence suggest that slow slip may play a role in triggering large megathrust earthquakes (*Segall and Bradley*, 2012; *Ito et al.*, 2013). Hence, a better understanding of the rheology and in-situ properties of the transition zone will lead to improved ground motion estimates and earthquake resilience in the Pacific Northwest.

Recent field (e.g. *Collettini et al.*, 2011; *Fagereng et al.*, 2011) and modeling studies (e.g. *Ando et al.*, 2010; *Nakata et al.*, 2011; *Skarbek et al.*, 2012) suggest that fault heterogeneity (e.g. a mixture of frictional velocity-weakening and velocity-strengthening materials, or similarly, a mixture of seismic and aseismic materials) along plate interfaces may be crucial to the generation of slow slip transients and tectonic tremor. In Chapter II, I model the effect of such heterogeneous features on slow slip by considering an idealized one-dimensional, elastic fault surface along the plate displacement direction, with spatially variable rate-and-state friction properties. This model represents a first-order, one-dimensional test of the dynamic implications of geologic heterogeneity in three-dimensional fault systems.

The model differs from previous studies by incorporating mixed frictional parameters along the fault surface that are manifest as alternating sections of VW and VS materials in the zone that hosts transient slip events. Linear analysis of a spring-slider system composed of two blocks in parallel, one with velocity-weakening (VW) and one with velocity-strengthening (VS) properties, provides an approximate prediction for the sliding stability of the elastic model. The results demonstrate how

different combinations of geological materials produce the full range of sliding styles that are observed along plate-bounding faults.

Slow slip phenomena are sensitive to extremely small stress changes. A number of studies have shown that tremor and LFEs respond to stress fluctuations on the order of 10 kPa associated with passing surface waves (*Rubinstein et al.*, 2007), 1 kPa loading from ocean tides (*Rubinstein et al.*, 2008), and < 1 kPa perturbations from solid earth tides (*Thomas et al.*, 2009). *Thomas et al.* (2009) showed that the tremor or LFE rate increases systematically with the magnitude of tidal shear stress that is aligned in the direction of slip. *Royer et al.* (2015) has also reported a significant correlation with tidally induced normal stress. Since tidal stress changes are extremely small relative to the expected lithostatic stress at the depths in question, a number of authors have proposed that tremor/LFE source regions are characterized by low effective stress (i.e. high pore pressure). Low effective stress is also implied by seismic data (e.g. *Audet et al.*, 2009), consistent with expected pore pressure changes produced by dehydration reactions (e.g. *Fagereng and Diener*, 2011), and is required by most models that successfully reproduce the first-order characteristics of slow slip behavior (e.g. *Segall et al.*, 2010; *Skarbek et al.*, 2012).

Despite the abundance of evidence for high fluid pressures in the slow slip zone, only a few studies have attempted to quantify the responsible processes (e.g. *Peacock*, 2009; *Fagereng and Diener*, 2011; *Katayama et al.*, 2012; *Poulet et al.*, 2014). In Chapter III, I attempt to quantify these processes by constructing a model for compaction of porous media in the presence of pressure and temperature-dependent dehydration reactions. There are two goals: 1) to test the feasibility of generating lithostatic pore pressures in a realistic model that includes dehydration reactions in a physical way, and 2) to examine the possibility that the observed periodicity of slow

slip and tremor can be explained by the wave-like migration of pressure and porosity in the plate interface. In this scenario, excess fluid pressure induced by dehydrating rocks propagates as a porosity wavetrain. I test the hypothesis that increased pressure at the plate interface, corresponding to a peak in a traveling porosity wave, triggers a slow slip or tremor event.

Recent observations in Japan have documented the occurrence of tremor and slow slip in subduction zone accretionary prisms and along the plate interface at depths <10 km, above the seismogenically locked zone (*Ito and Obara, 2006a,b; Ando et al., 2012; Sugioka et al., 2012*). As with the occurrence of ETS at depths below the locked zone, this shallow behavior has been associated with high fluid pressures and mechanical heterogeneity (*Kitajima and Saffer, 2012; Sugioka et al., 2012; Saito et al., 2013*). The stress state and properties of accretionary prisms define the background against which shallow tremor and slow slip take place, and so are of primary importance to understanding ETS behavior overall.

In Chapter IV, I employ a mechanical model of a submarine accretionary wedge to investigate how internal heterogeneity affects calculations of basal shear stress, taper angle, and internal slip surface geometry (i.e. faults that step-up from the basal surface). These are all key unknown parameters in areas where shallow slow slip and tremor are known to occur. There is now a large amount of data that characterizes the internal state and geometry of the Nankai accretionary prism in southwest Japan (e.g. *Tobin and Kinoshita, 2006*). Additionally, a large-scale scientific drilling project is being planned for the Hikurangi margin in New Zealand (*Wallace et al., 2011*). The model that I develop in Chapter IV is designed to exploit the data sets associated with these projects.

Together, these chapters represent an effort to develop geophysical theories that can explain the characteristics of slow slip and tremor in subduction zones. Care has been taken to ground these theories in geologic reality by making use of observations from assemblages of rocks that represent fossilized subduction zones. My intent has been to contribute towards the understanding of subduction zone plate boundaries in as useful a fashion as possible.

Each chapter has reached a different stage in the publication process. Chapter II was published in *Geophysical Research Letters* in 2012 and was co-authored by my advisor, Alan Rempel and my co-advisor at the time, David Schmidt (now at the University of Washington). Alan and David provided me with scientific and philosophical, as well as editorial, guidance. Chapters III and IV are in preparation for submission to the *Journal of Geophysical Research* and are also co-authored by Alan. Finally, a very preliminary form of the work described in Chapter III was published in the *Proceedings of the Fifth Biot Conference on Poromechanics* in 2013, again co-authored by Alan and myself.

CHAPTER II

GEOLOGIC HETEROGENEITY CAN PRODUCE ASEISMIC SLIP TRANSIENTS

This chapter was published in volume 39 of *Geophysical Research Letters* in November, 2012. I performed all of the calculations and wrote the manuscript. Alan Rempel and David Schmidt provided scientific and philosophical guidance and helped with the manuscript.

2.1. Introduction

In subduction zones, there is abundant evidence from laboratory experiments (*Hirth and Tullis, 1992; Dimanov and Dresen, 2005; Mehl and Hirth, 2008*), seismic data (*Eberhart-Phillips and Reyners, 1999; Martin and Rietbrock, 2006; Tsuji et al., 2008*), and field observations (*Bebout and Barton, 2002; Meneghini et al., 2009*) suggesting that, under *in situ* conditions, shear is distributed over broad zones ($\sim 10\text{--}10^3$ m) composed of rocks with marked differences in mechanical properties. Prior to the discovery of slow-slip events, a considerable body of work had documented the structure of the deformation zone beneath seismogenic depths. *Shreve and Cloos (1986)* developed a model that predicts the fate of subducted sediments and the formation of a heterogeneous *mélange* along the plate interface. *Cloos and Shreve (1988)* further expanded upon these ideas to discuss how such a "subduction channel" might act as a lubricant and facilitate motion of the down-going plate. *Fagereng and Sibson (2010)* give a concise summary of evidence for a "subduction channel shear zone" (defined here as a shear zone within subducted sediments) in which the style of deformation is determined by the relative abundance and distribution

of competent (i.e. brittle or non-compliant) and incompetent (ductile or compliant) material. Efforts to understand the physical interactions that produce aseismic transients (slow slip) must account for the effects of this geological heterogeneity.

Here, we model the features of such subduction channel shear zones by considering an idealized one-dimensional fault surface along the displacement direction, with spatially variable rate-and-state friction properties. Field observations suggest that two- and three-dimensional variations in the shapes of brittle phacoids have a significant effect on the style of deformation (*Fagereng, 2011*). Our model represents a first-order, one-dimensional test of the dynamic implications of geologic heterogeneity in three-dimensional fault systems.

Sustaining aseismic transients over fault lengths comparable to those inferred for subduction zones (tens of kilometers) has been a central challenge for models of slow slip and tremor. Recent studies have achieved this goal by using features of rate-and-state friction near neutral stability (*Liu and Rice, 2005; Rubin, 2008*), by incorporating dilatancy (*Liu and Rubin, 2010; Segall et al., 2010*), and by modifying the frictional parameterization to incorporate transitions from velocity-weakening (VW) to velocity-strengthening (VS) behavior at high slip speeds (*Shibazaki and Iio, 2003; Shibazaki and Shimamoto, 2007*). Discriminating between these modeling strategies is difficult with currently available external constraints. However, the ubiquitous presence of mixed brittle and ductile deformation features along faults exhumed from relevant depths suggests a basic mechanism for sustaining aseismic transients that is grounded in field interpretations of varying deformation styles (*Fagereng and Sibson, 2010; Fagereng, 2011; Fagereng et al., 2011; Bebout and Barton, 2002; Meneghini et al., 2009*).

Our model differs from previous studies by incorporating mixed frictional parameters along the fault surface that are manifest as alternating sections of VW and VS materials in the zone that hosts transient slip events. Linear analysis of a spring-slider system composed of two blocks in series, one with VW and one with VS properties, provides an approximate prediction for the sliding stability of the elastic model. Our results demonstrate how different combinations of geological materials produce the full range of sliding styles that are observed along plate-bounding faults.

2.2. Methods

The governing equations are solved on a one-dimensional fault segment, referred to simply as “the fault”, with an up-dip boundary corresponding to a seismogenic zone that is locked on the timescale of transient events, and made to slip at the plate convergence velocity v_{plate} at a down-dip boundary corresponding to depths well below (80 km) those of tremor activity and slow slip (e.g. *Rubin, 2008*). Directly down-dip of the locked boundary the fault contains a variable mixture of VW ($a/b < 1$) and VS ($a/b > 1$) material. To describe the mixture, we define a parameter η as the ratio of the combined length of VW material in the fault, to the total length of the mixed region. Strongly VS material extends between the mixed region and the down-dip, forced-slip boundary; this region corresponds to a long transition zone from frictional sliding to distributed deformation below.

Friction on the fault is described using the single state variable rate-and-state law

$$\mu(v, \theta) = \mu_0 + a \ln\left(\frac{v}{v_0}\right) + b \ln\left(\frac{v_0 \theta}{d_c}\right), \quad (2.1)$$

where μ_0 is the friction coefficient at reference speed v_0 , θ is a state variable, a and b characterize whether μ evolves to a higher or lower value with sliding rate v , and d_c

is the characteristic distance over which this evolution takes place according to

$$\dot{\theta} = -\frac{v\theta}{d_c} \ln\left(\frac{v\theta}{d_c}\right). \quad (2.2)$$

Stress balance requires that

$$\frac{G}{2\pi(1-\nu)} \int_{-\infty}^{\infty} \frac{\partial\delta/\partial\xi}{\xi-x} d\xi = \sigma\mu(v,\theta) + \frac{G}{2v_s}v, \quad (2.3)$$

where $\partial\delta/\partial\xi$ represents displacement gradients along the fault, with local coordinate x . The term on the left is derived from plane strain solutions for stress due to displacements on a fault embedded in an elastic medium with shear modulus G and Poisson ratio ν . The first term on the right is the stress due to friction, which is proportional to the effective normal stress σ . The remaining term describes stresses due to inertia, which scale with the ratio of the slip rate to the shear-wave speed v_s (*Rice, 1993*). Equations (1), (2), and (3) are cast as coupled first order differential equations in v and θ and integrated using ODE solver routines in MATLAB.

We characterize three modes of fault slip (*Rubin, 2008*): 1) dynamic sliding, with maximum slip speeds limited by inertia; 2) slow sliding, characterized by repeating transient slip events with slip speeds limited by friction; and 3) stable sliding, with slip speeds approaching a steady-state. Slip speeds and dip-parallel (assuming perfectly dip-slip motion) fault lengths W are normalized, respectively, by the plate convergence rate v_{plate} , and the critical nucleation length

$$h^* = \frac{Gd_c}{\sigma(b_{\text{vw}} - a_{\text{vw}})} \quad (2.4)$$

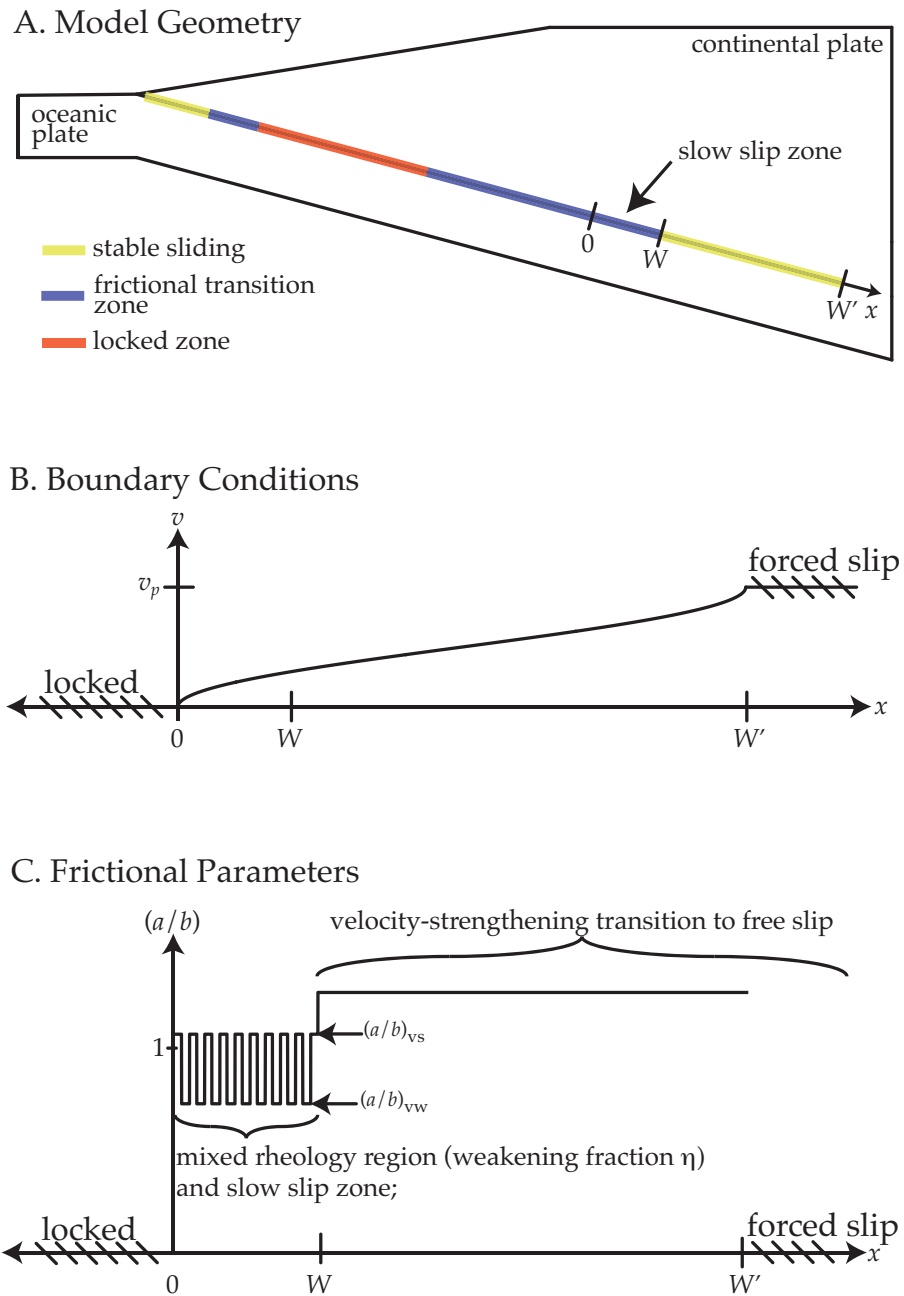


FIGURE 2.1. (a) Model geometry for a simplified two-dimensional subduction zone, the free surface is not included in the model. (b) Boundary conditions along the subduction plate-boundary fault. (c) Frictional parameters along the fault.

TABLE 2.1. Nominal parameter values used in model simulations. Ranges are given for those parameters that are varied to explore the different regimes of model behavior.

Symbol	Definition	Value
a_{vs}	friction parameter	0.0105
a_{vw}	friction parameter	0.001–0.095
b_{vs}	friction parameter	0.01
b_{vw}	friction parameter	0.01
d_c	characteristic slip distance	40 μm
v_{plate}	plate convergence velocity	$\sim 3 \text{ cm yr}^{-1}$
v_s	shear wave velocity	3 km s^{-1}
ν	Poisson’s ratio	0.25
G	shear modulus	30 GPa
W	fault length	20 km
W/h^*	scaled fault length	6–48
η	fraction VW on fault	0.35–0.9
h^*	nucleation distance	0.4–3.3 km
σ	effective stress	0.04–5.8 MPa

that must slip to nucleate dynamic events along a homogeneous fault (parameter definitions and nominal values in Table 2.1). By choosing the ratio of fault length W to h^* , the effective normal stress σ on the fault is set by equation (4) and does not exceed 6 MPa for any reported simulations. Parameters are chosen to maintain consistency with previous models (e.g. *Rubin, 2008; Liu and Rubin, 2010; Segall et al., 2010*) and to reflect the hypothesis that slow slip and tremor are made possible by a combination of temperature dependent frictional behavior and low effective stress.

A schematic diagram of the model domain is given in Figure 2.1. The length of the locked and forced-slip section is set to $8W$ (see Figure 2.1b). The fault has mixed frictional properties within the interval $0 < x < W$ and is strictly velocity-strengthening along $W < x < W'$. For all simulations, we set $W = 20 \text{ km}$ and $W'/W = 4$; the value of this ratio has a slight affect on the location of sliding behavior transitions (i.e. steady to slow sliding, or slow to dynamic sliding), as well as the maximum velocity during slow events (*Rubin, 2008; Liu and Rubin, 2010*). We

use a grid spacing $dx = L_b/20$ for all simulations reported here, where

$$L_b = \frac{Gd_c}{\sigma b} = h^* \left[1 - \left(\frac{a}{b} \right)_{\text{vw}} \right] \quad (2.5)$$

is the nucleation length scale introduced by *Dieterich* (1992).

We control the volume fraction η of VW material by changing the length of VW patches. The length of individual VS patches is set to five grid points, or $5dx = L_b/4$. This length was chosen primarily for numerical stability. For any given simulation, the value of the grid spacing dx depends on the value of $(a/b)_{\text{vw}}$, so η is controlled essentially by changing the number of VS patches. Our discretization introduces more numerical error as $(a/b)_{\text{vw}}$ decreases because of the increase in grid spacing that results. The effect can be seen in Figure 2.2, where the transition to dynamic sliding becomes less well defined for $\eta = 0.35$ than for other values of η . If the grid spacing were decreased this effect would not be seen.

Rubin and Ampuero (2005) showed that rupture nucleation on faults obeying rate-and-state friction is controlled by the behavior when conditions are well above steady state (i.e. $v\theta/d_c \gg 1$); in this limit, experimental observations (*Nakatani*, 2001) are well described by the slip law, equation (2). Accordingly, we employ the slip law form of state evolution to calculate frictional stresses along the fault. For the grid spacing defined above, use of the slip law introduces small but detectable errors near the transition to dynamic sliding. The slip-weakening zone at the nucleation front sets the lower limit on numerical resolution. *Ampuero and Rubin* (2008) showed that the size of the slip-weakening zone is well approximated by $0.75 \ln(v_{\text{max}}\theta_i/d_c)L_b$ where v_{max} is the maximum slip velocity in the slip-weakening zone and θ_i is the state value ahead of the nucleation front. During slow events this quantity remains large enough that a grid spacing of $dx = L_b/20$ is adequate to resolve the nucleation front;

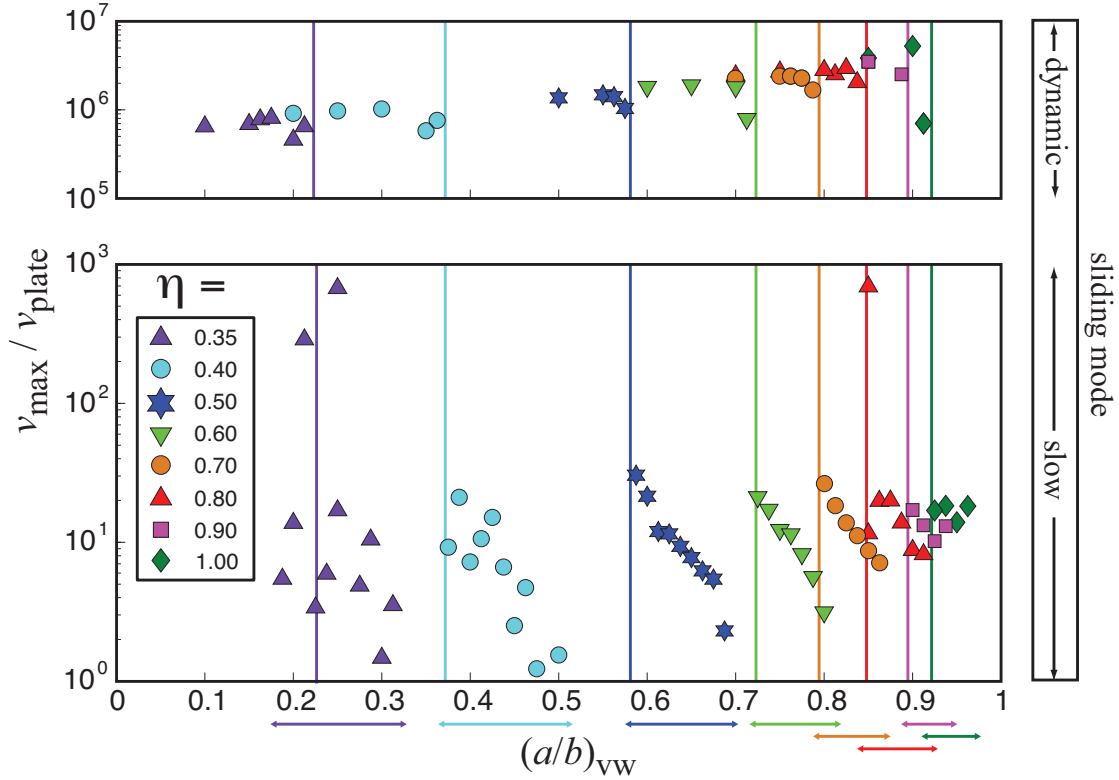


FIGURE 2.2. Normalized maximum sliding velocities from simulations with $W/h^* = 6$ and $(a/b)_{vs} = 1.05$. Each point on the graph represents an individual simulation; with different symbols referring to the values of η indicated in the legend. Vertical bars show the onset of dynamic sliding for each η . Horizontal bars along the x -axis delineate values of $(a/b)_{vw}$ that produce periodic slow events, which are shown in the lower panel. Higher values of $(a/b)_{vw}$, relative to horizontal bars for a given value of η , produce steady sliding and are not shown. In order to illustrate the model behavior, maximum slip velocities are included in the upper panel from simulations that produced dynamic sliding events; however, we note that the absolute magnitude (but not the dynamic behavior) of dynamic slip velocities is only approximated by our modeling procedure.

it is only when sliding becomes dynamic that the slip-weakening zone of the nucleation front becomes small enough that our grid spacing causes detectable numerical errors. Since our focus here is on slow events, we consider the presence of such errors to be acceptable; however, to further test our intuition we conducted a limited number of simulations with $dx = L_b/200$ and confirmed that they did not show marked

changes in maximum slip velocities or the location of the stable-unstable transition from equivalent simulations with $dx = L_b/20$.

Movies 1 and 2 illustrate typical simulations for each of the sliding behaviors (stable, slow, and dynamic) defined in the main text. Each movie shows the time evolution of sliding velocity, normalized by the plate convergence velocity v_{plate} , within the region of the fault containing mixed frictional parameters (i.e. $0 < x < W$, see Figure 2.1). For the three simulations shown, $W/h^* = 6$ and $\eta = 0.7$ (orange circles in Figures 2.2, 2.7, and 2.3), other parameter values are shown in the movie frames. In general, sliding events nucleate near the down-dip boundary of the mixed region, and propagate up-dip. Movie 1 shows a stable simulation; slow sliding events occur at the start due to the initial conditions. However, the maximum sliding velocity decreases with each subsequent event until the fault reaches a steady-state. A simulation producing slow sliding events is shown in Movie 2. Here, events nucleate down-dip and propagate up-dip periodically, maintaining an essentially constant maximum sliding velocity for each event. In these slow events, there is some down-dip propagation as the fault relaxes after the initial up-dip propagating event reaches the up-dip, locked boundary. In Movie 2 the alternating sections of VW and VS material manifest themselves as the saw-tooth pattern seen in the velocity profile during sliding events.

2.3. Results and Discussion

We ran simulations at constant fault length $W/h^* = 6$, for $0.35 < \eta < 1$, keeping frictional parameters that characterize VS material constant and varying the rate sensitivity of VW material by changing the ratio $(a/b)_{\text{vw}} < 1$ (Figure 2.2) (note: $a/b = 1$ is velocity neutral; ratios further from unity are more rate sensitive). As $(a/b)_{\text{vw}}$ decreases, fault behavior evolves smoothly from stable (not shown) to slow sliding,

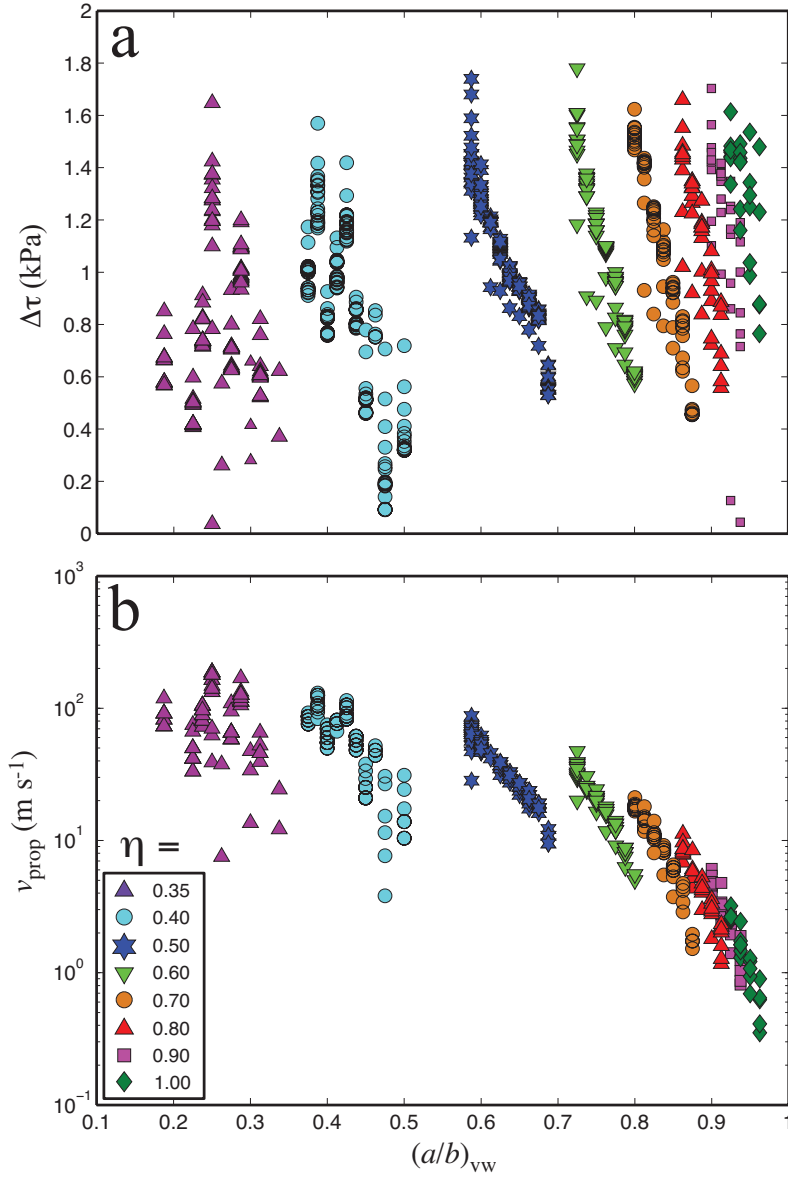


FIGURE 2.3. (a) Static stress drop $\Delta\tau$ and (b) propagation velocity v_{prop} for slow events from simulations with scaled fault length $W/h^* = 6$ and velocity-strengthening component characterized by $(a/b)_{vs} = 1.05$, with the values of η noted in the legend. Each point represents an individual event from the simulations presented in Figure 2.2 of the main text. Note that multiple events occurred during each simulation (i.e. points with identical $(a/b)_{vw}$).

and switches abruptly from slow to dynamic sliding. With less VW material (lower η), the value of $(a/b)_{vw}$ that marks the transition to dynamic sliding decreases. Whereas

previous models (*Liu and Rice, 2005; Rubin, 2008; Liu and Rubin, 2010; Segall et al., 2010*) have generated similar behavior using faults entirely composed of VW material, our results demonstrate that areas of the plate interface that host tremor and slow slip can also contain sizeable fractions of VS material. The VS material that is required to stabilize slow slip in our model is consistent with expected changes in frictional properties at higher ambient temperatures beneath the seismogenic zone, and field evidence in exhumed fault rocks for ductile deformation (*Fagereng and Sibson, 2010; Fagereng, 2011; Fagereng et al., 2011; Bebout and Barton, 2002; Meneghini et al., 2009*), which may continue to take place in the time between transient events that this treatment is designed to capture.

In Cascadia, tremor epicenters correlate with locations of high slip-rate during ETS events (*Wech and Creager, 2008; Bartlow et al., 2011*). Such findings support the hypothesis that tremor occurs as locally accelerated slip on heterogeneities within the slipping region. Accordingly, we interpret tremor propagation velocities as corresponding with modeled dip-parallel slip propagation velocities v_{prop} . Tremor events in Cascadia propagate along dip at 30–200 km/hr (*Ghosh et al., 2010*), similar to rates (25–150 km/hr) observed in southwest Japan (*Shelly et al., 2007a*). These values compare well with v_{prop} for our simulations. Figure 2.3 shows the static stress drops $\Delta\tau$ and propagation velocities v_{prop} for the slow events from the simulations shown in Figure 2.2. Propagation velocities range from $\sim 3.6 - 360 \text{ km hr}^{-1}$ and decrease as the amount η of velocity weakening material increases. This is due to the fact that lower values of $(a/b)_{\text{vw}}$ are required to stabilize slow sliding events for lower values of η .

Tectonic tremor has been found to consist of numerous low (LFE) and very low (VLFE) frequency earthquakes (*Shelly et al., 2006; Wech and Creager, 2007*).

Estimating the source parameters of tremor events remains a significant challenge. However, sparse estimates of static stress drop $\Delta\tau_s$ can be compared to our model results. In southwest Japan, $\Delta\tau_s$ for tremor events has been estimated at < 10 kPa to ~ 100 kPa (Obara, 2010). Also in southwest Japan, more precise determinations of $\Delta\tau_s$ in the range 0.1–10 kPa have been made for VLFs in the accretionary wedge (Ito and Obara, 2006a). Similar static stress drops have been inferred for large slow-slip events (Gao *et al.*, 2012). Our simulations predict static stress drops that are insensitive to η , but increase from ~ 0.1 –1.8 kPa with decreasing $(a/b)_{vw}$ (Figure 2.3b).

The presence of VS material in the fault produces slow sliding behavior over a larger range of fault lengths than is expected for strictly VW faults. We ran simulations with $(a/b)_{vw} = 0.8$ for a range of W/h^* (Figure 2.4). For each scaled fault length, as η increases the behavior evolves smoothly from stable to slow sliding, and abruptly from slow slip to dynamic sliding. The results illustrate the persistence of slow sliding events on faults that are much longer than the critical nucleation length (e.g. $W/h^* = 48$). For these calculations, VS material is characterized by frictional parameters that are almost velocity-neutral. Larger values of $(a/b)_{vs}$ would lead to slow sliding behavior for $W/h^* > 48$, corresponding to longer faults, or to smaller values of h^* associated with higher effective normal stresses.

2.4. Double Spring-Slider System

Validation and insight into the model behavior is gained by considering a simplified spring-slider system consisting of two rigid blocks held in frictional contact with a rigid surface at a constant normal stress σ and connected to each other by a spring with stiffness k_2 (Figure 2.5). The first block has $(a/b)_{vw} < 1$ and base

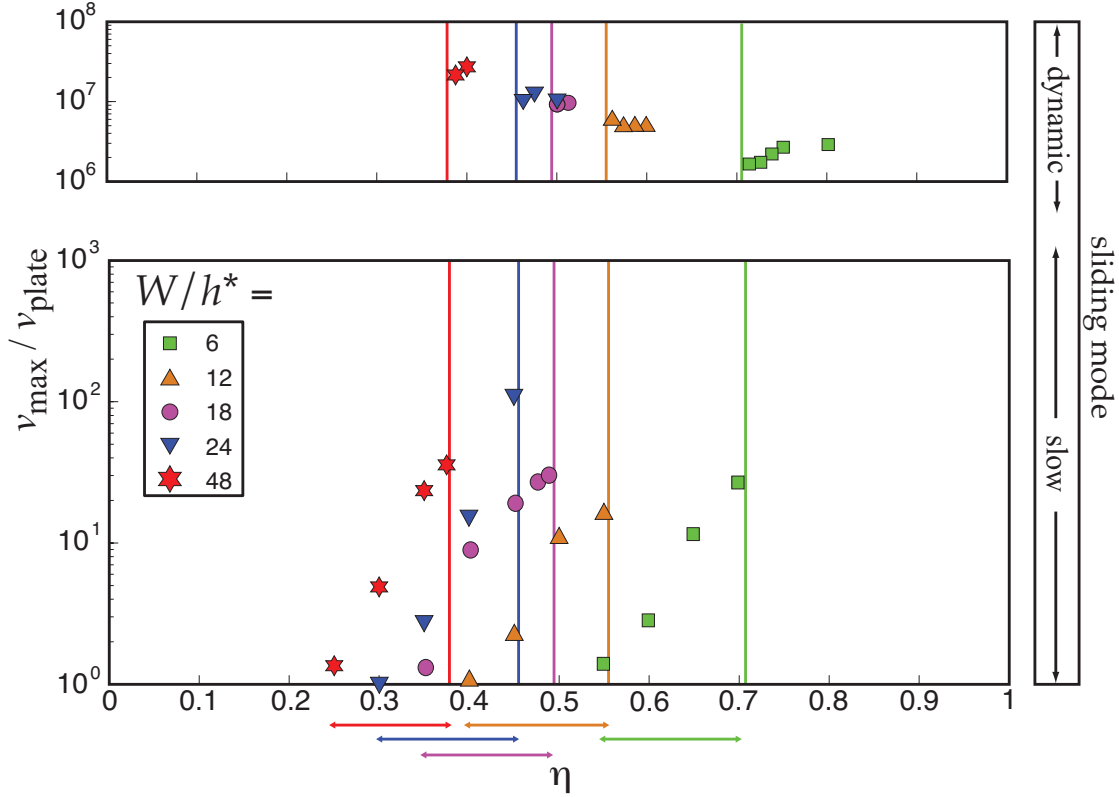


FIGURE 2.4. Normalized maximum sliding velocities from simulations with $(a/b)_{vw} = 0.8$ and $(a/b)_{vs} = 1.05$. Each point represents a different simulation, using values of η chosen to search for the sliding behavior transitions, with the onset of dynamic events marked by the vertical colored lines. The corresponding colored symbols mark simulations run with the different values of W/h^* that are noted in the legend. Bars along the x -axis delineate ranges of η that produce periodic slow events.

area η , while the second has $(a/b)_{vs} > 1$ with base area $1 - \eta$. A spring with stiffness k_1 connects the VW block to a load point that moves at constant velocity. Elastic compliance is accommodated by the stiffness of the springs, while inelastic deformation is accommodated by the slip displacement of the blocks. Linear stability analysis shows that two overlapping conditions determine the sliding stability (Figure 2.6). Each condition yields a critical value of k_1 that depends on k_2 . In the limit $k_2 \rightarrow \infty$, with the characteristic distance for state evolution d_c assumed constant,

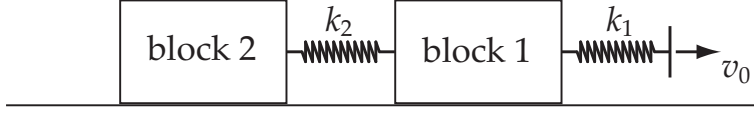


FIGURE 2.5. Schematic illustration of a double, spring-block slider system, with spring constants k_1 and k_2 and load-point velocity v_0 .

one stability condition vanishes and the remaining one takes the compact form

$$k_{1crit}^{\infty} = \frac{\sigma [\eta(b_{vw} - a_{vw}) + (1 - \eta)(b_{vs} - a_{vs})]}{d_c}. \quad (2.6)$$

Recognizing that $k_{1crit}^{\infty} = G/h_{mixed}^*$, the critical length scale for rupture nucleation is

$$h_{mixed}^* = \frac{Gd_c}{\sigma [\eta(b_{vw} - a_{vw}) + (1 - \eta)(b_{vs} - a_{vs})]}. \quad (2.7)$$

which recovers equation (4) when $\eta \rightarrow 1$. Comparison with h^* from equation (2.4) reveals how VS material effectively increases the critical slip length for instability of a spring-slider system (since $b_{vs} - a_{vs} < 0$). This underlies the predictions of our elastic model, which demonstrate that longer fault segments are required to slip simultaneously in order to nucleate transient slip events, relative to strictly VW faults. That is, by effectively increasing the critical nucleation length, geologic heterogeneity allows for slow slip to occur over larger sections of fault before slip becomes dynamic.

Figure 2.7 compares the double slider results against the numerically determined field in which slow slip is observed for the model calculations summarized in Figure 2.2. Within the context of the double slider system, the value of k_2 represents the degree of elastic coupling between the VW and VS materials. When $k_2 \rightarrow \infty$, the spring connecting the blocks is rigid, so VW and VS materials act as one block and slide at equal velocity. Hence, the stability condition predicted by equation (2.7) is more

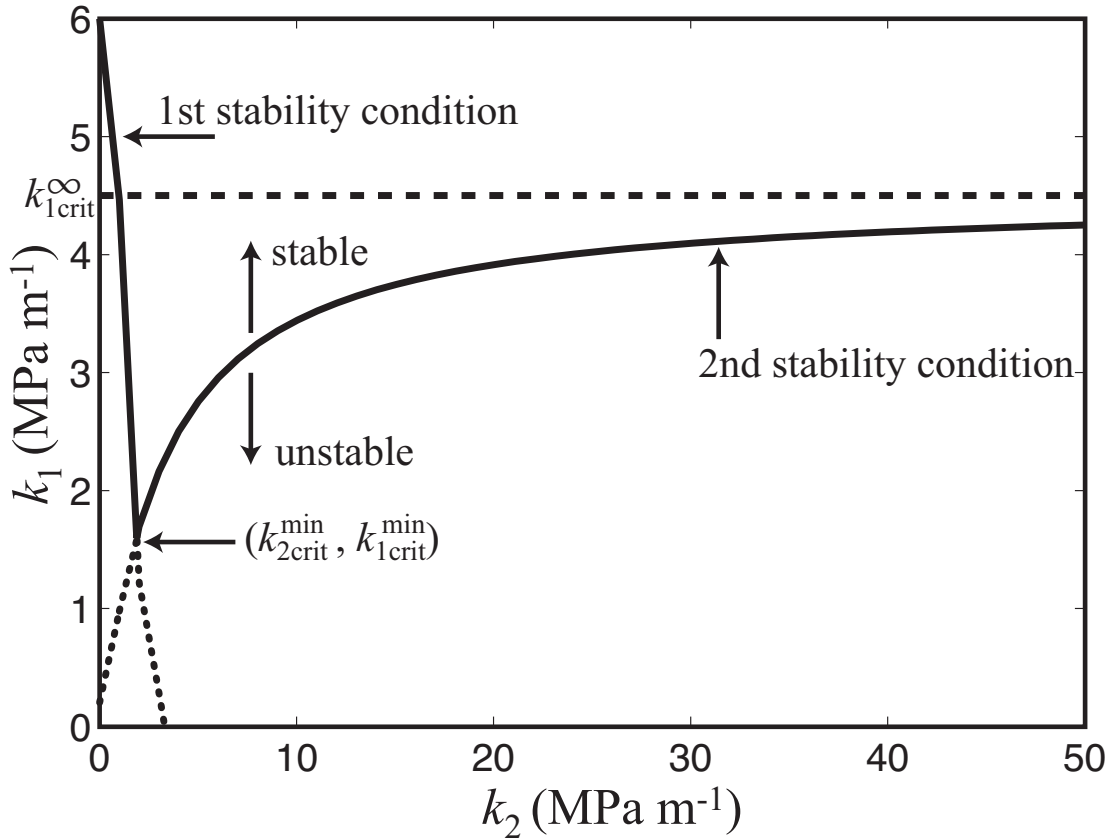


FIGURE 2.6. Stability field for double spring-slider system. The solid line indicates the stable-unstable boundary; the dashed line indicates this boundary for $k_2 \rightarrow \infty$ from equation (5). The motion of the blocks is stable when k_1 is greater than the critical value shown by the solid black line. The discontinuity where the two stability conditions overlap marks the minimum stability condition that is plotted with the solid curve on Figure 2.7; the dotted lines show the extension of each stability condition to stiffnesses that are beneath the critical stability predicted by the other condition. $\sigma = 240$ kPa, $(a/b)_{vw} = 0.83$, $(a/b)_{vs} = 1.05$, $d_c = 40$ μm , and $\eta = 0.6$.

restrictive than the behavior expected from the elastic model, which can accommodate significant velocity gradients along the fault. When k_2 is finite, the separation of the two blocks varies and the connecting spring stores elastic strain energy so that they slide at different rates – a situation akin to the elastic model. In natural shear zones, the degree of coupling between VW and VS elements scales with the degree of interconnectivity between brittle VW phacoids within a *mélange* matrix, represented

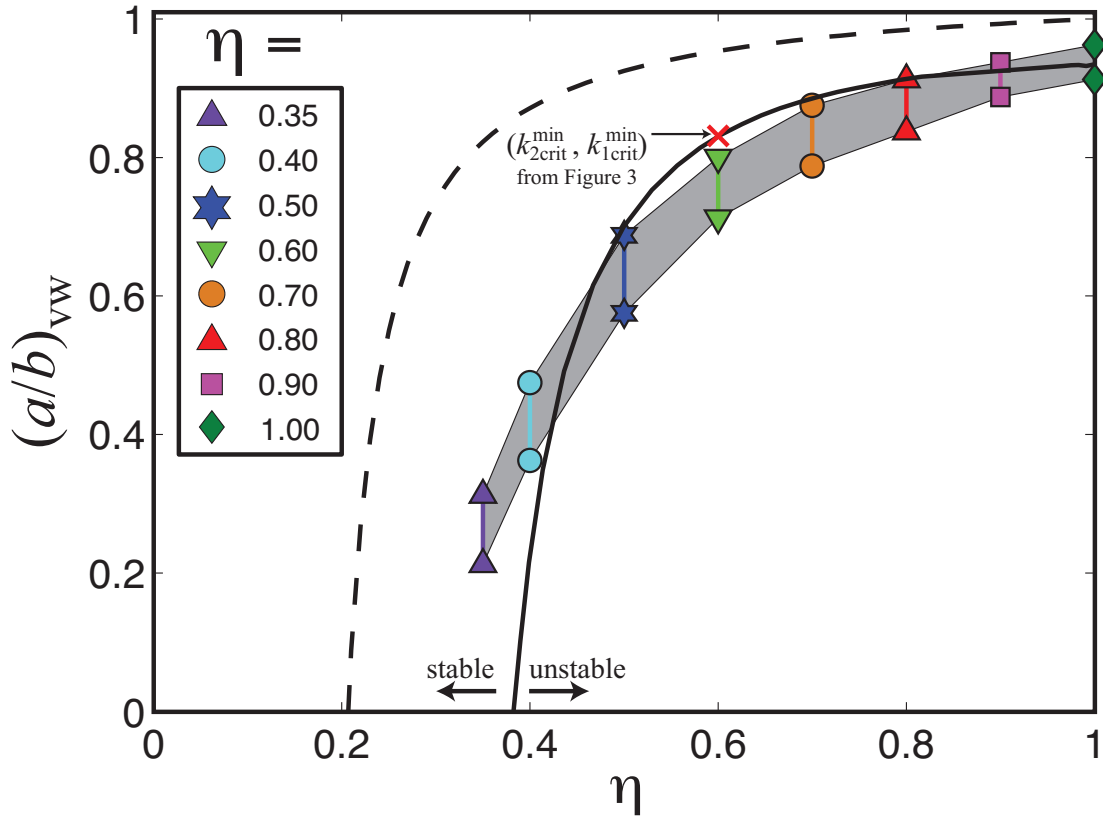


FIGURE 2.7. Stability field for elastic model. For the elastic model, slow sliding events occur within the gray shaded region, unstable (stable) sliding occurs below (above) this region. The dashed black line marks the stability boundary predicted by equation (6) (i.e. k_{1crit}^∞) and corresponds to the dashed line in Figure 2.6. The solid black line marks the theoretical stability boundary calculated by methods discussed in the text and the auxiliary information. The red cross marks the location of the point $(k_{2crit}^{\min}, k_{1crit}^{\min})$ from Figure 2.6.

in our model by the VS component. With this interpretation, $k_2 \rightarrow \infty$ corresponds to larger and/or more phacoids (either would increase the degree of interconnectivity), and decreasing values of k_2 correspond with decreasing size and/or fewer phacoids. As k_2 decreases, the critical stiffness of k_1 decreases, reducing the size of the unstable domain. The elastic model stability corresponds approximately with the minimum critical stiffness. For example, the location of the minimum stiffness point $(k_{2crit}^{\min}, k_{1crit}^{\min})$ from Figure 2.6 is shown on Figure 2.7.

The stability boundary is found by tracking the point $(k_{2\text{crit}}^{\text{min}}, k_{1\text{crit}}^{\text{min}})$ (i.e. the intersection, in k_2 - k_1 space, of the stability boundaries defined by (2.27) and (2.28), see Figure 2.6) through η - $(a/b)_{\text{vw}}$ space. What is desired are the coordinates $(\eta, (a/b)_{\text{vw}})$ of this point for given values of k_1 and k_2 ; the set of these points will describe the minimum stability boundary. The stiffness k_1 is set by the fault length and shear modulus, so k_2 is allowed varied and decreases from 2.6 to 0.02 MPa along the path of the solid black line in Figure 2.7. Thus the procedure consists of calculating the stability boundaries and finding their intersection in η - $(a/b)_{\text{vw}}$ space by numerically evaluating (2.27) and (2.28) for different values of k_2 , with k_1 , $(a/b)_{\text{vs}}$, and other parameters constant.

2.5. Conclusions

Recent field (*Fagereng and Sibson, 2010; Collettini, 2011; Fagereng, 2011; Fagereng et al., 2011*) and modeling studies (*Ando et al., 2010; Daub et al., 2011; Nakata et al., 2011*) suggest that fault heterogeneity (e.g. a mixture of VW and VS materials, or similarly, a mixture of brittle and ductile materials) along plate interfaces may be required for the generation of slow sliding transients and tectonic tremor. Matching observed recurrence intervals for tremor along the San Andreas fault at Parkfield, CA with a model based on a single block-spring-slider system, suggests that 40–70% of the frictional contacts at depth must be brittle, the remainder deforming in a ductile manner (*Daub et al., 2011*). Additionally, models (*Ando et al., 2010; Nakata et al., 2011*) that include fault heterogeneity as unstable patches on a stable background fault can reproduce migration speeds (dip- and strike-parallel) and source spectra of LFE/tremor events; including viscous effects (*Nakata et al., 2011*) produces a transition in rupture behavior from dynamic to slow sliding, similar to the

model presented here. Field studies present compelling evidence for these types of fault heterogeneity, notably at the Chrystalls Beach Complex, New Zealand (*Fagereng and Sibson, 2010; Fagereng, 2011; Fagereng et al., 2011*), where correlations are found between the volume fraction of competent material and inferred mechanisms of deformation (e.g. continuous, discontinuous). Competent volume fractions of ~ 0.3 – 0.85 produce structural markers of mixed continuous-discontinuous sliding behavior that may record LFEs.

Our results demonstrate that aseismic transients arise naturally along geologically heterogeneous faults, without requiring finely tuned rheological properties. All of our calculations are made assuming $\sigma < 6$ MPa, implying that fluid pressures on the fault approach lithostatic values (*Shelly et al., 2006; Audet et al., 2009; Matsubara et al., 2009*). We emphasize that further efforts to characterize fault rock properties are necessary to better constrain future modeling efforts. The presence of velocity-strengthening material mixed with velocity-weakening material increases the fault length capable of simultaneous, aseismic sliding. Our numerical results are well described by a double spring-block-slider system, suggesting that further study of such simple models may shed additional light on the physical mechanisms behind aseismic transients on plate boundary faults.

2.6. Linear Stability of a Two Block Spring-Slider System

For the system depicted in Figure 2.5, the equations of motion are

$$\eta\tau_1 = k_1(v_0t - \delta_1) - k_2(\delta_1 - \delta_2), \quad (2.8)$$

$$\text{and } (1 - \eta)\tau_2 = k_2(\delta_1 - \delta_2), \quad (2.9)$$

where δ_i ($i = 1, 2$) are the displacements of each block relative to the reference position at time $t = 0$. The shear stress τ_i along the base of each block is proportional to the normal stress σ and depends on the frictional constitutive behavior, which is a function of the sliding velocity v_i , and the state of the sliding surface θ_i , so that

$$\tau_i = \sigma F(\theta_i, v_i) . \quad (2.10)$$

Additionally, for each block the rate of change of the state variable is assumed to depend only on its sliding velocity and the instantaneous state of the sliding surface, so that

$$\dot{\theta}_i = G(\theta_i, v_i) . \quad (2.11)$$

To simplify the notation, we drop the arguments of $F(\theta_i, v_i)$ and $G(\theta_i, v_i)$ and write them more compactly as F_i and G_i . At steady-state, both blocks move at the load-point velocity $v_i = v_0$, and we write that $\tau_i = \tau_i^{ss}$ and $\theta_i = \theta_i^{ss}$. Since we are interested in infinitesimal perturbations from steady-state, we linearize by requiring $q_i \approx q_i^{ss} + q_i^*$ so that the perturbations satisfy

$$\tau_i^* \approx \sigma(F_{iv}v_i^* + F_{i\theta}\theta_i^*) , \quad (2.12)$$

$$\text{and } \dot{\theta}_i^* \approx G_{iv}v_i^* + G_{i\theta}\theta_i^* , \quad (2.13)$$

where subscripted v and θ indicate derivatives with respect to that variable (i.e. $F_{iv} = \frac{\partial F_i}{\partial v}$).

We now proceed to rewrite the system of linear equations solely in terms of the velocities v_i . First we eliminate the terms in θ_i^* by taking the time derivative of (2.12)

and substituting for θ_i^* and $\dot{\theta}_i^*$ into the result to obtain

$$\dot{\tau}_i^* = \sigma F_{iv} \dot{v}_i^* + \sigma (F_{i\theta} G_{iv} - F_{iv} G_{i\theta}) v_i^* + G_{i\theta} \tau_i^* . \quad (2.14)$$

Next we differentiate (2.14) with respect to time and use (2.8) and (2.9) and their time derivatives to eliminate the terms in τ_i^* , and write

$$\begin{aligned} 0 &= \sigma F_{1v} \ddot{v}_1^* + \left(\sigma F_{1\theta} G_{1v} - F_{1v} G_{1\theta} + \frac{k_1 + k_2}{\eta} \right) \dot{v}_1^* - \frac{k_2}{\eta} \dot{v}_2^* \\ &\quad + \frac{G_{1\theta}}{\eta} [-(k_1 + k_2)v_1^* + k_2 v_2^*] , \text{ and} \\ 0 &= \sigma F_{2v} \ddot{v}_2^* + (\sigma F_{2\theta} G_{2v} - \sigma F_{2v} G_{2\theta} + k_2) \dot{v}_2^* - k_2 \dot{v}_1^* + G_{2\theta} k_2 (v_1^* - v_2^*) . \end{aligned} \quad (2.15)$$

Equations (2.15) are a coupled system of ordinary differential equations in v_1^* and v_2^* that can be rewritten using matrix notation as

$$\mathbf{M}\ddot{\mathbf{v}} + \mathbf{C}\dot{\mathbf{v}} + \mathbf{K}\mathbf{v} = 0 . \quad (2.16)$$

We look for solutions to (2.16) in the form $\mathbf{v} = \mathbf{v}_0 e^{\lambda t}$, so that

$$\mathbf{Q}(\lambda)\mathbf{v} = 0 , \quad (2.17)$$

where $\mathbf{Q}(\lambda) = \mathbf{M}(\lambda^2) + \mathbf{C}(\lambda) + \mathbf{K}$. Equation (2.17) represents an eigenvalue problem with eigenvalues λ and corresponding eigenvectors \mathbf{v} . The stability of the linearized system depends on the signs of the real parts of the eigenvalues. When they are all negative, small perturbations to steady-state sliding decay in time, but if any one of the eigenvalues has a positive real component, then small perturbations are expected to grow exponentially. To find the eigenvalues we set $\det(\mathbf{Q}) = 0$, and solve for λ .

The determinant of Q is a fourth-order polynomial in λ that can be written in the form

$$\det(Q) = s_4\lambda^4 + s_3\lambda^3 + s_2\lambda^2 + s_1\lambda + s_0 , \quad (2.18)$$

with coefficients

$$\begin{aligned} s_4 &= \sigma^2 F_{1v} F_{2v} , \\ s_3 &= \frac{\sigma(k_1 + k_2)}{\eta} F_{2v} T_1 + \frac{\sigma k_2 F_{1v} T_2}{1 - \eta} , \\ s_2 &= \frac{k_2(k_1 + k_2)}{\eta(1 - \eta)} T_1 T_2 - \frac{\sigma k_2 F_{1v} G_{2\theta}}{1 - \eta} - \frac{\sigma(k_1 + k_2)}{\eta} F_{2v} G_{1\theta} - \frac{k_2^2}{\eta(1 - \eta)} , \\ s_1 &= \frac{k_2^2}{\eta(1 - \eta)} (G_{1\theta} + G_{2\theta}) - \frac{k_2(k_1 + k_2)}{\eta(1 - \eta)} (T_2 G_{1\theta} + T_1 G_{2\theta}) , \text{ and} \\ s_0 &= \frac{k_1 k_2}{\eta(1 - \eta)} G_{1\theta} G_{2\theta} , \text{ where} \\ T_1 &= 1 - \frac{\eta\sigma}{k_1 + k_2} (F_{1v} G_{1\theta} - F_{1\theta} G_{1v}) , \text{ and} \\ T_2 &= 1 - \frac{\sigma(1 - \eta)}{k_2} (F_{2v} G_{2\theta} - F_{2\theta} G_{2v}) . \end{aligned}$$

Formulas exist for the exact solution of a quartic equation, but the general case yields roots that contain hundreds of terms. Therefore, we look for approximate solutions to (2.17) and begin by examining the neutral stability case. If we assume that equation (2.17) has at least one pair of complex conjugate eigenvalues $\lambda = c \pm di$, then its characteristic polynomial can be written as

$$\lambda^4 + \frac{s_3}{s_4}\lambda^3 + \frac{s_2}{s_4}\lambda^2 + \frac{s_1}{s_4}\lambda + \frac{s_0}{s_4} = (\lambda - \lambda_1)(\lambda - \lambda_2)[\lambda - (c + di)][\lambda - (c - di)] . \quad (2.19)$$

At neutral stability $c = 0$ and we can solve for λ_1 and λ_2 as

$$\lambda_1 = \frac{1}{2} \left\{ -\frac{s_3}{s_4} + \left[\left(\frac{s_3}{s_4} \right)^2 - 4 \frac{s_2 s_3 - s_1 s_4}{s_3 s_4} \right]^{1/2} \right\}, \quad (2.20)$$

$$\text{and } \lambda_2 = \frac{1}{2} \left\{ -\frac{s_3}{s_4} \pm \left[\left(\frac{s_3}{s_4} \right)^2 - 4 \frac{s_0 s_3}{s_1 s_4} \right]^{1/2} \right\}. \quad (2.21)$$

Solving the equations of motion (2.8) and (2.9) numerically shows that the system has two pairs of complex conjugate eigenvalues and that (2.20) above is a good approximation of one of those pairs, while (2.21) is not a good approximation for either pair. We now repeat the above procedure assuming that there are two complex conjugate eigenvalue pairs $\lambda = m \pm ni$ and $\lambda = c \pm di$, in which case (2.19) is rewritten as

$$\lambda^4 + \frac{s_3}{s_4} \lambda^3 + \frac{s_2}{s_4} \lambda^2 + \frac{s_1}{s_4} \lambda + \frac{s_0}{s_4} = [\lambda - (m + ni)][\lambda - (m - ni)][\lambda - (c + di)][\lambda - (c - di)]. \quad (2.22)$$

At neutral stability (i.e. $c = m = 0$) we find

$$n = \pm \sqrt{\frac{1}{2s_4} [s_2 + (s_2^2 - 4s_0 s_4)^{1/2}]^{1/2}}, \quad (2.23)$$

$$\text{and } d = \pm \sqrt{\frac{1}{2s_4} [s_2 - (s_2^2 - 4s_0 s_4)^{1/2}]^{1/2}}. \quad (2.24)$$

Comparisons with numerical solutions of the equations of motion show that (2.23) is not a good approximation for the imaginary part of either eigenvalue pair, but that (2.24) adequately reproduces the imaginary part of the eigenvalue pair that is not associated with (2.20). We now have expressions for one eigenvalue pair (2.20) and

the imaginary part of the second pair (2.24), so

$$\lambda^4 + \frac{s_3}{s_4}\lambda^3 + \frac{s_2}{s_4}\lambda^2 + \frac{s_1}{s_4}\lambda + \frac{s_0}{s_4} = (\lambda - \lambda_1)(\lambda - \lambda_2)[\lambda - (c + di)][\lambda - (c - di)] \quad (2.25)$$

where now $\lambda_2 = \bar{\lambda}_1$ from (2.20), and the over-bar indicates the complex conjugate.

Solving for c leads to

$$c = \frac{-2\lambda_1\lambda_2 \pm \{(2\lambda_1\lambda_2)^2 - 4(\lambda_1 + \lambda_2)[d^2(\lambda_1 + \lambda_2) + s_1/s_4]\}^{1/2}}{2(\lambda_1 + \lambda_2)}. \quad (2.26)$$

Numerical comparisons show that choosing the positive sign in the numerator gives a good approximation to the real part of the eigenvalue pair whose imaginary part is given by (2.24).

2.6.1. Stability Conditions

We can now examine the eigenvalues for stability conditions. To summarize, the final approximate solutions are

$$\lambda_1 = \frac{1}{2} \left\{ -\frac{s_3}{s_4} + \left[\left(\frac{s_3}{s_4} \right)^2 - 4 \frac{s_2 s_3 - s_1 s_4}{s_3 s_4} \right]^{1/2} \right\},$$

$$\lambda_2 = \frac{1}{2} \left\{ -\frac{s_3}{s_4} - \left[\left(\frac{s_3}{s_4} \right)^2 - 4 \frac{s_2 s_3 - s_1 s_4}{s_3 s_4} \right]^{1/2} \right\},$$

and $\lambda_3 = \bar{\lambda}_4 = c + di$, where

$$c = \frac{-2\lambda_1\lambda_2 + \{(2\lambda_1\lambda_2)^2 - 4(\lambda_1 + \lambda_2)[d^2(\lambda_1 + \lambda_2) + s_1/s_4]\}^{1/2}}{2(\lambda_1 + \lambda_2)},$$

$$\text{and } d = \sqrt{\frac{1}{2s_4} [s_2 - (s_2^2 - 4s_0s_4)^{1/2}]^{1/2}} .$$

From the definitions above it can be seen that both λ_1 and λ_2 will be positive when

$$s_2s_3 - s_1s_4 < 0 . \quad (2.27)$$

Setting $\lambda_1, \lambda_2 < 0$, the real part c of the second pair of eigenvalues will be positive when $d^2(\lambda_1 + \lambda_2) + s_1/s_4 < 0$. If we assume from (2.20) that the real part of λ_1 and λ_2 is $-s_3/2s_4$, then the condition $c > 0$ becomes

$$\frac{s_1}{s_3} - \frac{s_2 - (s_2^2 - 4s_0s_4)^{1/2}}{2s_4} < 0 . \quad (2.28)$$

Evaluating (2.27) and (2.28) using the definitions of the coefficients s_i leads to quite complicated expressions; however, numerical evaluation of the two conditions is straightforward after making use of the definitions (*Ruina*, 1983)

$$\begin{aligned} F_{iv} &= \frac{a_i}{v_0} , \quad F_{i\theta} = \frac{b_i}{\theta^{ss}} , \\ G_{iv} &= -\frac{\theta^{ss}}{d_i} , \quad G_{i\theta} = -\frac{v_0}{d_i} , \\ T_1 &= 1 - \frac{\sigma\eta}{k_1 + k_2} \frac{d\tau^{ss}}{dv_1} , \\ \text{and } T_2 &= 1 - \frac{\sigma(1 - \eta)}{k_2} \frac{d\tau^{ss}}{dv_2} . \end{aligned}$$

Equation (5) is found by taking the limit $k_2 \rightarrow \infty$ and setting $d_1 = d_2 = d_c$, in which case (2.27) vanishes and (2.28) yields

$$k_1^\infty = \frac{\sigma [\eta(b_1 - a_1) + (1 - \eta)(b_2 - a_2)]}{d_c} . \quad (2.29)$$

2.7. Bridge

In this chapter I examined the frictional mechanics of subduction zone slow slip in the context of a subduction channel shear zone. In this model, slow slip is stabilized by a heterogeneous mixture of VW and VS materials within the plate interface. Such a mixture is motivated by a large body of work documenting the existence of a subduction channel at depths where slow slip occurs.

In Chapter III, I make further use of the subduction channel concept and examine mechanisms for the generation of large fluid pressures in the slow slip zone due to chemical dehydration reactions. Two separate reactions are considered, dehydration of 1) basalt within the subducting oceanic crust and 2) serpentinite within the subduction channel itself. The mechanics of a poro-elastic medium that includes these reactions, as well as a viscous component of deformation, are examined in detail.

CHAPTER III
GENERATION AND TRANSPORT OF EXCESS FLUID PRESSURE BY
DEHYDRATION REACTIONS IN THE SLOW SLIP REGION OF
SUBDUCTION ZONES

This chapter presents both published and unpublished material that I developed with Alan Rempel. I performed all of the calculations; Alan provided scientific and philosophical guidance. A preliminary version of the calculations done in the elastic limit was published in *Proceedings of the Fifth Biot Conference on Poromechanics* in July, 2013.

3.1. Introduction

In subduction zones, fluids escaping from down-going oceanic crust and sediment play an important role in governing the mode of fault behavior (e.g. seismic, creeping, slow slip) by controlling the effective stress along the plate interface. Episodic tremor and slow slip (ETS) occur at depths (~ 30 km) where the main source of fluids to the plate interface must be attributed to chemical dehydration reactions in the subducting fault material and underlying oceanic crust, rather than from porosity loss due to compaction (e.g. *Obara, 2002; Shelly et al., 2006; Liu and Rice, 2007; Peacock, 2009; Audet et al., 2009; Fagereng and Diener, 2011*). While oceanic sediments may have porosities of $\sim 50\%$ near the trench, by ~ 10 km depth the porosity of subducted sediments is reduced by an order of magnitude, to the point where mechanical compaction no longer provides a significant fluid source (*Moore and Vrolijk, 1992*). Therefore, the only significant mechanism for increasing pore pressure at relevant depths is attributed to fluid supply from chemical dehydration reactions.

Multiple lines of evidence indicate that pore pressure along subduction plate interfaces is near lithostatic at depths where slow slip and tremor are observed (*Kodiara. et al.*, 2004). Several studies have argued for the triggering of slow slip by small stress perturbations from climatic loading, a mechanism that would require a low effective stress (*Shen et al.*, 2005; *Lowry*, 2006). Similarly, other studies have found that tremor is sensitive to stress changes induced by tidal loading and passing surface waves (*Rubinstein et al.*, 2008; *Royer et al.*, 2015). Observations of anomalously high v_p/v_s ratios also support the presence of high pore pressures (*Shelly et al.*, 2006; *Audet et al.*, 2009; *Kato et al.*, 2010; *Peacock et al.*, 2011). Moreover, fault mechanics models that reproduce slow-slip behavior require high pore pressures as well (*Liu and Rice*, 2007; *Segall et al.*, 2010; *Skarbek et al.*, 2012).

Despite the abundance of evidence for high fluid pressures in the slow slip zone, only a few studies have attempted to quantify the responsible processes. There have been some studies that calculate the water content of stable mineral assemblages in subducting slabs, based on projections for the pressure and temperature in material as it is progressively buried (e.g. *Hacker et al.*, 2003; *Yamasaki and Seno*, 2003; *Peacock*, 2009; *Fagereng and Diener*, 2011). These models essentially produce static pictures of the chemically bound water content in subducting rocks as a function of pressure and temperature, and imply that fluid pressures are large wherever a reduction in bound water content is predicted. Models of this type have had success in correlating the location of chemical dehydration within the subducting slab to depths where slow slip and tremor is known to take place; however, there is little consideration of how pore pressure and porosity evolve in space and time, or how the rheology of the subducting material effects these processes (see *Katayama et al.*, 2012; *Poulet et al.*, 2014).

Slow slip in subduction zones occurs on an area of the plate interface in between the seismogenically locked and steadily creeping sections, commonly referred to as the “brittle–ductile transition zone”. In this region there is abundant evidence from laboratory experiments (*Hirth and Tullis*, 1992; *Dimanov and Dresen*, 2005; *Mehl and Hirth*, 2008), seismic data (*Eberhart-Phillips and Reyners*, 1999; *Martin and Rietbrock*, 2006; *Tsuji et al.*, 2008), and field observations (*Bebout and Barton*, 2002; *Meneghini et al.*, 2009) suggesting that, under *in situ* conditions, shear is distributed over broad zones ($\sim 10\text{--}10^3$ m) composed of rocks with marked differences in mechanical properties. This fact has been exploited in numerous models of slip on the plate interface (e.g. *Regenauer-Lieb and Yuen*, 2008; *Ando et al.*, 2010; *Daub et al.*, 2011; *Nakata et al.*, 2011; *Skarbek et al.*, 2012). These models conceive of the plate interface as consisting of brittle, seismic asperities (~ 100 m) embedded in an aseismic, ductile matrix. If this is indeed the case in nature, then such a mixed rheology has important implications for how metamorphically produced fluids are extracted and transported within the subducting material.

The situation is akin to the description of melt segregation and transport in the mantle as a two phase flow process (e.g. *McKenzie*, 1984; *Scott and Stevenson*, 1984, 1986; *Bercovici and Ricard*, 2003). In these models, relatively low viscosity melt can be extracted and focused from a more viscous, porous matrix through incompressible shear, or compressible matrix flow (*Spiegelman*, 1993a,b). The effects of compressible flow are pertinent to this study. Since the porous matrix is treated as a highly viscous fluid, it is free to expand or compact as a result of changes in pore pressure. Furthermore, if the permeability k and $\partial k/\partial\phi$ are increasing functions of porosity ϕ (as is frequently the case in geophysical settings), then propagating nonlinear porosity waves will form from any obstruction to flow (*Spiegelman*, 1993a) — for example, a

high porosity region created by melting or dehydration, or the presence of a brittle, competent block within a ductile matrix. We suggest that if large volumes of material within, or in the vicinity of the plate interface in the slow slip zone are deforming in a ductile manner, then the presence of dehydration reactions will result in the formation of porosity waves.

Here we attempt to quantify these processes by constructing a model for compaction of porous rocks in the presence of pressure and temperature-dependent dehydration reactions. There are two objectives. First, we test the feasibility of generating lithostatic pore pressures in a realistic model that includes dehydration reactions in a physical way. For this problem, we consider only elastic deformation of the subducting material, and include dehydration reactions by prescribing the magnitude of dewatering rates in temperature–pressure space. This model predicts that pressures on the order of lithostatic values are generated under a broad range of conditions, which has implications for hydrofracturing and tremor generation.

Second, we study how fluid is transported when viscous deformation of the porous matrix is included and dehydration reactions are introduced by allowing dewatering rates to vary as a function of temperature and pressure via a kinetic reaction rate law. In this model we assume that lithostatic pore pressures have already been generated, and focus on the movement of porosity and pressure through nonlinear wave behavior. Specifically, we examine the possibility that the observed periodicity of slow slip and tremor in subduction zones can be explained by the migration of porosity waves. In this scenario, excess fluid pressure induced by dehydrating rocks propagates as a porosity wavetrain. We test the hypothesis that increased pressure at the plate interface, corresponding to a peak in a traveling porosity wave, triggers a slow slip or tremor event. Our analysis suggests that given reasonable values of rock viscosity,

values of permeability at the edge of plausibility are required for porosity wavetrains to form at periods comparable to those of slow slip and tremor (~ 1 yr).

3.2. Model Overview

We simulate fluid and heat flow in a subducting slab by tracking the location of a vertically oriented, one-dimensional column of material as it moves through the subduction zone (Figure 3.1). The overburden and background temperature field that the column experiences are parameterized for the Cascadia subduction zone. The overburden is found by integrating seismically derived crustal density values, from the surface to the location of the plate interface (*Tréhu et al., 2008; Audet et al., 2009*). Since we focus on the slow slip region (~ 30 km depth), we assume a single value of 15° for the dip of the plate interface (*Tréhu et al., 2008*).

At the start of any simulation, the column is at a set depth below the locked zone, with an initial pressure equal to some fraction of the lithostatic fluid pressure, and an initial temperature determined by the thermal environment of Cascadia (*Peacock, 2009*). As a simulation progresses, the column moves through the slow slip zone and eventually it encounters the equilibrium boundary in p - T space for a dehydration reaction and begins to lose some of its chemically bound water (Figure 3.1). This fluid release is determined by either 1) published total amounts of dewatering accommodated over a narrow window of pressure and temperature variations (e.g. *Fagereng and Diener, 2011*), or 2) a nonlinear kinetic expression parameterized for a lizardite dehydration reaction (e.g. *Lasaga and Rye, 1993*). As described below, we apply the first case when deformation is assumed to take place at time scales within the elastic regime, and the second case when deformation is assumed to take place at time scales within the viscous regime.

The full model consists of four coupled partial differential equations for excess fluid pressure p (i.e. with respect to hydrostatic pressure), porosity ϕ , temperature T , and the chemically released fluid content m_d . These equations are based on mass and energy conservation laws, as well as an assumed linear visco-elastic rheology. A derivation of the governing equations is presented in the final section of this chapter (see *Model Derivation*). The pressure equation is derived from fluid mass conservation requirements, and is written as (e.g. *Walder and Nur, 1984; Wong et al., 1997; Connolly, 1997; Rice, 2006*)

$$\frac{\partial p}{\partial t} = \frac{c_m}{\mu} \frac{\partial}{\partial z} \left[k(\phi) \frac{\partial p}{\partial z} \right] - c_m \frac{\partial \phi^{\text{in}}}{\partial t} + \frac{c_m}{\rho_f} \frac{\partial m_d}{\partial t} + \gamma \dot{\sigma}_{11} , \quad (3.1)$$

where k is permeability, μ and ρ_f are the fluid dynamic viscosity and density, and $\dot{\sigma}_{11}$ is the tectonic loading rate. The effective modulus c_m and loading efficiency γ

$$c_m = \frac{(K_u - K)(K + \frac{4G}{3})}{\alpha^2(K_u + \frac{4G}{3})} , \quad \gamma = \frac{K_u - K}{\alpha(K_u + \frac{4G}{3})} , \quad (3.2)$$

are defined using G as the shear modulus, K and K_u as the drained and undrained bulk moduli, and α as the Biot parameter. Equation (3.1) gives the change in fluid pressure as a function of flow due to elastic deformation (first term on RHS), inelastic changes in porosity $\partial \phi^{\text{in}} / \partial t$ (second term), the dehydration reaction (third term), and tectonic loading (last term). Throughout this study, we assume that the pore-space forms a connected network, and that permeability obeys the relationship (e.g. *Brace, 1977; McKenzie, 1984; Connolly, 1997*)

$$k = k_0 \left(\frac{\phi}{\phi_0} \right)^n , \quad (3.3)$$

where k_0 is the permeability at reference porosity ϕ_0 .

The porosity equation is also derived from mass conservation requirements (e.g. *Rice, 2006; Brantut et al., 2011*)

$$\frac{\partial \phi}{\partial t} = \left(\frac{1}{c_m} - \frac{\phi}{K_f} \right) \frac{\partial p}{\partial t} + \frac{\partial \phi^{\text{in}}}{\partial t} - \frac{\gamma}{c_m} \dot{\sigma}_{11}. \quad (3.4)$$

where K_f is the fluid bulk modulus. Equation (3.4) gives the change in porosity due to elastic and inelastic deformations (first and second terms on RHS), as well as tectonic loading (last term). The inelastic change in porosity is given empirically by (e.g. *Connolly, 1997; Wang and fong Wong, 2003; Brantut et al., 2011*)

$$\frac{\partial \phi^{\text{in}}}{\partial t} = \frac{\xi}{\rho_f} \frac{\partial m_d}{\partial t} - \frac{3}{4\eta} p_e \phi, \quad (3.5)$$

where ξ governs porosity production due to reaction driven loss in solid mass, $p_e = g(\rho_s - \rho_f)z - p$ is the effective pressure where ρ_s is the solid density, and η is the shear viscosity of the solid matrix. The last term in equation (3.5) describes changes in porosity due to an assumed linear viscous relaxation.

The elastic constitutive behavior of the model is determined from published seismic properties for Cascadia (*Tréhu et al., 2008; Audet et al., 2009*), so that the shear modulus G , the undrained Poisson ration ν_u , and the undrained bulk modulus K_u satisfy

$$v_s = \sqrt{\frac{G}{\rho_b}}, \quad \left(\frac{v_p}{v_s} \right)^2 = \frac{2(1 - \nu_u)}{1 - 2\nu_u}, \quad K_u = \frac{2G(1 + \nu_u)}{3(1 - 2\nu_u)}. \quad (3.6)$$

The drained bulk modulus K is found by solving the following two equations simultaneously for an assumed value of α

$$\alpha = 1 - \frac{K}{K_s}, \quad K = \frac{\alpha^2 K_s K_f}{\phi K_s + (\alpha - \phi) K_f}, \quad (3.7)$$

where K_s is the solid constituent bulk modulus.

In the elastic limit, the elastic properties are allowed to change as a function of temperature and pressure via thermodynamic interpolation of the fluid properties (ρ_f, K_f) using NIST steam tables. However, for simplicity derivatives associated with these changes are ignored. In the viscous models, the elastic constants are fixed, as the focus is on the mechanical aspects of porosity wave behavior.

The temperature equation is based on energy conservation requirements, and is given by (e.g. *Connolly, 1997; Rice, 2006*)

$$C_s \frac{\partial T}{\partial t} = K_T \nabla^2 T + C_f \nabla \cdot \left(\frac{k}{\mu} T \nabla p \right) + \nabla \cdot \left(\frac{k}{\mu} p \nabla p \right) - L \frac{\partial m_d}{\partial t} - \sigma_{ij} \dot{\epsilon}_{ij} + \frac{g \rho_f k}{\mu} \nabla p \cdot \nabla z_{\text{elev}}. \quad (3.8)$$

This equation states that the change in temperature is due to conduction (first term on RHS), advective transport and work due to fluid flow (second and third terms), the latent heat of the dehydration reaction (fourth term), work done by elastic deformations (fifth term), and changes in gravitational potential energy (last term). Equations (3.1), (3.4) along with (3.5), and (3.8) are the governing equations for the model, and are completed by the specific formulation of the dehydration source $\partial m_d / \partial t$.

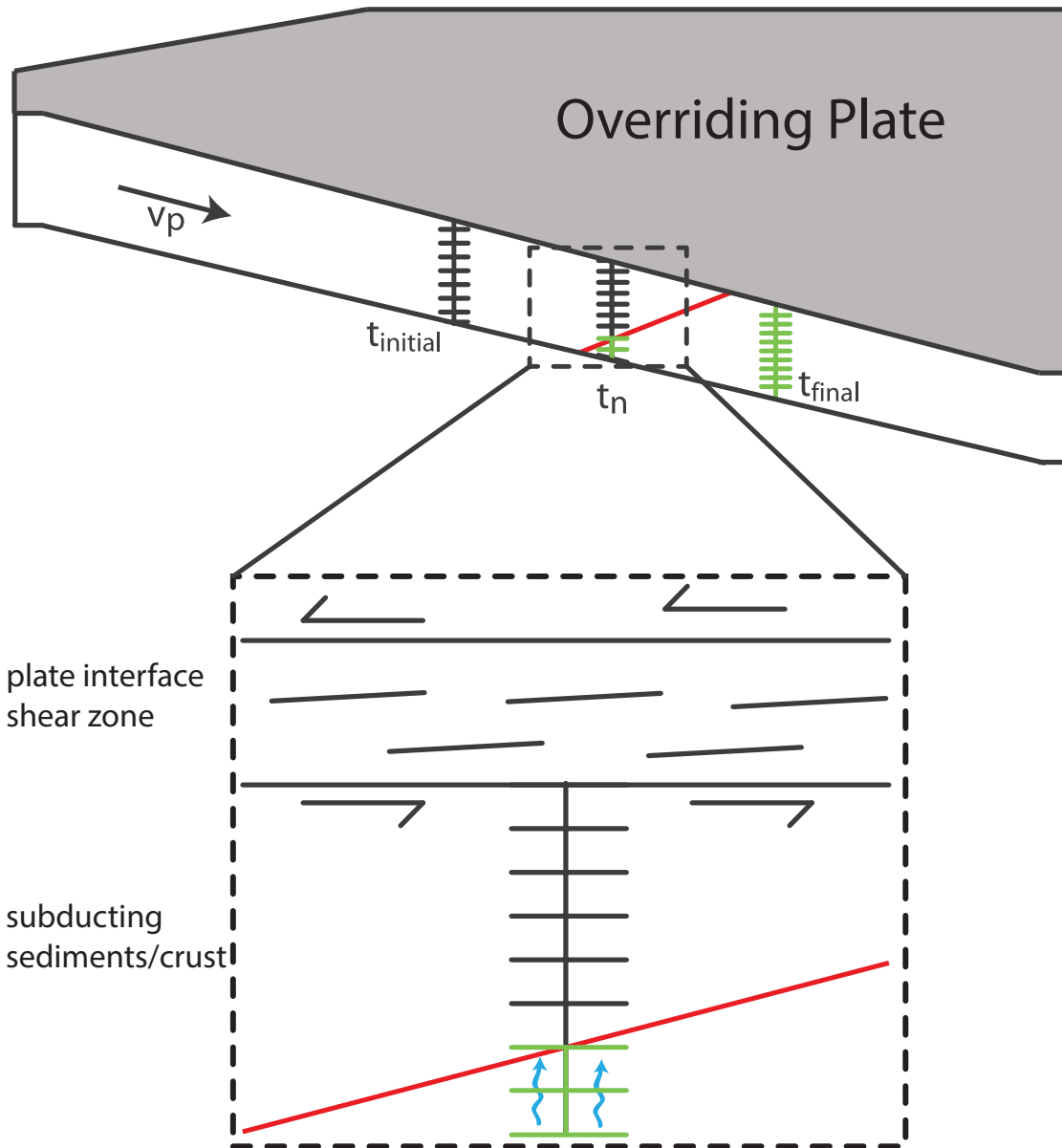


FIGURE 3.1. Subduction of a column of rock (black and green grids) is initiated at a known depth below the locked zone. Material crossing the equilibrium boundary (red line, green grid points) of a relevant dehydration reaction loses its chemically bound water at a prescribed rate, or at a rate controlled by the local offset from the equilibrium curve in $p - T$ space.

3.2.1. Dehydration Reactions

We consider two example reaction types: 1) a generalized mid-ocean ridge basalt reaction, and 2) dehydration of antigorite serpentinite. To put these reactions into the proper context, it is necessary to review some characteristics of the subduction zone plate interface in the slow slip region.

Numerous subduction zones around the world contain a seismic low velocity zone (LVZ), generally interpreted as hydrated, subducting oceanic crust (e.g. *Yuan et al.*, 2000; *Ferris et al.*, 2003; *Li et al.*, 2003; *Kawakatsu and Watada*, 2007; *Tibi et al.*, 2008; *Audet et al.*, 2010; *Hansen et al.*, 2012). In Cascadia for example, the LVZ is an ~ 8 km thick layer that disappears beneath the mantle wedge corner (*Rondenay et al.*, 2008; *Audet et al.*, 2010). The disappearance of the LVZ is associated with basalt-to-eclogite dehydration reactions within subducting mid-oceanic ridge basalt (*Rondenay et al.*, 2008; *Audet et al.*, 2010; *Fagereng*, 2011). Together with evidence for high fluid pressures in the slow slip zone just up-dip of the mantle wedge corner, these observations seem to indicate that the plate interface acts as a low permeability seal, trapping fluids from dehydrating crust in the slow slip zone (*Audet et al.*, 2010; *Hansen et al.*, 2012).

In addition to these arguments, there is also evidence for the presence of a “serpentinized subduction channel” in the vicinity of the mantle wedge corner. Such a structure has been invoked to explain the presence of high-pressure metamorphic rocks on the Earth’s surface, which indicate the existence of some mechanism for transporting material from depths of ~ 100 km in subduction zones (see *Guillot et al.*, 2009). Field and numerical studies point to the formation of a ~ 1 to 10 km thick melange shear zone, composed of competent oceanic peridotite blocks in an incompetent, serpentinized matrix (e.g. *Cloos*, 1986; *Blake et al.*, 1995; *Hermann*

et al., 2000; *Schwartz et al.*, 2001; *Gerya et al.*, 2002; *Hilaireret and Reynard*, 2009; *Blanco-Quintero et al.*, 2011). In this picture, deformation within the subduction channel is accommodated almost entirely within the serpentized matrix (*Cloos*, 1986; *Blake et al.*, 1995; *Hermann et al.*, 2000; *Breeding et al.*, 2003). Additionally, there is evidence that the serpentized matrix is dehydrating, and that resultant fluid flow is also accommodated largely within the matrix (*Breeding et al.*, 2003).

Thus, there appears to be two areas of active dehydration in the vicinity of the slow slip zone: 1) dehydration of basalt within elastically deforming subducting crust, and 2) dehydration of viscously deforming serpentinite within the subduction channel. These two sources likely interact in some way to generate high fluid pressures that are associated with episodic tremor and slip. In this work we consider in turn, both types of dehydration.

3.2.1.1. Basalt Dehydration, Elastic Limit

In the elastic limit, we use the results of *Fagereng et al.* (2011) to parameterize a general basalt dehydration reaction relevant to the Cascadia subduction zone. In this formulation the dehydration reaction rate depends linearly on the change in pressure and temperature. Accordingly, we assume that the dewatering rate $\partial m_d / \partial t$ is proportional to the change in concentration of chemically bound water in the solid matrix c_s , so that

$$\frac{\partial m_d}{\partial t} = -\rho_s(1 - \phi^0) \frac{\partial c_s}{\partial t} = -\rho_s(1 - \phi^0) \left(\alpha_p \frac{\partial p}{\partial t} + \alpha_T \frac{\partial T}{\partial t} \right), \quad (3.9)$$

where $\alpha_p = \partial c_s / \partial p$ and $\alpha_T = \partial c_s / \partial T$. The concentration of bound fluid within the solid constituent $c_s = c_s(p_{\text{tot}}, T)$ is treated as a known function of total fluid

pressure p_{tot} and temperature T (Dahlen, 1992). Fagereng and Diener (2011) have suggested that for relevant depths in Cascadia, c_s is mainly controlled by water release due to the breakdown of chlorite and glaucophane to form hornblende and epidote. Thermodynamic models indicate that ~ 1 wt% H_2O is released during these reactions, with the rocks initially containing ~ 2 wt% H_2O (Hacker et al., 2003; Peacock, 2009; Fagereng and Diener, 2011). We use the results of Fagereng and Diener (2011) to estimate changes in water content, which we accommodate over a narrow range of temperature and pressure conditions (1°C , 0.7 GPa) $\alpha_p = -1.4 \times 10^{-10} \text{ Pa}^{-1}$ and $\alpha_T = -5 \times 10^{-4} \text{ K}^{-1}$. Then the value of c_s is controlled based on the location of the subducting column relative to a single boundary in pressure–temperature space (Figure 3.2). At each point, the total fluid pressure is approximated by the overburden σ_{11} due to the weight of overlying material. For simplicity, we assume that temperature varies linearly with depth within the column, and evolves according to a fixed temperature gradient of $20^\circ\text{C}/\text{km}$ (e.g. Peacock, 2009).

3.2.1.2. Serpentinite Dehydration, Viscous Limit

A serpentinite-like dehydration reaction is included in the viscous model through a kinetic expression that depends nonlinearly on the total fluid pressure and temperature (Lasaga and Rye, 1993; Ague et al., 1998; Connolly, 1997)

$$\frac{\partial m_d}{\partial t} = sM_{\text{H}_2\text{O}} \left(1 - \frac{m_d}{m_d^0}\right) A |\Delta G(p_{\text{tot}}, T)|^{n_r} c_0 \exp \left[\frac{E_a}{R} \left(\frac{1}{T} - \frac{1}{T_0} \right) \right], \quad (3.10)$$

where A is the surface area of the rate-limiting mineral, c_0 and n_r are empirical reaction constants, E_a is the reaction activation energy, $M_{\text{H}_2\text{O}}$ is the molar mass of water, m_d^0 is the total chemically released water content, R is the gas constant,

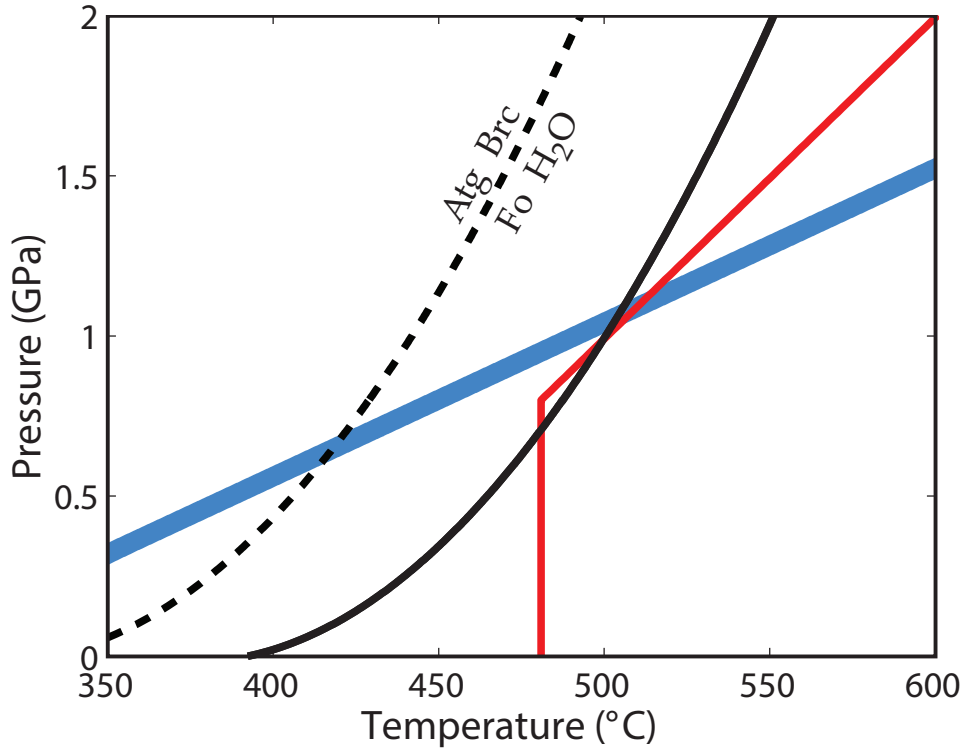


FIGURE 3.2. Pressure-temperature space showing the location of a generalized reaction boundary (red line), estimated from *Fagereng and Diener (2011)* for the breakdown of chlorite and glaucophane to form hornblende and epidote, and the equilibrium boundaries for reaction (3.11) (black dashed line) and the shifted reaction (solid black line). The blue shaded region shows the path of the subducting column path assuming lithostatic pore pressure and temperature as described in the text.

$\Delta G(p_{\text{tot}}, T)$ is the Gibbs free energy associated with the reaction, T_0 is a reference temperature for the reaction, and s is a reaction index that takes the value 0 if $\Delta G \geq 0$, and 1 otherwise.

Our model reaction is the low-temperature antigorite dehydration reaction



The general form of the equilibrium curve for equation (3.11) is computed using the thermodynamic software package SUPCRT92 (*Johnson et al., 1992*). For ease of

numerical computation, the equilibrium curve is shifted towards higher temperatures by $\sim 50^\circ\text{C}$, so that it intersects the general $p - T$ path of the subducting material at approximately the same location as the model basalt dehydration reaction (Figure 3.2). Material to the right of the boundary will dehydrate according to equation (3.10), while $\partial m_d / \partial t = 0$ for material to the left of the boundary. Finally, because experimental data on the kinetics of reaction (3.11) are lacking, values for the remaining parameters in equation (3.10) are taken from published experimental studies on the dehydration of lizardite, and can be found (with references) in Table 3.1.

3.3. Elastic Limit and Prescribed Dehydration

In the elastic limit all inelastic deformations are ignored (see below), and the pressure equation (3.1) can be rewritten as a single governing equation for excess fluid pressure. Expanding the first term on the RHS of (3.1) gives

$$\frac{\partial}{\partial z} \left[k(\phi) \frac{\partial p}{\partial z} \right] = \frac{dk}{d\phi} \frac{\partial \phi}{\partial z} \frac{\partial p}{\partial z} + \frac{\partial^2 p}{\partial z^2}, \quad (3.12)$$

and from the general change in porosity given by equation (3.77), if the inelastic change in porosity is ignored then

$$\frac{\partial \phi}{\partial z} = \frac{K_f - c_m \phi}{c_m (K_f + p)} \frac{\partial p}{\partial z}, \quad (3.13)$$

TABLE 3.1. Parameter definitions and nominal values used in model simulations.

Symbol	Definition	Value	Reference or Equation
A	effective surface area of rate limiting mineral	201 m^{-1}	<i>Connolly (1997)</i>
c_0	reaction rate constant	$1.29 \times 10^{-20} \frac{\text{mol}}{\text{m}^2} \left(\frac{\text{cal}}{\text{mol}}\right)^{n_r}$	<i>Ague et al. (1998)</i>
c_m	elastic parameter	49 GPa	(3.2)
C_f	fluid specific heat	$4 \times 10^6 \text{ J m}^{-3} \text{ K}^{-1}$	<i>Connolly (1997)</i>
C_r	rock specific heat	$2.5 \times 10^6 \text{ J m}^{-3} \text{ K}^{-1}$	<i>Connolly (1997)</i>
E_a	reaction activation energy	$2 \times 10^4 \text{ cal mol}^{-1}$	<i>Lasaga and Rye (1993)</i> <i>Ague et al. (1998)</i>
G	shear modulus	26 GPa	(3.6)
ΔG	reaction Gibbs energy	cal mol^{-1}	
k	permeability	m^2	(3.3)
K	drained bulk modulus	106 GPa	(3.7)
K_f	fluid bulk modulus	2.9 GPa	
K_T	thermal conductivity	2.5 W (m K)^{-1}	<i>Connolly (1997)</i>
K_u	undrained bulk modulus	108 GPa	(3.6)
L	latent heat of reaction	500 kJ kg^{-1}	<i>Brantut et al. (2011)</i>
m_d	chemically released fluid content	kg m^{-3}	
$M_{\text{H}_2\text{O}}$	H ₂ O molar mass	18 g mol^{-1}	
n_r	reaction law order	3.64	<i>Ague et al. (1998)</i>
n_ϕ	permeability law order	3	<i>Brace (1977)</i>
p	pressure	Pa	
R	gas constant	$1.987 \text{ cal (mol K)}^{-1}$	
T	temperature	K	
T_0	reaction reference temperature	633 K	<i>Ague et al. (1998)</i>
v_p	p-wave velocity	7 km s^{-1}	<i>Tréhu et al. (2008)</i>
v_p/v_s	seismic velocity ratio	2.35	<i>Audet et al. (2009)</i>
α	Biot-Willis parameter	0.2	(3.7)
γ	loading efficiency		(3.2)
η	shear viscosity	Pa s	
μ	fluid viscosity	$2 \times 10^{-4} \text{ Pa s}$	
ν	Poisson ratio	0.39	<i>Audet et al. (2009)</i>
ϕ	porosity		
ρ_f	fluid density	1000 kg m^{-3}	
ρ_s	solid density	3000 kg m^{-3}	
$\dot{\sigma}$	tectonic loading rate	$1 \times 10^{-5} \text{ Pa s}^{-1}$	
ξ	plastic compaction parameter	0.1 – 1 unitless	

Putting the above results into (3.1) and taking all of the moduli constant yields

$$\begin{aligned} \frac{\partial p}{\partial t} = & \left[1 + \frac{c_m \rho_s^0}{\rho_f} (1 - \phi^0) \alpha_p \right]^{-1} \left\{ \frac{c_m k}{\mu} \frac{\partial^2 p}{\partial z^2} + \frac{1}{\mu} \left(\frac{K_f - c_m \phi}{K_f + p} \right) \frac{dk}{d\phi} \left(\frac{\partial p}{\partial z} \right)^2 - \gamma \dot{\sigma}_{11} \right. \\ & \left. - \frac{c_m \rho_s^0}{\rho_f} (1 - \phi^0) \alpha_T \frac{\partial T}{\partial t} \right\} . \end{aligned} \quad (3.14)$$

Since α_p is either zero or a negative number (the concentration of bound water decreases with increasing pressure across the reaction boundary in p - T space), the leading coefficient on the RHS of (3.14) reveals a limit on the magnitude of α_p .

$$|\alpha_p| \leq \frac{\rho_f}{c_m \rho_s (1 - \phi^0)} \approx 4.6 \times 10^{-12} \text{ Pa}^{-1} . \quad (3.15)$$

Physically, the value of α_p is determined by the petrologic phase behavior. Equation (3.15) is a mechanical constraint on this behavior in the context of poro-elastic diffusion, since for the problem to remain physical the diffusivity must be greater than zero to satisfy the second law of thermodynamics.

3.3.1. Dimensionless Equations

Some simple analysis can yield estimates of dehydration rates necessary to generate lithostatic fluid pressures on the time scale of slow slip events. Consider the following dimensionless variables

$$z' = \frac{z}{H}, \quad t' = \frac{t}{t^*}, \quad p' = \frac{p}{p^*}, \quad \phi' = \frac{\phi}{\phi_0},$$

and choose

$$t^* = \frac{\mu H^2}{k c_m}, \quad p^* = g(\rho_s - \rho_f)H = g\Delta\rho H ,$$

where ϕ_0 is the initial porosity and H is the thickness of the dehydrating region. Then equation (3.1) in the elastic limit, with constitutive parameters taken as constants, can be written as

$$\frac{\partial p'}{\partial t'} = \frac{\partial^2 p'}{\partial z'^2} - \left(\frac{\phi_0 c_m}{g\Delta\rho H} \right) \frac{\partial \phi'^{\text{in}}}{\partial t'} + \left(\frac{\mu H}{gk\Delta\rho} \right) \Gamma + \gamma \dot{\sigma}'_{11} , \quad (3.16)$$

where $\Gamma = (\partial m_d / \partial t) / \rho_f$ is the dehydration rate defined as the mass of water released per unit bulk rock mass per unit time. By ignoring inelastic deformation we are assuming that $\phi_0 c_m \ll g\Delta\rho H$. The third term will contribute significantly to pore pressure development when its magnitude is of order unity. This leads to a condition on the dehydration rate

$$\Gamma_0 = \frac{gk\Delta\rho}{\mu H} . \quad (3.17)$$

Evaluating equation (3.17) using parameter values (see Table 3.1) appropriate to the slow slip zone (~ 35 km depth) at Cascadia, a permeability of 10^{-20} m², and a 1000 m thick dehydrating section yields a dehydration rate of $\Gamma_0 = 8 \times 10^{-16}$ s⁻¹. This is the rate necessary to generate excess pressures significantly above hydrostatic. Generation of lithostatic pore pressures will require dehydration rates $\gg \Gamma_0$.

The time scale of dehydration in the elastic regime is highly dependent on the thickness of the reaction zone. For the calculation in the last paragraph the time scale is $t^* = 13000$ years, which is much larger than the recurrence interval of tremor and slow slip. However, if the reaction zone is 10 m thick, rather than 1000 m, then the time scale is $t^* = 1.3$ years.

At this point it is useful for comparison to review some simple estimates of permeability and dewatering due to dehydration for subduction zone slow slip. To maintain near lithostatic pore pressures at relevant depths, permeabilities must be relatively low given estimated rates of fluid release due to dehydration reactions (*Audet et al.*, 2009; *Peacock*, 2009; *Peacock et al.*, 2011). At Cascadia, *Hyndman and Peacock* (2003) estimate a fluid production rate due to dehydration of $10^{-4} \text{ m}^3/(\text{m}^2\text{yr})$. Using this fluid production rate along with Darcy's law, *Audet et al.* (2009) suggest that the plate interface acts as a low permeability seal, with permeability values of 5×10^{-25} to $5 \times 10^{-22} \text{ m}^2$ for shear zone thicknesses of 1 to 1000 m. *Peacock et al.* (2011) perform a similar calculation and estimate a permeability of 10^{-24} to 10^{-21} m^2 , assuming a fluid production rate twice that obtained by *Hyndman and Peacock* (2003). *Peacock et al.* (2011) also point out that high pore pressure could be maintained if the entire layer of subducted oceanic crust has a low permeability, rather than just the plate interface. In this case, they estimate that the subducted crust has a permeability of $< 3 \times 10^{-20} \text{ m}^2$, corresponding to crystalline rocks with a fluid filled porosity of 2.7% to 4.0%, assuming nearly lithostatic pore pressure.

We are interested in what dehydration rates are necessary to generate lithostatic pore pressures over a 14 month time span (the average slow slip recurrence interval at Cascadia). It can be imagined that in the most extreme case, the pore pressure reduces to the hydrostatic value every time a slow slip event occurs, and increases to close to the lithostatic value during the period between events. For permeabilities less than 10^{-18} m^2 , simulations of equation (3.16) show that a dewatering rate of $\sim 2 \times 10^{-12} \text{ s}^{-1}$ is sufficient to generate pore pressures greater than lithostatic values in the upper few hundred meters of the subducting column, from an initial hydrostatic fluid pressure over a period of ~ 14 months (Figure 3.3). The source term is applied

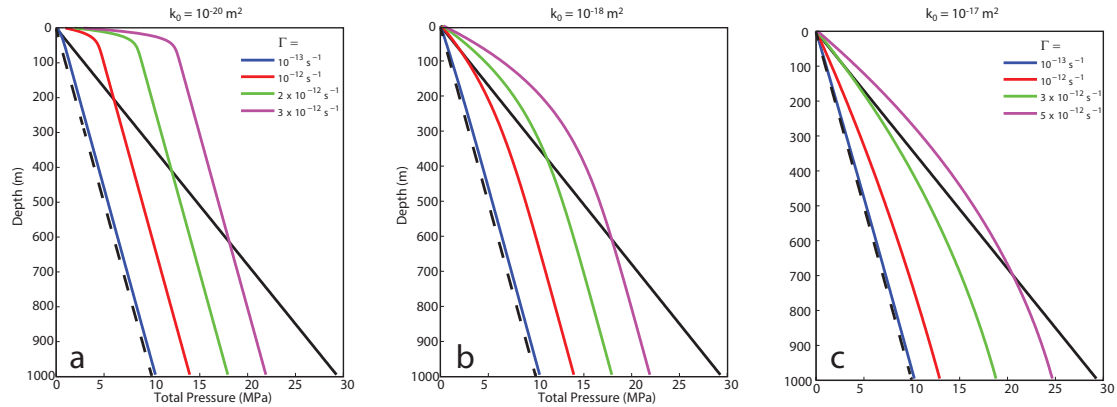


FIGURE 3.3. Pressure profiles for three values of permeability and values of Γ indicated by the legends. The colors in panel (b) correspond to those in panel (c). All simulations were run for 14 months, with hydrostatic initial conditions, a hydrostatic upper boundary, and a no-flow lower boundary. Hydrostatic and lithostatic pressure profiles are shown by the dashed and solid black lines.

to the entire column for these simulations, so these values can be interpreted as a lower bound on the reaction rate Γ . The simulated dewatering rate can be converted to a flux by considering a 1 m^3 volume of bulk rock and assuming that all released water flows through its upper surface. Then the dewatering rate becomes

$$\Gamma = 2 \times 10^{-12} \frac{\text{kg}_{\text{fluid}}}{\text{kg}_{\text{rock}} \cdot \text{s}} \cdot \frac{3000 \text{ kg}_{\text{rock}}}{\text{m}^3} \cdot \frac{\text{m}^3}{1000 \text{ kg}_{\text{fluid}}} \cdot 1 \text{ m} \cdot \frac{1000 \text{ mL}}{10^{-3} \text{ m}^3} \cdot \frac{31536000 \text{ s}}{\text{yr}} \approx 190 \frac{\text{mL}}{\text{m}^2 \text{ yr}}.$$

For permeabilities less than 10^{-20} m^2 , the necessary dewatering rate is half this value, so we can estimate a dewatering rate in the range $\Gamma = 85 - 190 \text{ mL m}^{-2} \text{ yr}^{-1}$, which compares well with the value reported by *Hyndman and Peacock (2003)*. Permeabilities larger than 10^{-18} m^2 require potentially unrealistic dehydration rates to produce lithostatic excess pressure. For example, a simulation with $k_0 = 10^{-17} \text{ m}^2$ required a dehydration rate $> 470 \text{ mL m}^{-2} \text{ yr}^{-1}$.

3.3.2. Results

Simulations of equation (3.14) employ a boundary condition formulated to mimic the presence of an impermeable layer, or cap, overriding the subducting column; in these models this layer corresponds to the plate interface shear zone (Figure 3.1, (e.g. *Skarbek and Rempel, 2013*). We assume that pore pressure at the upper surface of the cap is hydrostatic, and equate the fluid flux across the upper and lower surfaces, so that

$$q_{\text{cap}} = -\frac{k_{\text{cap}}}{z_{\text{cap}}}p_0 = \frac{k_0}{2\Delta z}(p_{-1} - p_1) . \quad (3.18)$$

This condition results in a time rate of change of pore pressure at the upper boundary of the subducting column proportional to

$$\frac{\partial p_0}{\partial t} \propto -\frac{k_{\text{cap}}\Delta z}{k_0 z_{\text{cap}}} . \quad (3.19)$$

A zero flux condition is applied at the subducting column’s base. Finally, equation (3.14) is integrated by applying the method of lines and using a fourth-order Runge-Kutta method in MATLAB. We ran two groups of simulations, the first varying permeability of the subducting column as well as the overriding cap layer, and a second set varying the column permeability and the cap layer thickness.

In the first group of simulations, values of the cap and initial column permeability are in the range $10^{-25} - 10^{-23} \text{ m}^2$, covering the scope of estimated permeabilities for subducting material at slow slip depths in Cascadia. In the second group, k_{cap} is kept constant and z_{cap} is varied from 10–1000 m, which covers the estimated range of shear zone thickness at relevant depths *Audet et al. (2009)*. All other parameters are kept constant throughout the suite of simulations. Each simulation is initiated at a depth of 30 km, within the frictional transition zone at Cascadia, (*Burgette et al.*,

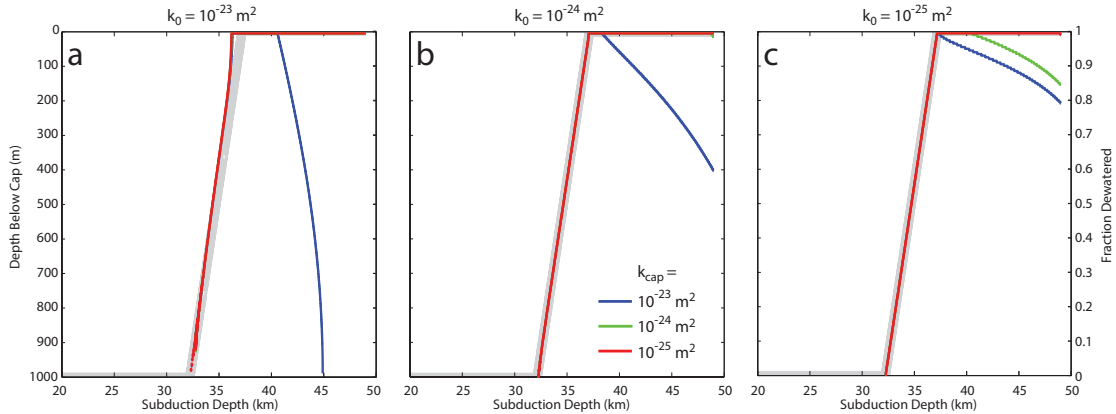


FIGURE 3.4. Results for simulations varying the permeability of the column k_0 as well as that of the cap k_{cap} . In all simulations shown here the cap thickness is set to $z_{\text{cap}} = 10$ m. Colored lines show the minimum depth below the upper boundary to negative effective stress within the subducting column. The grey shaded region shows the fraction of the column that has crossed the reaction boundary and dewatered.

2009) with initial porosity of 5%. Under these conditions, the permeability at any point in the subducting column does not vary substantially from its initial value.

Figures 3.4 and 3.5 show the minimum depth at which pressures above lithostatic are predicted for the range of permeabilities shown. Below this depth the model predicts a state of negative effective stress. Each panel also shows the fraction of the subducting column that has crossed the reaction boundary. Since the temperature increases with depth, the reaction begins at the base of the subducting column and proceeds smoothly upward until the entire column has crossed the boundary. The reaction source term is relatively constant across the span of model parameters, and is in the range $\Gamma = 2.2\text{--}3.6 \times 10^{-11} \text{ s}^{-1}$ for each simulation shown. This is approximately one order of magnitude above the estimated value in the previous section; however there the dehydration source is applied to the entire column, whereas here it is applied to an ~ 10 m thick section at any given time, due to the movement of the reaction boundary.

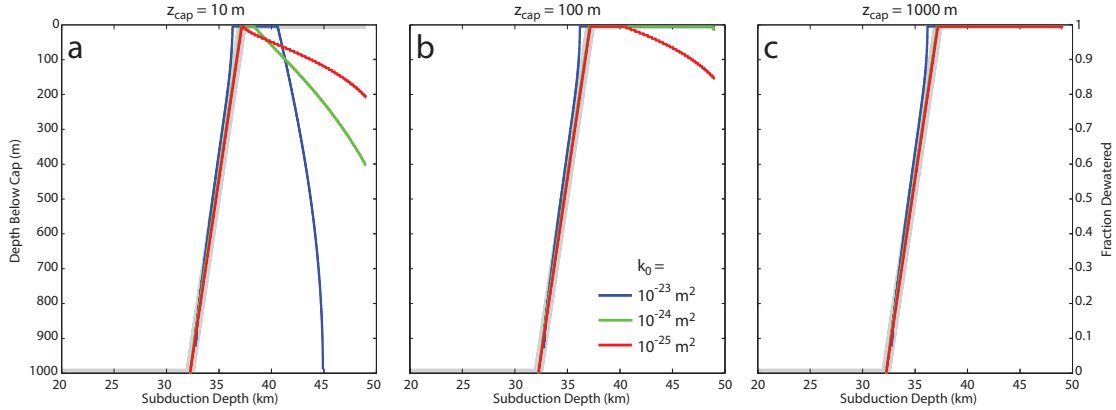


FIGURE 3.5. Results for simulations varying the permeability of the column k_0 and the thickness of the cap z_{cap} . In all simulations shown here the cap permeability is set to $k_{\text{cap}} = 10^{-24} \text{ m}^2$. Colored lines show the minimum depth below the upper boundary to negative effective stress within the subducting column. The grey shaded region shows the fraction of the column that has crossed the reaction boundary and dewatered.

A robust feature of all simulations is the generation of pore pressure in excess of the local lithostatic values. Pressures in excess of the lithostatic value are generated as soon as the reaction begins at the base of the column and track the location of the reaction front as it moves up the column. In simulations with relatively high column permeability ($k_0 = 10^{-23} \text{ m}^2$), the location of zero effective stress is able to move up the column slightly ahead of the reaction front. In all simulations, the entire column is pressurized above lithostatic values when the reaction front reaches the upper boundary of the column. Depending on the thickness and permeability of the cap layer, this condition may persist for the remainder of the simulation.

3.3.3. Summary

Our results show that basalt dehydration can reasonably generate lithostatic pore pressures within the slow slip zone. Dimensional analysis of the pore pressure

equation suggests that reaction zones within the subducting material must be 10s of meters thick to generate large pore pressures at time scales comparable to ETS recurrence intervals. In the next section, we show that predictions based on the kinetic dehydration law support this conclusion.

The common occurrence of pressures above lithostatic values in these simulations suggests the presence of hydraulic fracturing (e.g. *Skarbek and Rempel, 2013*). In these cases the fluid pressure generated due to dehydration reactions is greater than the least principle stress and hydraulic fractures may form if the tensile strength of the rocks is exceeded. The creation of such fractures would be expected to greatly alter the bulk permeability of the subducting material. Models for slow slip and tremor indicate that tremor is produced by frictional slip (e.g. *Ide et al., 2007; Shelly et al., 2007b*), although when it was first discovered it was suggested that tremor radiated as a result of dehydration reaction-induced hydraulic fracturing (*Obara, 2002*). However, if there is a significant amount of viscously deforming material in the plate interface it may impede or prevent hydro-fracturing. In the next section we examine the effects of dehydration reactions in a viscously deforming porous medium.

3.4. Viscous Limit and Reaction Kinetics

In this section we present results from simulations of the full model defined by the pressure (3.1) and porosity (3.4) equations, inelastic changes in porosity (3.5), and the temperature equation (3.8), along with the kinetic formulation of dehydration described in Section 4.2. The objective here is to study the time scales and mechanics of reaction-generated fluid transport, under the assumption that lithostatic pore pressure have already been generated. The results show that reaction-driven increases in porosity are propagated through the subducting column as solitary pressure and

porosity waves. This behavior is due to inelastic changes in porosity due to the viscous behavior included in equation (3.5). Finally, we show that extreme values of rock shear viscosity and permeability are required for these waves to propagate with periods similar to the recurrence interval of slow slip and tremor (~ 1 year).

In the viscous simulations, the initial pressure in the subducting column is uniformly lithostatic (i.e. effective stress is zero). Because of the viscous term in equation (3.5), this is the only stable initial condition. This condition implies the presence of a uniform background fluid flux

$$q_0 = \frac{gk(\phi_0)\Delta\rho}{\mu}, \quad (3.20)$$

where ϕ_0 is the initial porosity of the column. To maintain this initial condition as a steady state we require that pressure at the base of the column increases with time according to the tectonic loading rate. At the upper boundary a non-reflecting, or absorbing boundary condition is applied. This condition is formulated to maintain the initial condition as a steady state and to prevent any pressure/porosity waves impinging on the upper boundary from reflecting back into the column (e.g. *Engquist and Majda, 1977*).

The initial temperature profile is defined by the initial depth of the column and a geothermal gradient of 20 K/km. Temperature at the lower boundary is set to increase at a rate determined by the dip angle of the subducting slab, the plate convergence velocity, and the background temperature field (*Tréhu et al., 2008; Peacock, 2009*). Additionally, the background fluid flux implies the presence of a background heat transport due to the advective terms in equation (3.8). In order to achieve a steady state initial condition, this background heat transport is subtracted off of equation (3.8). Finally, the governing equations along with the initial and boundary conditions

are solved in MATLAB using the method of lines and standard ODE integration schemes.

3.4.1. Dimensionless Equations

The pressure and porosity equations (3.1) and (3.4) can be made dimensionless by first defining the compaction length

$$\delta_0 = \left(\frac{4\eta k_0}{3\mu\phi_0} \right)^{1/2}, \quad (3.21)$$

which is the natural length scale for viscous deformation (*McKenzie*, 1984; *Spiegelman*, 1993a). The natural velocity scale is the buoyant seepage velocity

$$v_0 = \frac{4g\Delta\rho\delta_0^2}{3\eta} = \frac{g\Delta\rho k_0}{\phi_0\mu}, \quad (3.22)$$

where $g\Delta\rho\delta_0 = g(\rho_s - \rho_f)\delta_0$ is the buoyant pressure over the compaction length, and $v_0\eta/\delta_0$ is the viscous pressure drop associated with strain rate v_0/δ_0 . Together, δ_0 and v_0 define a viscous compaction time

$$\tau_0 = \frac{4\eta}{3g\Delta\rho\delta_0}. \quad (3.23)$$

And now a set of dimensionless variables may be defined as

$$t' = \frac{t}{\tau_0}, \quad z' = \frac{z}{\delta_0}, \quad p' = \frac{p}{g\Delta\rho\delta_0}, \quad \phi' = \frac{\phi}{\phi_0}, \quad m'_d = \frac{m_d}{m_d^0}.$$

Using this set of variables and assuming all material properties are constant, equations (3.1), (3.4) and (3.5) become

$$\text{De}_p \frac{\partial p}{\partial t} = \frac{\partial}{\partial z} \left(\phi^n \frac{\partial p}{\partial z} \right) - \frac{\partial \phi^{\text{in}}}{\partial t} + \mathcal{K} \frac{\partial m_d}{\partial t} + \gamma \text{De}_p \dot{\sigma}_{11} \quad (3.24)$$

$$\frac{\partial \phi}{\partial t} = \text{De}_p \frac{\partial p}{\partial t} - \text{De}_\phi \phi \frac{\partial p}{\partial t} + \frac{\partial \phi^{\text{in}}}{\partial t} - \gamma \text{De}_p \dot{\sigma}_{11} \quad (3.25)$$

$$\frac{\partial \phi^{\text{in}}}{\partial t} = \xi \mathcal{K} \frac{\partial m_d}{\partial t} - \phi p_{\text{eff}}, \quad (3.26)$$

where the primes have been dropped and the following dimensionless constants are defined

$$\text{De}_p = \frac{g \Delta \rho \delta_0}{\phi_0 c_m}, \quad \text{De}_\phi = \frac{g \Delta \rho \delta_0}{K_f}, \quad \mathcal{K} = \frac{m_d^0}{\phi_0 \rho_f}.$$

The first two terms are referred to as “Deborah” numbers, and measure the importance of elastic deformations relative to viscous deformation (*Reiner*, 1964; *Connolly and Podladchikov*, 1998). The last term, referred to here as the “Jenny” number, is the ratio of chemically bound fluid mass to the fluid mass present in the pore space in the initial state defined by ϕ_0 . Thus, the Jenny number is a material parameter that measures the importance of the dehydration source and is between 1 – 50 for the parameters used here.

It is reasonable to assume that porosity waves form on the order of the compaction time. If this is the case, then equation (3.21) and (3.22) define a

relationship between the shear viscosity and the permeability at a given period

$$\eta = \frac{3k_0(g\Delta\rho\tau_0)^2}{4\phi_0\mu}. \quad (3.27)$$

Setting $\tau_0 = 1$ year (approximately the period of slow slip events in Cascadia) and taking $\phi_0 = 0.01 - 0.1$ results in the relationship shown in Figure 3.6, which implies that triggering slow slip events in this manner requires values of viscosity and permeability that may be difficult to achieve. The viscosity at the top of the subducting column can be estimated for the Cascadia $p - T$ path (shown in Figure 3.2) by using the experimental data of *Hilaireret et al.* (2007) for antigorite. *Hilaireret et al.* (2007) give the viscosity as a power law function of strain rate, pressure, and temperature. The shaded region in Figure 3.6 corresponds to viscosity values calculated for a 1 to 1000 m thick plate interface sheared at the plate convergence rate for Cascadia, $v_{\text{plate}} \approx 3.7$ cm/year. To achieve a 1 year recurrence interval with the calculated viscosity values, Figure 3.6a shows that permeabilities in the range 5×10^{-14} to 10^{-10} m² are required, values that can only be achieved if a well connected network of fractures exists. Certain authors have suggested this scenario. On the other hand, for permeability values estimated in the elastic model results (10^{-25} to 10^{-20} m²), the shear viscosity must be within the range 10^4 to 10^9 Pa s, which is several orders of magnitude lower than the viscosity of ice (*Cuffey and Paterson*, 2010).

Using the same dimensionless variables defined above, the temperature equation (3.8) can be made dimensionless by scaling temperature by the reaction reference temperature T_0 . Then in one dimension

$$\frac{\partial T}{\partial t} = \Pi_1 \frac{\partial^2 T}{\partial z^2} + \Pi_2 \frac{\partial}{\partial z} \left(\phi^n T \frac{\partial p}{\partial z} \right) + \Pi_3 \frac{\partial}{\partial z} \left(\phi^n p \frac{\partial p}{\partial z} \right) - \Pi_4 L \frac{\partial m_d}{\partial t} - \Pi_5 \sigma_{11} \left(\dot{\sigma}_{11} + \alpha \frac{\partial p}{\partial t} \right) + \Pi'_3 \frac{\partial p}{\partial z}, \quad (3.28)$$

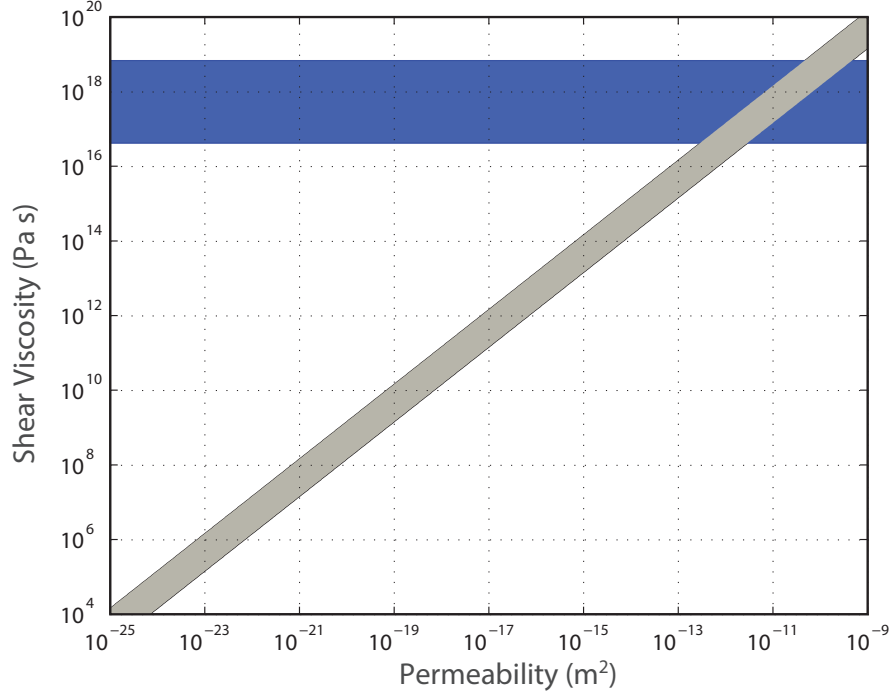


FIGURE 3.6. Plot of the relationship, equation (3.27), between permeability and viscosity for a compaction time $\tau_0 = 1$ year. The grey shaded region shows this relationship for porosities 0.01 to 0.1. The blue shaded region shows viscosities calculated using the results of *Hilaiet et al.* (2007), for strain rates corresponding to plate interface thicknesses of 1 to 1000 m.

where

$$\Pi_1 = \frac{4\eta K_T}{3C_s g \Delta \rho \delta^3}, \quad \Pi_2 = \frac{C_f \phi_0}{C_s}, \quad \Pi_3 = \frac{g \Delta \rho \delta \phi_0}{C_s T_0}, \quad \Pi_4 = \frac{L m_d^0}{C_s T_0}, \quad \Pi_5 = \frac{(g \Delta \rho \delta)^2}{C_s T_0 (K + \frac{4G}{3})},$$

and Π'_3 is equal to Π_3 with $\Delta \rho$ replaced by ρ_f . The fifth term is negligibly small, and in the small porosity limit ($\phi_0 \ll 1$), Π_2 , Π_3 , and Π'_3 are as well. So the only significant processes are temperature changes due to conduction and the dehydration reaction.

3.4.2. Results

The parameter values given in Table 3.1 result in $De_p, De_\phi \approx 10^{-4}$, in which case the elastic terms in equations (3.24) and (3.25) may be ignored. Then the pressure equation becomes

$$0 = \frac{\partial}{\partial z} \left(\phi^n \frac{\partial p}{\partial z} \right) + \mathcal{K}(1 - \xi) \frac{\partial m_d}{\partial t} + \phi p_e, \quad (3.29)$$

and the only changes in porosity are those due to inelastic effects, so that

$$\frac{\partial \phi}{\partial t} = -\phi p_e + \xi \mathcal{K} \frac{\partial m_d}{\partial t}. \quad (3.30)$$

The behavior of equations (3.29) and (3.30) can be demonstrated by considering an initial step increase in porosity with depth, and no dehydration. To avoid numerical issues, the step is smoothed slightly (e.g. *Spiegelman*, 1993b), so that

$$\phi(z, 0) = \begin{cases} 1, & z < z_0, \\ \phi_1 + (1 - \phi_1) \operatorname{sech}[(z - z_0)/2.5], & z \geq z_0, \end{cases} \quad (3.31)$$

where ϕ_1 is the magnitude of the porosity step at depth z_0 . Viscous resistance to porosity changes causes the initial step to propagate as a dispersive wavetrain (Figure 3.7); if viscous resistance were negligible then the porosity step would propagate as a perfect shock (*Spiegelman*, 1993b). Initially the flux below the porosity step is larger than above; this creates a local porosity maximum at the location of the step. However, as it continues to grow, the porosity maximum creates a region behind itself where locally the flux increases in the direction of flow, draining the region and

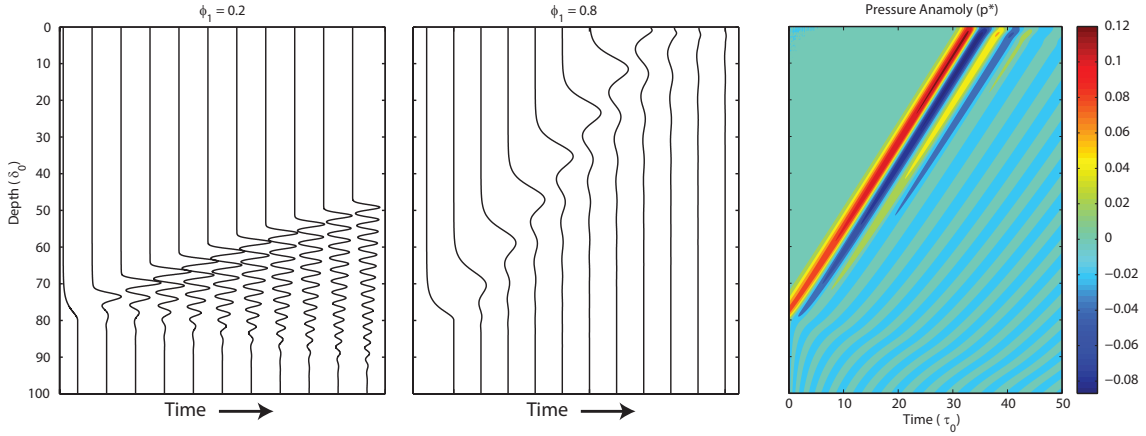


FIGURE 3.7. Evolution of a porosity step at $z = 80$ for (a) $\phi_1 = 0.2$ and (b) $\phi_1 = 0.8$. Viscous resistance to volume changes causes the initial step to propagate as a dispersive train of solitary waves. Panels (a) and (b) show porosity profiles with increasing time. The separation between adjacent profiles corresponds to a porosity of 1.5 (a) and 0.2 (b). (c) Contours of the pressure anomaly $z - p_{\text{tot}}$ for $\phi_1 = 0.8$, for comparison with Figure 3.10.

producing a porosity minimum. By the same process in reverse, the new minimum creates another porosity maximum behind itself and so on, and a wavetrain is formed.

Two examples are shown in Figure (3.7) for $\phi_1 = 0.2, 0.8$ (i.e. perturbations that are 20 and 80% of the initial porosity ϕ_0). In the case $\phi_1 = 0.2$ the wavetrain grows at a rate faster than the velocity of the leading wave and so information is propagated deeper into the column. Figure (3.7) also shows that the amplitude and speed of the waves depend on the initial porosity step ϕ_1 . For comparison, contours of the pressure anomaly $p^* = z - p_{\text{tot}}$ are shown in Figure 3.7c.

The physical mechanisms can be further illuminated by considering a simple example; the proceeding arguments follow those of *Spiegelman* (1993b). If initially there is a perfect step increase in porosity with depth (Figure 3.8), with boundary conditions $p_e(-\infty) = p_e(\infty) = 0$, and no dehydration, equation (3.29) at $t = 0$ takes

the form

$$-\frac{\partial^2 p_e}{\partial z^2} + p_e = 0, \quad z > 0, \quad (3.32)$$

$$-\phi^{n-1} \frac{\partial^2 p_e}{\partial z^2} + p_e = 0, \quad z < 0,$$

where the dimensionless effective pressure is $p_e = z - p$. Applying the boundary conditions along with the requirements that p_e and the fluid flux $q = \phi^n(1 - \partial p_e / \partial z)$ are continuous at $z = 0$ results in the solutions

$$p_e = p_e^{\max} e^z, \quad z > 0, \quad (3.33)$$

$$p_e = p_e^{\max} e^{-z\phi^{\frac{1-n}{2}}}, \quad z < 0,$$

where

$$p_e^{\max} = \frac{\phi^n - 1}{1 + \phi_1^{\frac{n+1}{2}}}.$$

Profiles at $t = 0$ for the effective pressure, porosity, $\partial\phi/\partial t$, and the fluid flux are shown in Figure 3.8a, for $\phi_1 = 0.5$. The pressure anomaly is largest at the porosity step and decays exponentially with distance from $z = 0$. Additionally, the fluid flux varies smoothly even though the porosity is discontinuous. From equation (3.30) we can see that the porosity will evolve from this initial condition by increasing at the location of the step; initially growing faster directly below the step than above, since the change in porosity is proportional to itself. As the porosity at the step increases, it will eventually produce a porosity minimum below itself as described above.

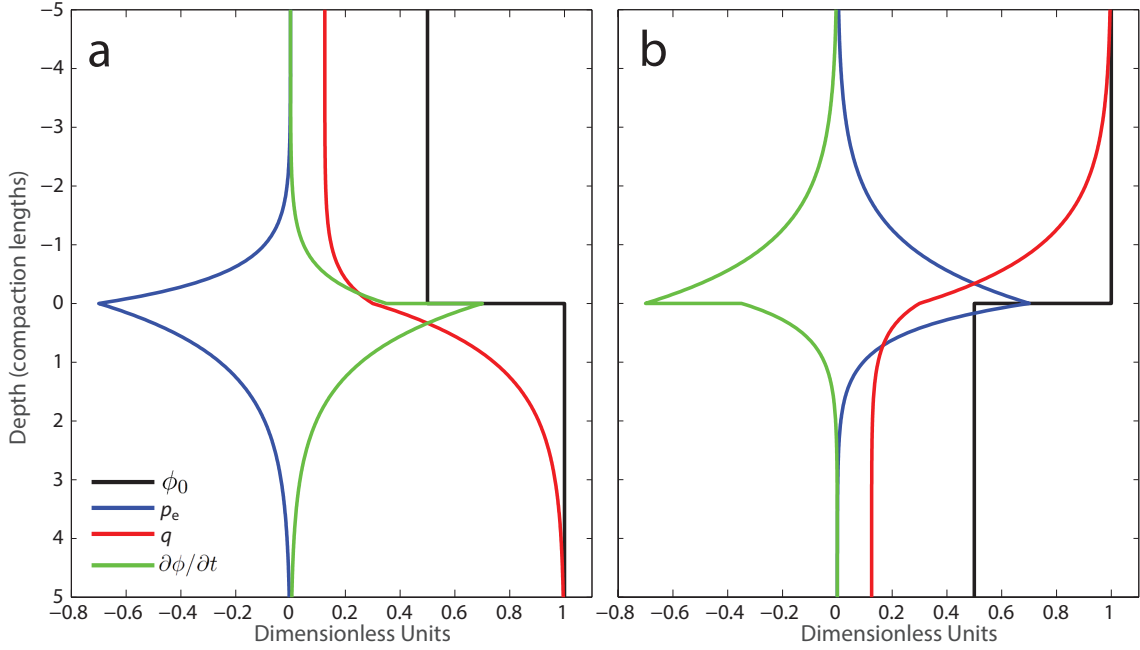


FIGURE 3.8. Initial profiles of effective pressure p_e (blues lines), fluid flux q (red lines), and $\partial\phi/\partial t$ (green lines), for the initial porosity profiles shown by the black lines.

If the procedure is reversed, so that the initial condition is a step decrease in porosity with depth, the result is that porosity will initially decrease in the vicinity of the step (Figure 3.8b). Again, this process will eventually create a porosity maximum below the minimum that develops at the step. This simple analysis illustrates further how viscous resistance to porosity changes produces the wavetrains shown in Figure (3.7) by alternately enhancing and obstructing fluid flow up the column.

3.4.2.1. Solitary Wave Behavior

The waves shown in Figure (3.7) behave as solitary waves whose properties can be described quite well through a physical analogy with a propagating step shock in porosity. The wave behavior produced by equations (3.29) and (3.30) is similar to that produced by equations for two-phase flow of melt within the solid Earth (*Richter and*

McKenzie, 1986; *Barcilon and Richter*, 1986; *Scott and Stevenson*, 1986; *Spiegelman*, 1993a,b). In these studies both the melt and solid matrix are treated as immiscible, incompressible and highly viscous fluids. For comparison, the equations derived by *McKenzie* (1984) in the absence of melting take the form

$$0 = \frac{\partial \phi}{\partial t} + \nabla \cdot (\phi \mathbf{v}) , \quad (3.34)$$

$$0 = \frac{\partial 1 - \phi}{\partial t} + \nabla \cdot [(1 - \phi) \mathbf{V}] , \quad (3.35)$$

$$\phi(\mathbf{v} - \mathbf{V}) = -\frac{k}{\mu} \nabla p , \quad (3.36)$$

$$\nabla p = \eta \nabla^2 \mathbf{V} + \left(\zeta + \frac{\eta}{3} \right) \nabla (\nabla \cdot \mathbf{V}) - g(1 - \phi) \Delta \rho \delta_{i3} , \quad (3.37)$$

$$k = k_0 \phi^n , \quad (3.38)$$

where \mathbf{v} and \mathbf{V} are the velocities of the melt and matrix, and ζ is the matrix bulk viscosity. Results from study of these equations are adapted here to analyze the wave behavior observed for equations (3.29) and (3.30).

The McKenzie equations will produce dispersive wavetrains very similar to those shown in Figure 3.7. Furthermore, in the small porosity limit with $n = 3$, the governing equations can be reduced to a single, nonlinear wave equation for porosity of the form (*Barcilon and Richter*, 1986)

$$\phi_t = [\phi^3(\phi_{zt} - 1)]_z . \quad (3.39)$$

Barcilon and Richter (1986) and *Spiegelman* (1993b) have shown that equation (3.39) admits solitary wave solutions with properties

$$c(A) = 2A + 1 , \quad (3.40)$$

$$\lambda(A, f) = - \left(A + \frac{1}{2} \right)^{\frac{1}{2}} \left\{ -2(A - f)^{\frac{1}{2}} + \frac{1}{(A - 1)^{\frac{1}{2}}} \ln \left[\frac{(A - 1)^{\frac{1}{2}} - (A - f)^{\frac{1}{2}}}{(A - 1)^{\frac{1}{2}} + (A - f)^{\frac{1}{2}}} \right] \right\} , \quad (3.41)$$

$$V(A, f) = \frac{2}{3} [2(2A + 1)(A - f)]^{\frac{1}{2}} [2A + f] , \quad (3.42)$$

where A is the maximum amplitude, c is the phase velocity, λ is the wavelength, and V is the volume contained within the solitary wave. Equations (3.40) – (3.42) are scaled to the small background porosity (*Barcilon and Richter*, 1986; *Spiegelman*, 1993b). In other words, $f = 1$ corresponds to $\phi = \phi_1$ for the scaling used in the analysis and numerical experiments presented here. For example, the re-scaled dispersion relation is (e.g. *Spiegelman*, 1993b) $c = \phi_1(2A + \phi_1)$, which can be seen from the scaling relations (3.21) – (3.23).

A physical argument developed by *Spiegelman* (1993b) and based on conservation of mass shows that the waves produced by the McKenzie equations are described very well by equations (3.40) – (3.42). First, assume that the leading wave in the train that develops from an initial step increase in porosity moves with the same mass as if the step propagated as a shock. For the initial porosity profile shown in Figure 3.8, the characteristic solution predicts a breaking porosity wave at time $t = \Delta t$ (*Whitham*, 2011; *Spiegelman*, 1993b). This is not a physical situation, as the porosity cannot be multi-valued at any particular location. However, the properties of the waves that are predicted by equations (3.29) and (3.30), can be described by finding the solitary wave that moves with the same mass as the hypothetical breaking wave. The porosity

(i.e. volume or mass in 1-D) in the breaking wave at time $t = \Delta t$ is

$$V_b = (1 - \phi_1^n) \Delta t . \quad (3.43)$$

Following *Spiegelman* (1993b), a reasonable estimate for Δt for the solitary wave is the time it takes the wave to move its wavelength λ , or $\Delta t = \lambda/c$. Thus, if the volume V in the solitary wave is equal to that of the breaking wave, then

$$V(A, \phi_1, n) = \frac{(1 - \phi_1^n) \lambda(A, \phi_1, n)}{c(A, \phi_1, n)} . \quad (3.44)$$

Equation (3.44) defines a relationship between the magnitude of the initial porosity step and the amplitude of solitary waves that subsequently develop. The relationship is compared in Figure 3.9 to the results shown in Figure 3.7 along with numerical simulations for $\phi_1 = 0.4, 0.6$. To be consistent, the analytical relations are re-scaled to the magnitude of the porosity step ϕ_1 (e.g. *Spiegelman*, 1993b). Figure 3.9a shows that the amplitude of the solitary waves is predicted quite well. However, Figure 3.9b shows that the dispersion relation (3.40), over predicts the velocity of the simulated waves. The disagreement is not extreme, and suggests that an accurate dispersion relation can be derived from the actual governing equations (rather than from the McKenzie equations).

Accordingly, in the absence of dehydration the pressure (3.29) and porosity (3.30) equations may be combined to form a single equation for porosity. First, combining the two equations and rewriting in terms of the effective pressure p_e we have

$$\phi_t = [\phi^n (1 - p_{e_z})]_z . \quad (3.45)$$

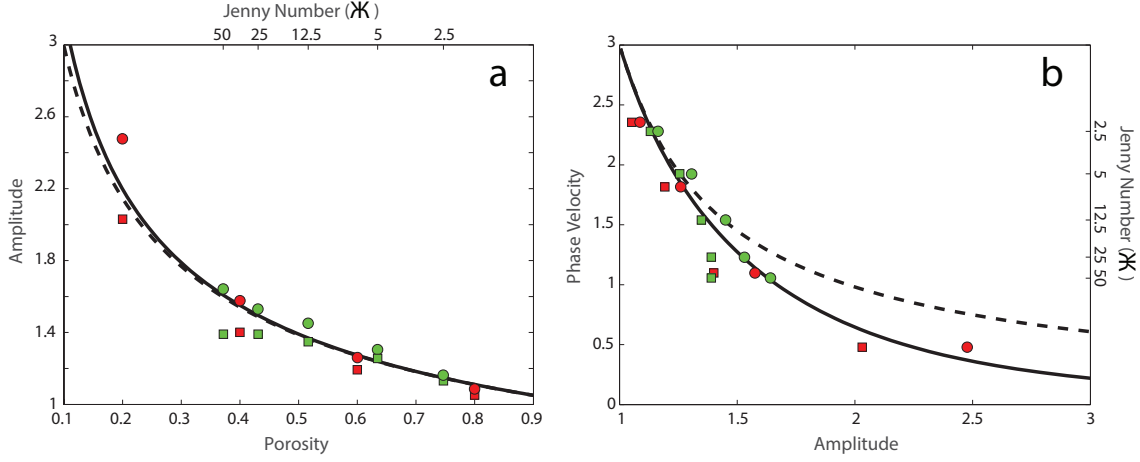


FIGURE 3.9. (a) Amplitude of dispersive wavetrains as a function of the porosity step ϕ_1 . Circles and squares show the maximum and mean amplitudes, respectively, of the leading porosity wave. The dashed line is the amplitude predicted by the physical argument relating to the McKenzie equations, the solid line is the same predicted for the system considered here (equation (3.47)). (b) Phase velocity of the leading porosity wave as a function of the amplitudes shown in panel (a). The dashed line corresponds to the dispersion relation given by equation (3.40), the solid line shows the prediction of the dispersion relation given by equation (3.54), both appropriately re-scaled. Green circles and squares show the maximum and mean amplitude of the leading wave for simulations that include dehydration.

The effective pressure gradient can be written in terms of the porosity by taking the gradient of equation (3.30)

$$\phi_{tz} = -\phi_z p_e - \phi p_{e_z} = \frac{\phi_z \phi_t}{\phi} - \phi p_{e_z}. \quad (3.46)$$

And finally, for $n = 3$ we obtain

$$\phi_t = \left[\phi^3 \left(1 + \frac{\phi_{tz}}{\phi} - \frac{\phi_z \phi_t}{\phi^2} \right) \right]_z. \quad (3.47)$$

Equation (3.47) is a nonlinear wave equation for porosity and should be compared to equation (3.39). Following *Barcilon and Richter* (1986), we seek solutions of the

form

$$\phi(z, t) = f(z - ct) . \quad (3.48)$$

Equation (3.47) becomes

$$-cf' = \left[f^3 \left(1 - \frac{cf''}{f} + \frac{cf'^2}{f^2} \right) \right]' , \quad (3.49)$$

where primes denote differentiation with respect to $z - ct$. Integrating equation (3.49) and applying the boundary condition $f(\infty) = 1$ (i.e. the porosity tends to the background value far from the wave disturbance) gives

$$-cf = f^3 \left(1 - \frac{cf''}{f} + \frac{cf'^2}{f^2} \right) - (c + 1) . \quad (3.50)$$

Defining $p = f'$ gives

$$\begin{aligned} -cf &= f^3 \left(1 - \frac{cp}{f} \frac{dp}{df} + c \frac{p^2}{f^2} \right) - (c + 1) , \\ &= f^3 \left[1 - \frac{cf}{2} \frac{d}{df} \left(\frac{p^2}{f^2} \right) \right] - (c + 1) . \end{aligned} \quad (3.51)$$

where

$$\frac{d}{df} \left(\frac{p^2}{f^2} \right) = \frac{2}{f} \left(\frac{p}{f} \frac{dp}{df} - \frac{p^2}{f^2} \right) . \quad (3.52)$$

Integrating and applying the same boundary condition as before, along with $p(\infty) = 0$, gives

$$\frac{c}{2} \frac{p^2}{f^2} = \frac{1}{6f^3} [c(f - 1)^2(f + 2) + 2(1 - f^3) + 6f^3 \ln f] . \quad (3.53)$$

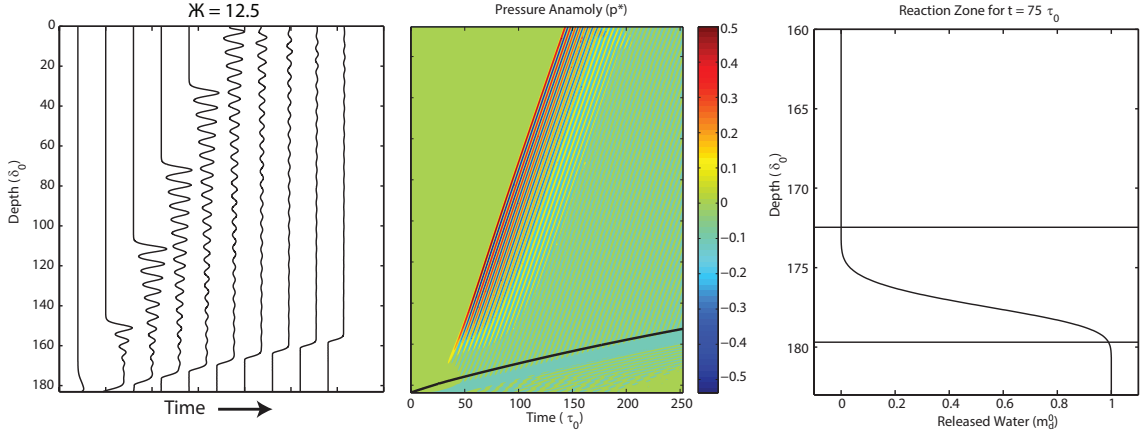


FIGURE 3.10. Evolution of initially uniform (a) porosity and (b) pressure anomaly for a simulation including dehydration with $\mathcal{K} = 12.5$. The separation between adjacent profiles in panel (a) corresponds to a normalized porosity of 1.3. (c) The amount of released water m_d within the reaction zone for time $t = 75t_o$. This corresponds to the third porosity profile in panel (a). The horizontal black lines show the numerically determined reaction zone, defined by the depth where $\Delta G = 0$ and the depth where $m_d = 0.99m_d^0$.

The dispersion relation is found by setting $p(A) = 0$, where A is the maximum porosity of the solitary wave (*Spiegelman, 1993b*). Then

$$c(A) = \frac{2(1 + 3A^3 \ln A - A^3)}{(A - 1)^2(A + 2)}. \quad (3.54)$$

This equation is re-scaled to ϕ_1 and plotted in Figure (3.9) and agrees quite well with the simulated phase velocities. Finally equation (3.54) is used along with equations (3.41) and (3.42) to determine a new relationship between A and ϕ_1 ; the result does not differ substantially from the one determined earlier.

3.4.2.2. Dehydration

The behavior of the model does not differ substantially if dehydration is included as described in Section 2. The solitary waves that form are identical to those formed by an initial porosity step without dehydration. Figure 3.9 includes results from a

variety of simulations that include dehydration. In all of these simulations the initial porosity profile is uniform and the magnitude of the porosity increase due to the reaction is controlled by the value of the Jenny number \mathcal{JK} and the kinetics of the reaction; otherwise the simulations are identical.

Figure 3.9 also shows that the results of simulations including dehydration begin to deviate from the predicted behavior as the value of \mathcal{JK} increases. This is due to numerical error caused by employing a constant grid spacing. No reliable results could be obtained for $\mathcal{JK} > 50$. More sophisticated numerical routines that employ a dynamic grid spacing should be able to produce reliable results over a larger parameter range (e.g. *Connolly, 1997*).

The most important effect of the dehydration reaction is to increase the porosity at the reaction front. An example with $\mathcal{JK} = 12.5$ is shown in Figure 3.10. As the reaction front propagates up the column, the region of increased porosity that it leaves behind will eventually become sufficiently large to initiate a solitary wavetrain that separates from the reaction front and propagates up the column. As the wavetrain travels up the column, it leaves behind it a region of elevated porosity similar in magnitude to the region of elevated porosity created by the reaction front before the wavetrain initiated (Figure 3.10a). As the reaction front moves into this region of elevated porosity it is no longer able to generate sufficiently large porosities to initiate another solitary wavetrain.

In these simulations, the reaction boundary moves steadily up the column at a velocity v_r controlled by the rate of temperature increase due to conduction. Figure 3.10b shows contours of the pressure anomaly, as well as the upper boundary of the reaction zone, defined by the depth where ΔG becomes negative. Because of this steady movement, the distribution of chemically released fluid within the reaction

zone increases exponentially with depth measured from the upper boundary of this zone, and does not change with time (Figure 3.10c).

Figure 3.10 also highlights the difficulty in producing a sustained, periodic pressure signal at the plate interface. In these simulations the dehydration zone propagates at a constant velocity that depends primarily on the rate of conductive temperature increase within the column. No other solitary wavetrains can form when this is the case. In order to generate multiple wavetrains, the movement of the reaction zone must be periodic. In other words, pressure and temperature changes within the reaction zone must be sufficient to push the material to the left of the reaction boundary in Figure 3.2, causing the reaction to stop until further temperature increase causes it to re-start.

3.4.2.3. Thickness of the Reaction Zone

The steady form of the chemically released fluid profile within the reacting material suggests a simple method for estimating the thickness of the reaction zone based on the kinetic and thermal parameters. If we change coordinates into a frame moving with the reaction zone $z' = z - v_r t$, the kinetic dehydration rate law becomes

$$-m_d^0 \left(\frac{\partial m'}{\partial t} - v_r \frac{\partial m'}{\partial z'} \right) = s M_{\text{H}_2\text{O}} m' A |\Delta G|^{n_r} c_0 \exp \left[-\frac{E_a}{R} \left(\frac{1}{T} - \frac{1}{T_0} \right) \right], \quad (3.55)$$

where $m' = 1 - m_d/m_d^0$. In this coordinate system $z' = 0$ corresponds to the top of the reaction zone, and increases with depth. Transformation to the moving frame also ensures that the dehydration rate does not change with time within the reaction zone, so the first term in equation (3.55) can be ignored.

The fact that the reaction rate is steady within the reaction zone suggests that the total pore pressure and temperature profiles within this region do not deviate much from the background values defined by the lithostatic pressure gradient and the geothermal gradient. The simulations show this is the case, and further suggest that both ΔG and the exponential term in equation (3.55) also change linearly with depth. First, note that

$$\frac{d}{dz} \left(\frac{1}{T} \right) = -\frac{1}{T^2} \nabla T_g ,$$

where ∇T_g is the background geothermal gradient. Then if the temperature increases linearly with depth according to ∇T_g , we can write

$$\frac{1}{T} = - \left(\frac{1}{T^2} \nabla T_g \right) z' + \frac{1}{T_{\text{top}}} , \quad (3.56)$$

where $1/T_{\text{top}}$ is the temperature at the top of the reaction zone at $z' = 0$. Since the quantity $1/T^2$ should not change much over the thickness of the reaction zone, we will approximate it as $1/T_{\text{top}}^2$. The quantity $E_a \nabla T_g z' / (RT^2)$ is much less than one, and we can approximate the temperature dependence in equation (3.55) as

$$\exp \left(-\frac{E_a}{RT} \right) \approx \exp \left(-\frac{E_a}{RT_{\text{top}}} \right) \left(1 + \frac{E_a \nabla T_g z'}{RT_{\text{top}}^2} \right) . \quad (3.57)$$

Second, since the Gibbs free energy is by definition zero at the top of the reaction zone and decreases with depth, we can write $\Delta G \approx -G_z z$. The gradient G_z must be estimated empirically from thermodynamic data and the background temperature and pressure fields. For the simulations considered here $G_z = 15$ cal/(m mol).

Finally, equation (3.55) can be approximated as (dropping primes on z)

$$v_r m_d^0 \frac{\partial m'}{\partial z} = Q m' z^{n_r} \left(\frac{E_a \nabla T_g}{RT_{\text{top}}^2} z + 1 \right), \quad (3.58)$$

where $Q = M_{\text{H}_2\text{O}} A |G_z|^{n_r} c_0 \exp \left[-\frac{E_a}{R} \left(\frac{1}{T_{\text{top}}} - \frac{1}{T_0} \right) \right]$. Integrating and requiring $m'(z = 0) = 1$ gives

$$m'(z) = \exp \left[\left(\frac{Q E_a \nabla T_g}{v_r m_d^0 (n_r + 2) R T_{\text{top}}^2} \right) z^{n_r+2} + \left(\frac{Q}{v_r m_d^0 (n_r + 1)} \right) z^{n_r+1} \right]. \quad (3.59)$$

Since v_r is negative (the reaction front moves vertically up the column), the second term in the exponential expression in equation (3.59) dominates and we are left with

$$m'(z) = \exp \left[\left(\frac{Q}{v_r m_d^0 (n_r + 1)} \right) z^{n_r+1} \right]. \quad (3.60)$$

Equation (3.60) shows that the chemically bound fluid content decays exponentially with depth from the top of the reaction boundary.

The total thickness Δz_r of the reaction zone can be estimated by finding the depth where 99% of the chemically bound fluid has been released, or $m'(\Delta z_r) = 0.01$. Putting this requirement into equation (3.60) gives

$$\Delta z_r = \left[\frac{\ln(0.01)(n_r + 1)v_r m_d^0}{M_{\text{H}_2\text{O}} A |G_z|^{n_r} c_0 \exp \left[-\frac{E_a}{R} \left(\frac{1}{T_{\text{top}}} - \frac{1}{T_0} \right) \right]} \right]^{\frac{1}{n_r+1}}. \quad (3.61)$$

For the simulation shown in Figure 3.10, the numerically determined reaction zone thickness is 40 m, while equation (3.61) predicts $\Delta z_r = 42$ m. It is important to note that the reaction zone thickness predicted by equation (3.61) does not make any assumptions about the rheological behavior of the dehydrating material, so this

result should apply to dehydration in the elastic regime as well. If kinetic parameters for the dehydration of basaltic oceanic crust have values similar to those used here for serpentinite, then it is reasonable to assume an ~ 40 m thick reaction zone in the subducting crust. If this is the case, then the time scale for dehydration of this amount of material in the elastic regime is $t^* \approx 20$ years for a permeability of 10^{-20} m², which is approaching times comparable to the recurrence interval for slow slip and tremor.

3.4.3. Summary

Our results support the notion that, if there is a significant viscous component to deformation in the slow slip zone then the presence of dehydration reactions can be expected to generate porosity waves within the plate interface subduction channel. It is possible, given likely values of viscosity and values of permeability near the upper limit of plausibility, that such waves trigger ETS events and may explain observed periodicity in subduction zones. Thermodynamic modeling conducted by *Peacock* (2009) showed that worldwide, subduction zone ETS occurs across a fairly wide range of pressure and temperature conditions, such that a single dehydration reaction cannot explain the range of observations. If this is true, our results imply that the range of ETS recurrence intervals observed at locations may be explained by the kinetics of the relevant dehydration reactions.

Any obstruction to fluid flow in a viscously deforming porous medium can be expected to generate porosity waves (*Spiegelman*, 1993c). Competent, elastically deforming blocks within a subduction channel are obvious candidates for producing such obstacles to fluid flow within a viscous matrix. Such a situation could possibly lead to the formation of high porosity, high permeability channels along the

boundaries of competent blocks. Similar features have been observed in models of melt migration at mid-oceanic ridges and beneath arc volcanoes, where high permeability channels may form due to the flow of melt against an impermeable freezing boundary (*Spiegelman, 1993c; Wilson et al., 2014*).

3.5. Discussion and Conclusion

The rheology and fluid pressure along the plate interface are of primary importance in understanding slow slip and tremor in subduction zones. We highlight two key observations relevant to this point. First, slow slip and tremor at subduction zones generally occur within the frictional transition zone. In other words, they occur over the range of pressures and temperatures where the material along the plate interface transitions from dominantly seismic deformation, to dominantly aseismic deformation. This seems to be the case at every subduction zone where slow slip or tremor has been observed. Second, wherever slow slip or tremor are observed, there is also strong evidence that the fluid pressures are close to lithostatic values. Furthermore, ETS has only been observed at depths where the only plausible sources of such pressure are chemical dehydration reactions.

We propose a very simple conceptual model that takes these observations into account. First, the plate interface in the slow slip zone is best described as a subduction channel shear zone. Furthermore, we imagine that the aseismic matrix within the subduction channel is to a large degree composed of hydrous minerals such as serpentinite. Second, fluid produced by progressive dehydration of basalt within the subducting crust, but beneath the subduction channel, is trapped by the subduction channel itself, which acts as a low-permeability seal (e.g. *Audet et al., 2010*). If the subduction channel contains large amounts of highly sheared viscous materials like

serpentinite, this would explain the low permeability, at least perpendicular to the sense of shear (*Kawano et al.*, 2011; *Okazaki et al.*, 2013). On top of this, the material within the subduction channel is itself dehydrating, perhaps episodically, against a background of nearly lithostatic fluid pressure. The dehydration of serpentinite has been experimentally observed to transiently generate a 1 to 3 order magnitude increase in permeability (*Tenthorey and Cox*, 2003). This increase in permeability may allow rapid migration of fluid, initiating an ETS event, before continued shear decreases permeability again, and the cycle begins once more.

Once an ETS event begins, its characteristics should be governed by the frictional properties of the subduction channel. Models of slow slip that incorporate rate and state friction generally require some stabilizing mechanism to prevent slip events from growing into large earthquakes. The subduction channel concept corresponds to models that successfully stabilize slow slip by incorporating mixed velocity–weakening (seismic) and velocity–strengthening (aseismic) frictional properties, or a similar mixture of brittle and ductile materials, along the plate interface (e.g. *Regenauer-Lieb and Yuen*, 2008; *Ando et al.*, 2010; *Daub et al.*, 2011; *Nakata et al.*, 2011; *Skarbek et al.*, 2012). Deformation experiments on lizardite and antigorite serpentinite specimens show that deformation in the brittle regime is nondilatant, even in specimens that are serpentinitized to a low ($\sim 10\text{--}15\%$) degree (*Escartín et al.*, 1997, 2001). Thus, if serpentinite is present in the plate interface, it may preclude models that invoke dilatant strengthening to stabilize slow slip (e.g. *Liu and Rubin*, 2010; *Segall et al.*, 2010), at least at depths close to the mantle wedge corner where the subduction channel is likely serpentinitized.

This conceptual model has a few implications. First, it implies that fluid pressures within the slow slip zone are always high. This conclusion is supported the

results of our elastic model, and more generally by all of the evidence for large fluid pressures outlined above. There are no reported observations of large fluid pressure variations associated with ETS, so any variations in fluid pressure must be some small fraction of the total. Additionally, models that invoke diffusive transport of fluid pressure on timescales comparable to ETS recurrence intervals require somewhat unreasonable permeabilities. Localized increases in fluid pressure may trigger ETS events, but it seems unlikely that the propagation of an event is mediated by continued fluid flow (*Peng and Gombert, 2010*).

Given expected values of subduction channel viscosity and values of permeability on the high end of plausibility, it is possible that viscous transport of reaction generated porosity can trigger an ETS event. Although we did not explicitly include the effects of shearing a subduction channel, or of imposed physical obstacles to flow such as might be caused by competent blocks in a viscous matrix, our model represents a first-order description of such a system, and our results give a good indication that viscous effects are important in governing the behavior of slow slip and tremor in subduction zones. Future research will focus on how porosity waves travel through a subduction channel and interact with obstacle forming, competent material.

3.6. Model Derivation

Here we derive the governing equations for compaction of a fluid saturated porous medium. Viscous deformation is incorporated by including *a priori* a compaction term that depends linearly on the shear viscosity. Dehydration related fluid sources are included by suitably altering the statement of conservation of fluid mass.

3.6.1. Pore Pressure and Porosity

The stress-strain relations for a fluid saturated, linear elastic, porous medium are

$$\sigma_{ij} = 2G\varepsilon_{ij} + \left(K - \frac{2G}{3}\right)\varepsilon_{kk}\delta_{ij} - \alpha p\delta_{ij}, \quad (3.62)$$

where σ_{ij} and ε_{ij} are the components of the stress and strain tensors, p is the total pore pressure and the Einstein summation convention is used. Additionally, conservation of fluid mass within the porous solid demands

$$\frac{\partial m_f}{\partial t} + \rho_f \frac{\partial q_i}{\partial x_i} = \frac{\partial m_d}{\partial t}, \quad (3.63)$$

where m_f is the fluid mass density relative to that which would occupy a reference volume of the porous medium in an unstressed and unpressurized reference state, q_i is the discharge velocity of the fluid relative to the solid, ρ_f is the fluid density, and m_d is the mass density of chemically released fluid.

For an infinitesimal deformation of the elastic volume we can write the change in the isothermal free energy per unit volume as

$$dW = \sigma_{ij}d\varepsilon_{ij} - \phi dp, \quad (3.64)$$

which is an exact differential (*Rice and Cleary, 1976*). Making use of the Maxwell relations

$$\sigma_{ij} = \left(\frac{\partial W}{\partial \varepsilon_{ij}}\right)_p, \quad \phi = -\left(\frac{\partial W}{\partial p}\right)_{\varepsilon_{ij}},$$

we can write

$$\left(\frac{\partial\sigma_{ij}}{\partial p}\right)_{\varepsilon_{ij}} = \frac{\partial^2 W}{\partial\varepsilon_{ij}\partial p} = -\left(\frac{\partial\phi}{\partial\varepsilon_{ij}}\right)_p = -\frac{1}{\rho_f}\left(\frac{\partial m_f}{\partial\varepsilon_{ij}}\right)_p. \quad (3.65)$$

From equation (3.62) we have

$$\left(\frac{\partial\sigma_{ij}}{\partial p}\right)_{\varepsilon_{ij}} = -\alpha\delta_{ij}, \quad (3.66)$$

so that

$$\left(\frac{\partial m_f}{\partial\varepsilon_{ij}}\right)_p = \rho_f\alpha\delta_{ij}. \quad (3.67)$$

Integrating and assuming a linear dependence on pressure, we have

$$dm_f = \rho_f\alpha\varepsilon_{kk} + C_1p. \quad (3.68)$$

where C_1 is some constant.

A brief calculation of the pressure change due to an undrained elastic deformation (i.e. $dm_f = 0$) will determine C_1 . Consider the superposition of two states: 1) an isotropic stress $P - p$ applied at zero pore pressure and 2) an isotropic stress p applied at pore pressure P . The volumetric strains ε_{kk} in these two states are (p. 281 *Malvern*, 1977)

$$\varepsilon_{kk}^1 = -\frac{P - p}{K}, \quad \varepsilon_{kk}^2 = -\frac{p}{K_s}, \quad (3.69)$$

so that the volumetric strain in the superimposed state is

$$\varepsilon_{kk} = -\left(\frac{P - p}{K} + \frac{p}{K_s}\right) = -\frac{P - \alpha p}{K}. \quad (3.70)$$

Now the pressure due to the undrained deformation can be written as

$$p = \frac{P + \varepsilon_{kk}K}{\alpha} = -\frac{(K_u - K)\varepsilon_{kk}}{\alpha}, \quad (3.71)$$

where K_u is the undrained bulk modulus defined by $K_u = -p/\varepsilon_{kk}$. Then setting equation (3.68) equal to zero and using equation (3.71) we have

$$\rho_f \alpha \varepsilon_{kk} + C_1 \frac{(K - K_u)\varepsilon_{kk}}{\alpha} = 0, \quad (3.72)$$

or

$$C_1 = \frac{\rho_f \alpha^2}{K_u - K}. \quad (3.73)$$

Thus for small strains and pressures relative to the reference state, the change in fluid content due to elastic deformation can be expressed as

$$dm_f = \rho_f \alpha \varepsilon_{kk} + \frac{\rho_f \alpha^2}{K_u - K} p. \quad (3.74)$$

At this point we require that inelastic changes in porosity will also cause a change in fluid content so that

$$dm_f = \rho_f \alpha \varepsilon_{kk} + \frac{\rho_f \alpha^2}{K_u - K} p + \rho_f d\phi^{\text{in}}. \quad (3.75)$$

We now want to develop an equation for the change in porosity. From the definition of m_f we can write

$$dm_f = \phi d\rho_f + \rho_f d\phi = \frac{\rho_f}{K_f} \phi p + \rho_f d\phi, \quad (3.76)$$

where K_f is the fluid bulk modulus defined by $K_f = \rho_f dp/d\rho_f$. Then from equation (3.75) we have

$$d\phi = \alpha\varepsilon_{kk} + \left(\frac{\alpha^2}{K_u - K} - \frac{\phi}{K_f} \right) p + d\phi^{\text{in}} . \quad (3.77)$$

At this point σ_{ij} and p are redefined to describe perturbations from an initial hydrostatic state, σ_{ij}^{hyd} and p^{hyd} , in equilibrium with gravitational loading (*Rice and Cleary, 1976*). Then this initial state satisfies

$$\frac{\partial \sigma_{ij}^{\text{hyd}}}{\partial x_i} - g\rho \frac{\partial z_{\text{elev}}}{\partial x_j} = 0 , \quad (3.78)$$

$$\frac{\partial p^{\text{hyd}}}{\partial x_i} + g\rho_f \frac{\partial z_{\text{elev}}}{\partial x_i} = 0 , \quad (3.79)$$

where z_{elev} is the vertical elevation above some datum. Considering σ_{ij} and p as perturbations away from the initial hydrostatic state, stress equilibrium requires

$$\frac{\partial \sigma_{ij}}{\partial x_i} = 0 . \quad (3.80)$$

Now restricting the problem to uniaxial strain in the x_1 direction, ε_{11} is the only non-zero strain component. In this situation the only non-zero stresses are σ_{11} , σ_{22} , and σ_{33} , which are related through the stress-strain relations such that

$$\sigma_{11} = \left(K + \frac{4G}{3} \right) \varepsilon_{11} - \alpha p , \quad (3.81)$$

$$\sigma_{22} = \sigma_{33} = \left(K - \frac{2G}{3} \right) \varepsilon_{11} - \alpha p . \quad (3.82)$$

Substituting equations (3.75) and (3.81) into the statement of conservation of fluid mass yields

$$\frac{\partial p}{\partial t} = \frac{c_m}{\mu} \frac{\partial}{\partial z} \left[k(\phi) \frac{\partial p}{\partial z} \right] - c_m \frac{\partial \phi^{\text{in}}}{\partial t} + \frac{c_m}{\rho_f} \frac{\partial m_d}{\partial t} + \gamma \dot{\sigma}_{11} , \quad (3.83)$$

where Darcy's law has also been used

$$q_1 = -\frac{k}{\mu} \frac{\partial p}{\partial x_1} , \quad (3.84)$$

and where

$$c_m = \frac{(K_u - K)(K + \frac{4G}{3})}{\alpha^2(K_u + \frac{4G}{3})} , \quad \gamma = \frac{K_u - K}{\alpha(K_u + \frac{4G}{3})} .$$

Substituting equation (3.75) into equation (3.77) yields

$$\frac{\partial \phi}{\partial t} = \left(\frac{1}{c_m} - \frac{\phi}{K_f} \right) \frac{\partial p}{\partial t} + \frac{\partial \phi^{\text{in}}}{\partial t} - \frac{\gamma}{c_n} \dot{\sigma}_{11} . \quad (3.85)$$

Throughout this study, we assume that the permeability obeys the relationship

$$k = k_0 \left(\frac{\phi}{\phi_0} \right)^n . \quad (3.86)$$

Finally, the inelastic change in porosity is given by

$$\frac{\partial \phi^{\text{in}}}{\partial t} = \frac{\xi}{\rho_f} \frac{\partial m_d}{\partial t} - \frac{3}{4\eta} p_e \dot{\phi} , \quad (3.87)$$

where ξ is an empirical parameter governing porosity production due to reaction driven loss in solid mass, $p_e = g\Delta\rho z - p$ is the effective pressure, and η is shear viscosity. The last term in equation (3.87) describes changes in porosity due to the assumed linear viscous behavior.

3.6.2. Temperature

3.6.2.1. First Law

Consider the local thermodynamic properties of a linear elastic, porous medium plus a mobile fluid in the reference state (T^0, p^0) :

e = internal energy per unit reference volume of the composite system

s = entropy per unit reference volume of the composite system

s_s = entropy of the solid component per unit mass of solid

m_s = mass of solid per unit reference volume of the composite system

T = local temperature

Consider also the thermodynamic properties of a fluid phase in an imagined external reservoir at local thermal and compositional equilibrium with the composite system:

$e_f = e_f(p, T)$ = internal energy of the fluid per unit mass of fluid

$s_f = s_f(p, T)$ = entropy of the fluid per unit mass of fluid

Now consider a system consisting of a unit reference volume of the composite system plus some fluid mass dm_f from the equilibrating reservoir, which is reversibly added to the composite system. The work done on the system in pushing in the fluid is $p(dm_f/\rho_f)$, where dm_f/ρ_f is the volume of fluid pushed in. The work done by deforming the composite system is $-\sigma_{ij}d\epsilon_{ij}$. As noted above, we are assuming that dehydration reactions do no work on the overall system.

As a result of adding the fluid and deforming the composite system, the energy of the overall system changes from $e + e_f dm_f$ before fluid insertion to $e + de$ after fluid insertion. Additionally, the entropy of the overall system changes from $s + s_f dm_f$ to $s + (s_f - s_s)dm_s + ds$, where dehydration reactions have changed the solid mass by $-dm_s$. The heat absorbed is T times the change in entropy. Thus the first law of thermodynamics requires

$$de - e_f dm_f = T[(s_f - s_s)dm_s + ds - s_f dm_f] + \frac{p}{\rho_f} dm_f - \sigma_{ij} d\epsilon_{ij} , \quad (3.88)$$

or

$$de - e_f dm_f = T(ds - s_f dm_f) + \frac{p}{\rho_f} dm_f + L dm_s - \sigma_{ij} d\epsilon_{ij} , \quad (3.89)$$

where $L = T(s_f - s_s)$ is the latent heat of the dehydration reaction.

Finally, consider a general non-equilibrium process of fluid motion and elastic deformation in the porous medium, but assume that the succession of states can be considered as a sequence of local equilibrium states such that the above statement of the first law remains valid. Then, considering an arbitrary region of space V with bounding surface S , the first law can be written as

$$\begin{aligned} \frac{\partial}{\partial t} \int_V e dV + \int_S e_f (\rho_f q_i) \cdot dS = & - \int_S Q \cdot dS - \int_S \frac{p}{\rho_f} (\rho_f q_i) \cdot dS + \frac{\partial}{\partial t} \int_V L m_s dV \\ & - \int_V \sigma_{ij} \frac{\partial \epsilon_{ij}}{\partial t} dV - \int_V g (\rho_f q_i) \frac{\partial z_{\text{elev}}}{\partial x_i} dV , \end{aligned} \quad (3.90)$$

where Q is the heat flux out of the volume V and the last term on the RHS accounts for the body force due to gravity on the system. Then using the divergence theorem and the statement of fluid mass conservation, application to a region V of arbitrarily

small size yields

$$\frac{\partial e}{\partial t} + \nabla \cdot [e_f(\rho_f q_i)] = -\nabla \cdot Q - \nabla \cdot (p q_i) - L \frac{\partial m_d}{\partial t} - \sigma_{ij} \frac{\partial \epsilon_{ij}}{\partial t} - g(\rho_f q_i) \cdot \nabla z_{\text{elev}} . \quad (3.91)$$

To put equation (3.91) into the form of a PDE for temperature, note that $de = C_s dT$, $\rho_f de_f = C_f dT$, and $Q = -K_T \nabla T$, where C_s and C_f are the specific heat of the solid and fluid phases, and K_T is the thermal conductivity. Putting all of this together along with Darcy's law, we arrive at

$$C_s \frac{\partial T}{\partial t} = K_T \nabla^2 T + C_f \nabla \cdot \left(\frac{k}{\mu} T \nabla p \right) + \nabla \cdot \left(\frac{k}{\mu} p \nabla p \right) - L \frac{\partial m_d}{\partial t} - \sigma_{ij} \dot{\epsilon}_{ij} + \frac{g \rho_f k}{\mu} \nabla p \cdot \nabla z_{\text{elev}} . \quad (3.92)$$

This equation states that the change in temperature is due to conduction (first term on RHS), advective transport and work due to fluid flow (second and third terms), the latent heat of the dehydration reaction (fourth term), work done by elastic deformations (fifth term), and changes in gravitational potential energy (last term).

3.6.2.2. Second Law

The second law of thermodynamics places some constraints on the behavior of the dehydration reaction. In the form of the Calusius-Duheim inequality applied to the overall system, the second law requires

$$\frac{\partial}{\partial t} \int_V s dV + \int_S s_f(\rho_f q_i) \cdot dS \geq - \int_S \frac{Q}{T} \cdot dS , \quad (3.93)$$

with the local form

$$\frac{\partial s}{\partial t} - s_f \left(\frac{\partial m_f}{\partial t} - \frac{\partial m_d}{\partial t} \right) + (\rho_f q_i) \cdot \nabla s_f \geq -\frac{\nabla \cdot Q}{T} + \left(\frac{Q}{T^2} \right) \cdot \nabla T. \quad (3.94)$$

Multiplying (30) by $-T$ and adding the result to (3.94) yields

$$\begin{aligned} \frac{\partial e}{\partial t} - T \frac{\partial s}{\partial t} + \sigma_{ij} \frac{\partial \epsilon_{ij}}{\partial t} + \left(T s_f - e_f - \frac{p}{\rho_f} \right) + L \frac{\partial m_d}{\partial t} \leq - \left(e_f - T s_f + \frac{p}{\rho_f} \right) \frac{\partial m_d}{\partial t} \\ - (\rho_f q_i) \cdot \left\{ g \nabla z_{\text{elev}} + \left[\nabla e_f - T \nabla s_f + \nabla \left(\frac{p}{\rho_f} \right) \right] \right\} - \frac{Q}{T} \cdot \nabla T. \end{aligned} \quad (3.95)$$

The LHS of equation (3.95) is zero, which can be seen from (3.89). Additionally, from the definition of the chemical potential $\mu_f = e_f - T s_f + p/\rho_f$ of a pure fluid phase we have $\nabla e_f - T \nabla s_f + \nabla(p/\rho_f) = \nabla p/\rho_f$, so

$$(\rho_f q_i) \cdot \left[\frac{\nabla p}{\rho_f} + g \nabla z_{\text{elev}} \right] + \frac{Q}{T} \cdot \nabla T \leq - (L + \mu_f) \frac{\partial m_d}{\partial t}, \quad (3.96)$$

which is a thermodynamic constraint on the diffusion of fluid and the flow of heat in the presence of a dehydration reaction.

3.7. Bridge

In this chapter I developed a poro-elastic model to examine how fluid pressure in the slow slip zone is generated through chemical dehydration reactions. Results indicated that the dehydration of subducting oceanic basalt in the elastic regime is likely responsible for the presence of lithostatic fluid pressure at the plate interface. On top of this, viscous dehydration of serpentinite within the subduction channel has important implications for the movement of fluid pressure at the plate interface,

and may be responsible for triggering slow slip and tremor at observed recurrence intervals.

Now for something completely different. In Chapter IV, I focus on shallow slow slip. Recent observations in Japan have documented the occurrence of tremor and slow slip in subduction zone accretionary prisms and along the plate interface at depths <10 km, above the seismogenically locked zone (*Ito and Obara, 2006a,b; Ando et al., 2012; Sugioka et al., 2012*). As with the occurrence of ETS at depths below the locked zone, this shallow behavior has been associated with high fluid pressures and mechanical heterogeneity (*Kitajima and Saffer, 2012; Sugioka et al., 2012; Saito et al., 2013*). Chapter IV is devoted to understanding the mechanics of accretionary prisms. The stress state and properties of accretionary prisms define the background against which shallow tremor and slow slip take place, and so are of primary importance to understanding ETS behavior overall.

CHAPTER IV

HETEROGENEOUS COULOMB WEDGES: INFLUENCE OF PORE PRESSURE, POROSITY, AND INTERNAL FRICTION

This chapter presents unpublished material that I developed with Alan Rempel. I performed all of the calculations; Alan provided scientific and philosophical guidance.

4.1. Introduction

Coulomb wedge models are simple but effective tools used to study accretionary prisms and thin-skinned fold-and-thrust belts (*Dahlen, 1990*). These models describe a relationship at mechanical equilibrium between the geometry and the internal properties of a wedge shaped body. Their widespread application has yielded important insights into the mechanics of accretionary systems and associated faults (e.g. *Davis et al., 1984; Zhao et al., 1986; Dahlen, 1990; Breen and Orange, 1992; Lallemand et al., 1994; Wang and Hu, 2006*). Recent data acquisition enables spatially resolved estimates of controlling wedge parameters in active submarine margins, thereby providing vastly improved constraints that motivate more detailed theoretical investigations of such systems. Here we focus on models of submarine accretionary wedges, and investigate how internal heterogeneity affects calculations of basal shear stress, taper angle, and internal slip surface geometry (i.e. faults that step-up from the basal surface).

A major simplification employed in most Coulomb wedge models (hereafter referred to simply as “wedge models”) involves assigning representative, depth-averaged values for the internal properties of the wedge. However, to fully characterize the mechanical constraints on wedge behavior, the spatial distributions of pore

pressure, porosity, and coefficient of friction are required throughout the wedge volume. Acquiring detailed information on these parameters represents a significant challenge for any given site. Lacking adequate constraints, the role of heterogeneity in wedge models has not received much attention (see *Fletcher, 1989; Zhao et al., 1986; Dahlen, 1990; Breen and Orange, 1992*). Instead, it has been common practice to assume depth-averaged values for internal properties (see *Lallemand et al., 1994; Wang and Hu, 2006*). However, as ever more data is collected at various sites, the need for mechanical models that include the effects of heterogeneous internal properties has become acute.

Given that the surface profile of any wedge should generally be known and available as a model input, two types of problems are commonly addressed. Many previous studies have focused on explaining the observed taper angles of accretionary prisms (e.g. *Wang and Hu, 2006*), based on assumptions about the internal state of the wedge and the shear stress along its base. Conversely, the geometry of the wedge can be used to gain information about the internal state, or the basal shear stress (e.g. *Suppe, 2007*); this second approach is particularly useful since the basal dip can usually (but not always) be determined using seismic data (e.g. *Moore et al., 2009; Smith et al., 2012*). Here, we derive a model that incorporates spatial heterogeneity and investigate the implications for both types of wedge problems. To this end, we make use of the formulation in *Suppe (2007)*, wherein the equilibrium equation for a spatially homogeneous wedge is written in terms of two strength parameters that collect all of the fault and wedge strength terms. In effect, this allows us to incorporate knowledge of the detailed internal state within two simple parameters and make predictions about the shear stress along the basal surface. We extend

Suppe's (2007) approach by applying it to the approximate theory for a mechanically heterogeneous wedge that was developed by *Fletcher* (1989) and *Dahlen* (1990).

There is now a large amount of data that characterizes the internal state and geometry of the Nankai accretionary prism in southwest Japan (e.g. *Tobin and Kinoshita*, 2006). Additionally, a large-scale scientific drilling project is being planned for the Hikurangi margin (*Wallace et al.*, 2011). In this paper we develop a mechanical model that can exploit the data sets associated with these projects. We quantify the errors associated with using depth-averaged parameter values and show that they can be accounted for in a simple manner when considering specific heterogeneous distributions of pore pressure or porosity. We also show more generally that for a given taper angle, geologically reasonable, first-order heterogeneities in pore pressure or porosity will result in a lower basal shear stress. A corollary to this is that the taper angle must increase under such heterogeneous conditions if the basal shear stress is fixed. Finally, we show that heterogeneities in the pore pressure ratio have an important effect on the geometry of faults that step up from the basal surface.

4.2. Wedge Analysis

Following the approach of (*Fletcher*, 1989, p. 10,349-10,350) and (*Dahlen*, 1990, p. 89-92), we derive an equation for the equilibrium, or critical, state of a submarine accretionary wedge with spatially varying pore pressure ratio (i.e. deviation from hydrostatic relative to lithostatic pore pressure), bulk density (i.e. porosity), and frictional properties (Figure 4.1). Details are provided in the final section of this chapter; here, we outline our assumptions and present the primary model equations.

We can work either with the lateral gradients of the upper $z_u(x)$ and basal $z_b(x)$ wedge surfaces or the surface slope $\alpha \approx dz_u/dx$ and basal dip $\beta \approx -dz_b/dx$, where

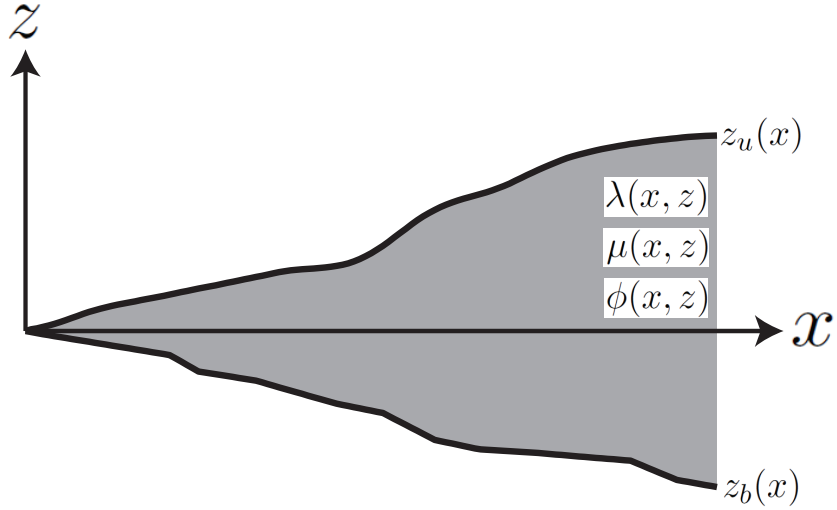


FIGURE 4.1. Coordinate system and cross section cartoon of a heterogeneous wedge.

equivalence is achieved under the small angle approximation. For simplicity, we treat the interior of the wedge as cohesionless (although the derivation in the final section does not), but we allow for the possibility of cohesion along its base. We examine how lateral variations in the normalized basal shear stress $F(x)$ are constrained by the geometry, and a combination of internal properties that can be thought of as the “state parameters” of the wedge. These are the porosity $\phi(x, z)$, the friction coefficient $\mu(x, z)$, and the pore pressure ratio $\lambda(x, z)$, which is defined here as

$$\lambda(x, z) = \frac{p(x, z) - p(x, z_u)}{\sigma_{zz}(x, z) - p(x, z_u)}, \quad (4.1)$$

where $p(x, z)$ and σ_{zz} are the pore fluid pressure and vertical compressive stress within the wedge, and $p(x, z_u)$ is the fluid pressure at the seafloor. Further symbol definitions can be found in Table 4.1.

The normalized basal shear stress was introduced by *Suppe (2007)* and collects basal fault strength terms in a single parameter F that can be thought of as an effective coefficient of friction along the wedge base. For an intrinsic basal friction μ_b

TABLE 4.1. Symbols and definitions. Values are given only for parameters that are held constant throughout this paper. Other parameter values are assigned in the text where appropriate.

Symbol	Definition	Value
α	surface slope	
β	basal dip	
Γ	effective density	
ε	basal shear stress correction	
δ	basal dip correction	
θ	friction angle	
λ	pore pressure ratio	
μ	friction coefficient	
ρ	bulk density	
ρ_f	fluid density	1035 kg m ⁻³
ρ_s	solid density	2650 kg m ⁻³
σ_{ij}	stress tensor components	
τ_b	basal shear stress	
ϕ	porosity	
ϕ_0	porosity at upper surface	0.6
ϕ_c	cut-off porosity	0.05
b	porosity exponent	
F	normalized basal shear stress	
S	basal cohesion	0
z_u	location of upper surface	
z_b	location of basal surface	

and cohesion S_b we have

$$F = \frac{\tau_b}{g\bar{\rho}H} = \mu_b(1 - \lambda_b) + \frac{S_b}{g\bar{\rho}H}. \quad (4.2)$$

And in the equilibrium state

$$F(x) = \frac{\Gamma(x) - \rho_f dz_u}{\bar{\rho}(x) dx} - \frac{\Gamma(x) - \bar{\rho}(x) dz_b}{\bar{\rho}(x) dx} + \frac{H(x) d\Gamma}{2\bar{\rho}(x) dx}, \quad (4.3)$$

where ρ_f is the fluid density, $\bar{\rho}(x)$ is the depth-averaged bulk density, and $H(x) = z_u - z_b$ is the local wedge thickness. The main challenge in solving equation (4.49)

lies in computing Γ , defined as

$$\Gamma(x) = \frac{2}{H^2} \int_{z_b}^{z_u} \Lambda(x, z) \left[\int_z^{z_u} \rho(x, z') dz' \right] dz, \quad (4.4)$$

where

$$\Lambda(x, z) = 1 + 2(1 - \lambda) \frac{\sin \theta}{1 - \sin \theta}. \quad (4.5)$$

We refer to Γ as the “effective density”. It depends on the bulk density ρ and shares those units. It is the only variable that includes the effects of pore pressure and friction angle $\theta = \tan^{-1} \mu$ within the wedge interior. Importantly, the effective density varies only in x .

4.3. Results

It is common in the literature to conduct wedge analyses for accretionary prisms by adopting a set of state parameters (λ, ρ, μ) that are chosen as representative, average values for the entire wedge (see reviews by *Lallemand et al.*, 1994; *Wang and Hu*, 2006); scarcity of relevant site data has often necessitated such an approach. However, the state parameters of an accretionary prism in nature do vary throughout space, as demonstrated in recent data acquired in Japan at the Nankai subduction margin (*Tobin and Kinoshita*, 2006). Future drilling expeditions off New Zealand are expected to provide similar constraints (*Wallace et al.*, 2011). It is therefore natural to ask how such variations will affect calculations made using the Coloumb wedge theory, and whether alternatives to simple, averaged parameter values might yield improved results.

In this section we examine how spatially varying pore pressure ratio, porosity, and friction coefficient affect the basal shear stress, the taper angle, and the orientation of

internal slip surfaces. To facilitate discussion, we define a wedge state characterized by depth-averaged values for the state parameters, denoted by barred symbols (e.g. $\bar{\lambda}$) and referred to as the depth-averaged state, computed with effective density $\bar{\Gamma}$. To allow for meaningful comparisons between heterogeneous and depth-averaged calculations, when we introduce heterogeneity for a specific parameter, the depth-averaged value of that parameter in the heterogeneous state is used to define the depth-averaged state.

Before considering any specific functional forms for the state parameters, we first discuss some general results of introducing heterogeneity. Several general conclusions follow from equations (4.49) and (4.4) when the pore pressure ratio increases monotonically with depth beneath the wedge surface, porosity decreases monotonically, or the friction coefficient decreases monotonically, so that

$$\frac{\partial \lambda}{\partial z} < 0, \quad \frac{\partial \phi}{\partial z} > 0, \quad \frac{\partial \mu}{\partial z} > 0. \quad (4.6)$$

We further stipulate that $\lambda(x, z_u)$, $\phi(x, z_u)$, and $\mu(x, z_u)$ are constants, and that the increase in wedge thickness with distance from the trench leads to the conditions

$$\frac{d\bar{\lambda}}{dx} \geq 0, \quad \frac{d\bar{\phi}}{dx} \leq 0, \quad \frac{d\bar{\mu}}{dx} \leq 0, \quad (4.7)$$

where x is defined as increasing landward from the trench and z is defined as positive upwards (Figure 4.1). Provided that the geometry of the wedge is known, any spatial distributions of pore pressure ratio, porosity, and friction coefficient that satisfy these conditions are guaranteed (conditionally for friction coefficient) to result in a lower basal shear stress relative to the depth-averaged state. Conversely, if the location of the upper surface and the basal shear stress are known, then distributions satisfying

these conditions will result in a larger basal dip, relative to the depth-averaged state. Proofs of these statements, detailed in the final section of this chapter, follow from the observation that $\Gamma \leq \bar{\Gamma}$ for each case.

For pore pressure ratio and porosity at least, these conditions represent first order effects, in that they are expected to coincide with an increasing degree of tectonic compression typical of accretionary prisms, as distance from the trench and depth increase (*Moore and Vrolijk, 1992*). The assumption that porosity decreases with depth and distance from the trench is supported by a large body of evidence, including seismic (e.g. *Bray and Karig, 1985; Bangs et al., 1990; Kitajima and Saffer, 2014*) and borehole measurements (e.g. *Bray and Karig, 1985; Kitamura et al., 2014*), numerical modeling studies (e.g. *Ellis et al., 2013*), microstructural observations (e.g. *Behrmann and Kopf, 1993*), geophysical measurements (e.g. *Housen et al., 1996; Henry et al., 2003*), and structural studies (e.g. *Moore et al., 2011*).

A decrease in porosity with depth beneath the seafloor also implies the corresponding assumption that the pore pressure ratio will increase with depth and distance from the trench, since to first order, compaction driven decreases in porosity can be expected to coincide with increases in pore pressure (*Bray and Karig, 1985*). These trends are supported by studies that infer pore pressure from the seismic velocity structure (e.g. *Tsuji et al., 2008; Tobin and Saffer, 2009; Kitajima and Saffer, 2012*) and numerical modeling results (e.g. *Bekins and Dreiss, 1992; Saffer and Bekins, 2006*).

Gradients in the pore pressure ratio drive fluid flow. If bulk density is constant, then the hydrostatic value of the pore pressure ratio is $\lambda_h = \rho_f/\rho$. When bulk density increases with depth, λ_h must actually decrease with depth. Thus, it is possible to have a situation where the overpressure (pore pressure above hydrostatic)

is increasing with depth (and thus driving upward fluid flow), but the pore pressure ratio is constant, or even decreasing with depth. This happens when the vertical pore pressure gradient is only slightly above the hydrostatic value. However, in most accretionary wedges, pore pressure along the base of the wedge can be significantly greater than the hydrostatic value and in some cases it approaches the lithostatic value (e.g. *Screaton et al.*, 2002; *Saffer*, 2003; *Calahorrano et al.*, 2008; *Skarbek and Saffer*, 2009; *Tobin and Saffer*, 2009; *Saffer and Tobin*, 2011). It is therefore common for the pore pressure ratio to increase with depth in natural settings, since it must assume the hydrostatic value at the seafloor.

It should be noted that the monotonic increase in pore pressure ratio with depth considered here may only be valid in the outer prism (the portion of the accretionary prism that overlies the nominally aseismic section of the plate boundary). Numerical modeling studies (e.g. *Saffer and Bekins*, 1998; *Spinelli and Saffer*, 2004) and indications from seismic data (*Calahorrano et al.*, 2008; *Tobin and Saffer*, 2009) suggest that a reduction in pore pressure ratio can be associated with the onset of seismogenic locking on the plate interface (*Saffer and Tobin*, 2011). Additionally, one expects that the effects of complications involving lateral compressive stresses (e.g. *Bray and Karig*, 1985), wedge faults (e.g. *Saffer and Tobin*, 2011), or thermal/diagenetic conditions (e.g. *Moore and Vrolijk*, 1992) could push pore pressure and porosity–depth trends away from simple monotonic functions. This is especially true at greater depths and further landward from the deformation front (*Saffer and Bekins*, 2006).

For the friction coefficient or friction angle, it is not necessarily the case that either a decrease or increase with depth should be a general feature in accretionary settings. Many effects could lead to either situation. For example, changes in lithology

or mineralogy due to overthrusting and mélangé formation could lead to either condition (*Shreve and Cloos, 1986; Moore and Byrne, 1987*). Diagenetic changes could cause an increase in friction coefficient with depth (e.g. *Saffer and Marone, 2003*). Conversely, development of foliations could be responsible for a decrease with depth. In the absence of more firm and general constraints, we do not consider any specific functional forms for heterogeneities in the friction coefficient.

4.3.1. Basal Shear Stress

The magnitude of the reduction in basal shear stress that results from heterogeneous parameter distributions depends on the specific functional forms and parameter values used. For the purposes of illustration, in this section we adopt simple depth-dependent analytical expressions for the pore pressure ratio and porosity in turn, and compute the effect on the basal shear stress when compared to that predicted for the depth-averaged state. In each case the parameter that is allowed to vary with space (λ or ϕ) is considered the only source of heterogeneity within the wedge; the other state variables are assigned depth-averaged values. We assume for simplicity that the wedge has a constant taper angle, in which case it is more natural to write the equations in terms of the wedge surface slope α and dip angle β , rather than the wedge profile gradients.

We compute normalized basal shear stresses for both the depth-averaged \bar{F}_i and heterogeneous states F_i , where the subscript $i = \lambda, \phi$ indicates the parameter that is allowed to vary. Results are presented as corrections to \bar{F}_i , so that F_i in the heterogeneous cases can be written as $F_i = \bar{F}_i(1 + \varepsilon_i)$, and equation (4.49) implies

that the correction ε_i can be expressed as

$$\varepsilon_i(x) = \frac{(\Gamma_i - \bar{\Gamma}_i)(\alpha + \beta) + \frac{H}{2} \frac{d}{dx} (\Gamma_i - \bar{\Gamma}_i)}{(\bar{\Gamma}_i - \bar{\rho})(\alpha + \beta) + (\bar{\rho} - \rho_f)\alpha + \frac{H}{2} \frac{d\bar{\Gamma}_i}{dx}}. \quad (4.8)$$

Further details can be found in the final section.

We first consider a linear increase of the pore pressure ratio from a hydrostatic value λ_h at the upper surface to a value $\lambda_b(x) \leq 1$ at the base, so that

$$\lambda(x, z) = \left(\frac{z_u - z}{H} \right) [\lambda_b(x) - \lambda_h] + \lambda_h, \quad (4.9)$$

which has a depth-averaged value of $\bar{\lambda} = (\lambda_b + \lambda_h)/2$. There are few spatially extensive data sets with direct measurements of pore pressure within accretionary prisms; most recent attempts link seismic velocity and/or porosity to pore pressure using experimental results and assuming a ratio of lateral to vertical stress in conjunction with specific failure criteria or rheological constitutive models (e.g. *Moore and Tobin, 1997; Tsuji et al., 2008; Saffer and Tobin, 2011; Kitajima and Saffer, 2012*). Although there is considerable scatter in such predictions, the depth trends presented in these studies are nevertheless well approximated by the functional form adopted in equation (4.56).

Inserting equation (4.56) into equation (4.4) and integrating, the effective density is

$$\Gamma_\lambda(x) = \rho \left[1 + 2 \left(1 - \frac{2\lambda_b(x) + \lambda_h}{3} \right) \frac{\sin \theta}{1 - \sin \theta} \right]. \quad (4.10)$$

Equation (4.58) corresponds with the solution for $\bar{\Gamma}$ in a depth-averaged wedge with a pore pressure ratio of $\bar{\lambda}(x) = (2\lambda_b + \lambda_h)/3$. In other words, the effective density for a heterogeneous wedge with pore pressure ratio described by equation (4.56) is

equivalent to that for a depth-averaged wedge where the pore pressure ratio is equal to $(2\lambda_b + \lambda_h)/3$ instead of the actual depth-average of equation (4.56), which is $\bar{\lambda} = (\lambda_b + \lambda_h)/2$. Equation (4.49) implies that the normalized basal shear stress is

$$F_\lambda(x) = \left(1 - \frac{\rho_f}{\rho}\right) \alpha + \frac{2 \sin \theta}{1 - \sin \theta} \left[\left(1 - \frac{2\lambda_b(x) + \lambda_h}{3}\right) (\alpha + \beta) - \frac{H}{3} \frac{d\lambda_b}{dx} \right], \quad (4.11)$$

so that the correction to the depth-averaged case can be expressed as

$$\varepsilon_\lambda(x) = \frac{-2(\lambda_b(x) - \lambda_h)(\alpha + \beta) - H \frac{d\lambda_b}{dx}}{12 \left(1 - \frac{\lambda_b(x) + \lambda_h}{2}\right) (\alpha + \beta) + \frac{6(1 - \sin \theta)}{\sin \theta} \left(1 - \frac{\rho_f}{\rho}\right) \alpha - 3H \frac{d\lambda_b}{dx}}. \quad (4.12)$$

This provides a particular illustration that agrees with our previous, general statement: the basal shear stress correction is always negative when the pore pressure ratio increases with depth.

In Figure 4.2 we show the predictions of equations (4.11) and (4.12) as a function of λ_b . For all calculations we set $\alpha = 2^\circ$, $\beta = 3^\circ$, and assume a wedge thickness of 1000 m at the trench; these are typical values for sedimentary accretionary prisms (*Lallemand et al.*, 1994). To simplify the calculation we assume that λ_b is constant throughout the wedge, so that neither the heterogeneous nor the depth-averaged state effective densities depend on distance from the trench. We then calculate \bar{F}_λ , F_λ , and ε_λ for values ranging between $\lambda_b = 0.48$ (hydrostatic pore pressure) to $\lambda_b = 1$ (lithostatic pore pressure). In this way each value of F_λ or ε_λ in Figure 4.2 corresponds to an individual value of λ_b , so that the locus of points represents a collection of wedges. As indicated above, the heterogeneous state basal shear stress is less than that of the depth-averaged state for all values of λ_b . The magnitude of the correction ε_λ increases from 0 to about 0.25 as λ_b increases. This is a significant change. For example, if $\lambda_b = 0.9$, which corresponds to an average pore pressure in

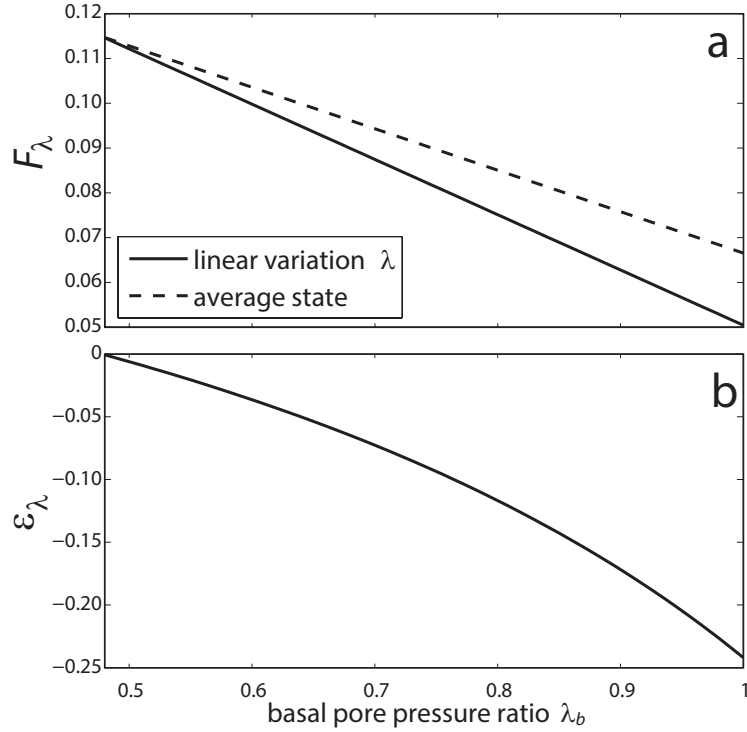


FIGURE 4.2. (a) Normalized basal shear stress resulting from a linear increase in pore pressure ratio with depth (solid line), compared with that for the depth-averaged state (dashed line), and (b) the corresponding correction. Other parameters: $\alpha = 2^\circ$, $\beta = 3^\circ$, $\bar{\phi} = 0.3$, $\bar{\mu} = 0.6$.

the wedge just under half-way between hydrostatic and lithostatic, using the average value overestimates the basal shear stress by about 17%. However, this error can be completely avoided simply by setting the pore pressure ratio equal to $(2\lambda_b + \lambda_h)/3$. This will be an excellent approximation in any setting where the pore pressure ratio exhibits a close to linear increase with depth. In general, our analysis suggests that when performing depth-averaged wedge calculations, weighting the pore pressure ratio towards the basal value will yield an improved approximation.

We next consider the effects of an exponential decrease in porosity with depth from a fixed value ϕ_0 at the upper surface towards a cut-off porosity ϕ_c , such that

$$\phi(x, z) = (\phi_0 - \phi_c)e^{-b(z_u - z)} + \phi_c, \quad (4.13)$$

with depth-average

$$\bar{\phi}(x) = \frac{\phi_0 - \phi_c}{bH} (1 - e^{-bH}) + \phi_c . \quad (4.14)$$

Use of exponential relations like equation (4.13) to describe porosity in accretionary prisms is nearly ubiquitous and supported by a large body of observational data (e.g. *Bray and Karig, 1985; Moore and Vrolijk, 1992; Bekins and Dreiss, 1992; Breen and Orange, 1992; Saffer and Bekins, 1998, 2006*).

We repeat the procedure described above using heterogeneous porosity described by equation (4.13). In this case the heterogeneous effective density is

$$\Gamma_\phi(x) = \Lambda \left[\rho_c + \frac{2}{bH} (\rho_0 - \bar{\rho}) \right] = \Lambda \hat{\rho}(x) , \quad (4.15)$$

where $\rho_0 = \rho(x, z_u)$, $\rho_c = \rho_s + (\rho_f - \rho_s)\phi_c$, $\bar{\rho} = \rho_s + (\rho_f - \rho_s)\bar{\phi}$. The depth-averaged effective density is $\bar{\Gamma}_\phi(x) = \Lambda\bar{\rho}$. Similar to the pore pressure ratio case, equation (4.65) is the effective density for a wedge where the bulk density has no depth dependence and is equal to $\hat{\rho} = \rho_c + 2(bH)^{-1}(\rho_0 - \bar{\rho})$. The heterogeneous normalized basal shear stress is

$$F_\phi(x) = \left(1 - \frac{\rho_f}{\bar{\rho}} \right) \alpha + (\Lambda - 1) (\alpha + \beta) , \quad (4.16)$$

and the corresponding homogeneous normalized basal shear stress is

$$\bar{F}_\phi(x) = \left(1 - \frac{\rho_f}{\bar{\rho}} \right) \alpha + (\Lambda - 1) (\alpha + \beta) + \frac{\Lambda H}{2\bar{\rho}} \frac{d\bar{\rho}}{dx} . \quad (4.17)$$

This is notable in that the heterogeneous value F_ϕ does not depend on the lateral gradient of the depth-averaged bulk density in any way, even though this gradient is non-zero in the heterogeneous state. In other words, ignoring the gradient actually gives a more accurate result. The corresponding correction to the normalized basal

shear stress is

$$\varepsilon_\phi(x) = \Lambda \frac{\left(\frac{\hat{\rho}}{\bar{\rho}} - 1\right)(\alpha + \beta) - \frac{1}{2} \left[\frac{\hat{\rho} + \rho_0 + bH\rho_c}{\bar{\rho}} - 2 - bH \right] \frac{dH}{dx}}{(\Lambda - 1)(\alpha + \beta) + \left(1 - \frac{\rho_f}{\bar{\rho}}\right) \alpha - \frac{1}{2} \left[\frac{\rho_0 + bH\rho_c}{\bar{\rho}} - 1 - bH \right] \frac{dH}{dx}}. \quad (4.18)$$

The results for porosity are a bit more complex than the pore pressure ratio results. Because of the cut-off formulation that we use for porosity, both \bar{F}_ϕ and F_ϕ depend on the wedge thickness in a way that cannot be ignored. This is illustrated in Figures 4.3a and 4.3b, which show the results for a single wedge calculation with $b = 6.5 \times 10^{-4} \text{ m}^{-1}$ ($b^{-1} \approx 1.5 \text{ km}$). For all of our porosity calculations we set $\phi_0 = 0.6$ and $\phi_c = 0.05$. The magnitude of the porosity correction ε_ϕ reaches a maximum value at $\sim 13 \text{ km}$. Once past this value, the correction in Figure 4.3b begins to decrease and asymptotically approaches 0 with increased distance from the trench.

To report general porosity results, we calculate \bar{F}_ϕ , F_ϕ , and ε_ϕ for a range of values of $b = 10^{-5} - 10^{-2} \text{ m}^{-1}$. For each value of b we report the mean value of these three quantities over the frontal 30 km of the wedge, so that as for the pore pressure ratio results, the locus of points in Figures 4.3c and 4.3d represent a collection of wedges. On the secondary axis we also show the e -folding depth b^{-1} , the depth below seafloor at which the porosity has decreased from ϕ_0 by a factor of e^{-1} . The e -folding depth represents a more intuitive, physical quantity to reference in discussing the results.

The results show that the correction is always negative, and has a well defined minimum (i.e. maximum magnitude) that is due mainly to the behavior of the depth-averaged model (Figures 4.3c and 4.3d). The correction asymptotically approaches zero with increases or decreases from this minimum. This is explained by the fact that heterogeneous porosity distributions with large or small e -folding depths have

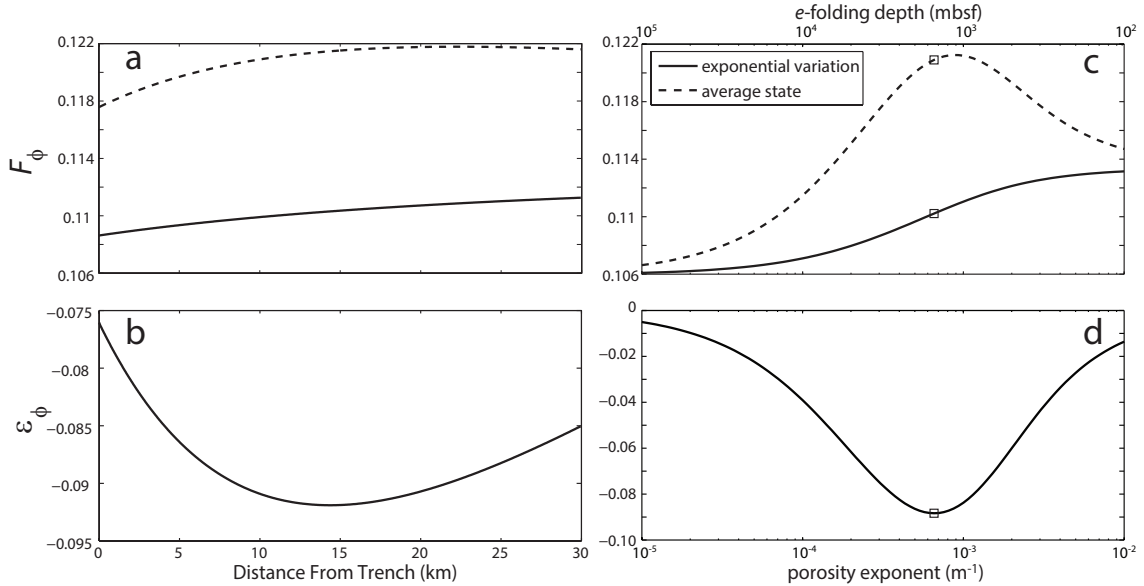


FIGURE 4.3. (a) Normalized basal shear stress over the frontal 30 km resulting from an exponential decrease in porosity with depth (solid line), compared with that for the depth-averaged state (dashed line), and (b) the corresponding correction for a single wedge calculation with $b = 6.5 \times 10^{-4} \text{ m}^{-1}$. (c) Normalized basal shear stress averaged over the frontal 30 km for the exponential (solid line) and depth-averaged (dashed line) states and (d) the corresponding correction. The boxes correspond to the simulation shown in (a) and (b). Other parameters: $\alpha = 2^\circ$, $\beta = 3^\circ$, $\bar{\lambda} = 0.5$, $\bar{\mu} = 0.6$.

little spatial variation and are therefore similar to the corresponding depth-averaged states. When b^{-1} is large, the vertical porosity gradient is small and there is not much variation from ϕ_0 within the wedge. When b^{-1} is small, the porosity reaches ϕ_c close to the surface and does not deviate substantially from that value. Hence, both situations result in small corrections.

It is notable that all of the complexity in the basal shear stress correction is due to the extra term in equation (4.17) compared to equation (4.16). In fact, the most important aspect of the porosity results is the simplicity of the expression for the heterogeneous normalized basal shear stress F_ϕ . Equation (4.16) is equivalent to the prediction one obtains for a wedge with constant internal properties under the small taper angle approximation (e.g. equation (86) in *Dahlen, 1990*), so it is remarkable

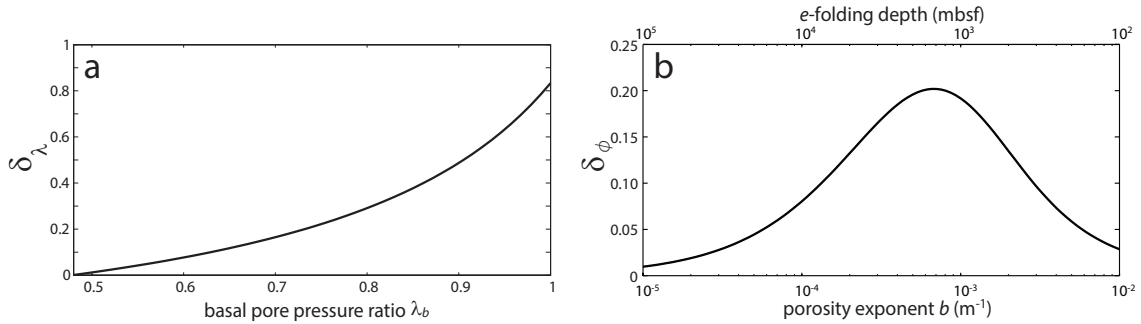


FIGURE 4.4. Corrections to the equilibrium basal dip angle resulting from (a) linear pore pressure with $\bar{\phi} = 0.3$, and (b) exponential porosity with $\bar{\lambda} = 0.5$. Other parameters: $\alpha = 2^\circ$, $\beta = 3^\circ$, $\bar{\mu} = 0.6$.

that this equation fully accounts for the heterogeneous porosity distribution described by equation (4.13).

4.3.2. Taper Angle

In general the surface slopes and basal dips of accretionary prisms are well known. However, in some settings there are areas where the location of the basal surface is either poorly resolved, or there are multiple candidate surfaces for the base of the prism (e.g. *Moore et al.*, 2009). The question naturally arises: how does introducing heterogeneity affect the taper angle? In considering the answer, we fix the surface slope α (which should always be known in natural settings) and calculate the affect of heterogeneities on the basal dip β . For simple, monotonic variations that satisfy equation (4.72), the result is always an increase in β relative to the depth-averaged model when the basal shear stress is fixed.

Following a procedure analogous to that in Section 4.1, corrections to the basal dip of the form $\beta_i = \bar{\beta}_i(1 + \delta_i)$ are shown in Figure 4.4 for the relations given in equations (4.56) – (4.64). With a linear depth dependence for pore pressure ratio and

assuming λ_b constant as before, this correction can be expressed as

$$\delta_\lambda(x) = \frac{(\lambda_b - \lambda_h) \left[F - \left(1 - \frac{\rho_f}{\bar{\rho}} \right) \alpha \right]}{2(3 - 2\lambda_b - \lambda_h) \left[F - \left(\bar{\Lambda} - \frac{\rho_f}{\bar{\rho}} \right) \alpha \right]}. \quad (4.19)$$

The correction δ_ϕ for cut-off porosity is computed numerically due to the dependence on x in equation (4.65)(see final section for details).

As in Section 4.1, the effect of heterogeneities in pore pressure ratio is typically expected to be larger than that of porosity variations, although the difference is more pronounced for each than it was for the predictions of basal shear stress. The porosity results show that for a large vertical porosity gradient, the basal dip can be about 20% larger than expected from a depth-averaged model. However, when there is a large vertical pressure gradient, the predicted basal dip can be 80% larger than the depth-averaged state. Two examples are shown in Figure 4.5.

4.3.3. Slip Surfaces

Critical Coulomb wedges are by definition at failure everywhere. Therefore at any point within the wedge there are two potential slip surfaces, oriented at angles $\pm(\pi/4 - \theta/2)$ with respect to the orientation of the maximum principal stress σ_1 (*Jaeger and Cook, 1969*). In a homogeneous, non-cohesive wedge, the orientation of σ_1 is the same everywhere and so the dips of the slip surfaces do not depend on position within the wedge (*Davis et al., 1984*). However, the presence of heterogeneities serves to rotate the direction of σ_1 as a function of depth, and cause the slip surfaces to become non-planar.

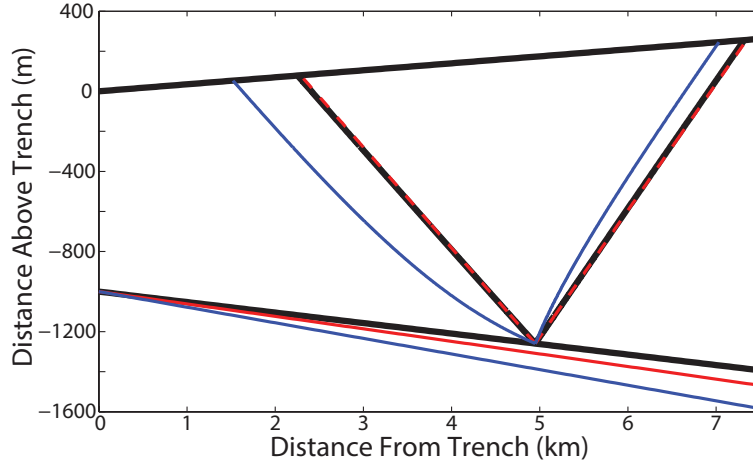


FIGURE 4.5. Example equilibrium wedge profiles and slip surfaces for linear pore pressure ratio (blue lines $\beta = 4.5^\circ$, $\lambda_b = 0.9$, $\bar{\phi} = 0.3$) and exponential porosity (red lines $\beta = 3.6^\circ$, $b = 6.6 \times 10^{-4} \text{ m}^{-1}$, $\bar{\lambda} = 0.5$). Black lines show the corresponding depth-averaged state $\alpha = 2^\circ$, $\bar{\beta} = 3^\circ$, $\bar{\lambda} = 0.5$, $\bar{\phi} = 0.3$, $\bar{\mu} = 0.6$.

The stress state of a heterogeneous wedge is completely determined by the equilibrium analysis and is given by

$$\sigma_{zz}(x, z) = g \left[\rho_f(D - z_u) + \int_z^{z_u} \rho(x, z') dz' \right], \quad (4.20)$$

$$\sigma_{xx}(x, z) = g \left[\rho_f(D - z_u) + \Lambda(x, z) \int_z^{z_u} \rho(x, z') dz' \right], \quad (4.21)$$

$$\sigma_{xz}(x, z) = g \int_z^{z_u} \left[\rho_f \frac{dz_u}{dx} - \frac{\partial}{\partial x} \left(\Lambda(x, z) \int_{z'}^{z_u} \rho(x, \xi) d\xi \right) \right] dz', \quad (4.22)$$

Knowing the stress state, it is straightforward to calculate the orientation of σ_1 and thus plot the slip lines in the wedge. We again consider the effects of heterogeneities described by equations (4.56) and (4.13), and compare the geometry of the slip surfaces to those expected for the depth-averaged state. We calculated the slip lines in Figure 4.5 using the same parameters used to calculate the alternative basal surfaces in the same figure, but with the stress state taken from the fixed geometry solution (shown by the black lines in Figure 4.5).

Heterogeneous porosity has a negligible effect on the slip surfaces. This is because the bulk density only appears in the stress state as a depth-integrated quantity; since the depth-average of the porosity distribution is defined as an integral over depth, the two states are very similar. However, although the effect is difficult to see at the resolution shown for Figure 4.5, the heterogeneous slip lines for porosity are slightly rotated clock-wise from the average slip lines.

Imposing a linear depth dependence for the pore pressure ratio has a more significant affect, especially for the seaward vergent slip surfaces, which acquire a listric geometry. The resulting slip lines are rotated counter-clockwise, and have a concave shape relative to those predicted from the depth-averaged state model. This coincides with the style of seaward vergent, imbricate thrusts commonly observed in accretionary prisms (e.g. *Davis and Hyndman, 1989; Bangs et al., 1990; Flueh et al., 1998; Moore et al., 2001; Barker et al., 2009; Smith et al., 2012*), which can also be produced in depth-averaged Coulomb wedge models that include cohesion (*Dahlen and Suppe, 1984*).

4.4. Conclusions

Our results illustrate the importance of including heterogeneity in Coulomb wedge calculations. It is important to re-emphasize that illustrative examples provided in Section 4 are concerned with first-order variations that can be approximately described by the conditions defined by equations (4.72). Effects that we term “second-order” (e.g. accretionary mélange formation, focussed flow through wedge faults, diagenetic effects) will cause deviations from these conditions.

All of our results suggest that variations in the pore pressure ratio should be given greater consideration than variations in porosity. The porosity in submarine

accretionary prisms is expected to be fairly well described by an exponential decrease with depth and distance from the trench. Our results show that porosity distributions of this type can easily be accounted for simply by using a depth-averaged value as a function of distance from the trench, rather than a single value for the entire wedge. Similarly, we have shown that the effects of a linear increase in the pore pressure ratio with depth and distance from the trench can be accounted for by using a depth-independent value that is weighted towards the basal pore pressure ratio. Although pore pressure in accretionary prisms is typically far less well constrained than porosity, the simple linear spatial dependence used here is proposed as a reasonable first approximation. More precise estimates could be made with considerations of how fluid flow affects the pore pressure distribution within an accretionary prism (e.g. *Rowe et al.*, 2012).

Our inference about the importance of heterogeneities in the pore pressure ratio is lent further support by the form of splay faults predicted using heterogeneous state properties. Whereas porosity variations cause practically no change from the linear surfaces predicted by the depth-averaged model, pore pressure variations cause large rotations from the surfaces predicted using the depth-averaged state and impart a listric form to seaward vergent surfaces that coincides with observations of natural accretionary prisms.

A productive and natural strategy for gaining insight into the behavior of heterogeneous geological systems involves applying simplified model treatments that account only for those features that are essential to understanding the overall behavior. Coulomb wedge models have exemplified this approach, and have been enormously successful at elucidating the mechanics of accretionary margins. Now, with vastly improved resolution of site characteristics determined at great expense

from recent and ongoing surveys, responsible modeling strategies must evolve to better approximate those geologic heterogeneities that are actually observed. Our analysis demonstrates that the predictions from heterogeneous wedge models can deviate significantly from predictions made using the simplest possible averaging procedure to define a homogeneous wedge model. In an upcoming paper we will use the results obtained here in an analysis of the Kumano transect along the Nankai accretionary prism in southwest Japan.

4.5. Model Derivation

This derivation follows those by (*Fletcher*, 1989, p. 10,349-10,350) and (*Dahlen*, 1990, p. 89-92). The equations found below give the equilibrium state of a submerged wedge with irregular upper and basal surfaces, as well as spatially varying mechanical properties and pore pressure. Our derivation differs from those of *Fletcher* (1989) and *Dahlen* (1990) primarily in that our coordinate system is defined with the z axis pointing sky-ward, additionally we work with the lateral gradients of the upper and basal wedge surfaces rather than the surface slope α and basal dip β . However, the results obtained by *Dahlen* (1990) are recovered by setting $dz_u/dx = \alpha$ and $dz_b/dx = -\beta$ in equation (4.49) (c.f. *Dahlen*, 1990, equation (98)).

The derivation is carried out in two dimensions for a static wedge (i.e. inertia is negligible). The equations of static equilibrium are

$$\frac{\partial \sigma_{xx}}{\partial x} + \frac{\partial \sigma_{xz}}{\partial z} + b_x = 0, \quad (4.23)$$

$$\frac{\partial \sigma_{xz}}{\partial x} + \frac{\partial \sigma_{zz}}{\partial z} + b_z = 0. \quad (4.24)$$

Lateral body forces are not considered, so $b_x = 0$. If we adopt the convention that compressive stresses are positive, then the body force due to gravity is $b_z = g\rho(x, z)$, where g is gravitational acceleration, and ρ is the bulk density of the material composing the wedge. Now, make the approximation

$$\left| \frac{\partial \sigma_{xz}}{\partial x} \right| \ll \left| \frac{\partial \sigma_{zz}}{\partial z} \right|, \quad (4.25)$$

which can be checked *a posteriori* and is implied by use of the small angle approximation of the wedge taper. Using the approximation (4.25), equation (4.24) can be integrated to obtain

$$\sigma_{zz}(x, z) = -g \int_{z_b(x)}^z \rho(x, z') dz' + f(x), \quad (4.26)$$

where the integration is from the basal surface $z_b(x)$ to some point z within the wedge. Henceforth we will drop the argument of $z_b(x)$, but keep in mind that it is a function of distance x from the trench, as is the upper surface $z_u(x)$. To find the function $f(x)$, we make use of the boundary condition on the normal stress σ_{zz} along the upper surface. This condition is simply that the magnitude of the normal stress on the upper surface is equal to the fluid pressure

$$\sigma_{zz}(x, z_u) = p_f(x, z_u) = g\rho_f(D - z_u), \quad (4.27)$$

where D is the depth of the water at the trench, so that $D - z_u$ is the lateral water depth profile. From equation (4.26)

$$f(x) = g \int_{z_b}^{z_u} \rho(x, \xi) d\xi + p_f(x, z_u). \quad (4.28)$$

So the vertical compressive stress becomes

$$\begin{aligned}\sigma_{zz}(x, z) &= g \left[\int_z^{z_b} \rho(x, z') dz' + \int_{z_b}^{z_u} \rho(x, z') dz' \right] + p_f(x, z_u) , \\ &= g \int_z^{z_u} \rho(x, z') dz' + g\rho_f(D - z_u) .\end{aligned}\tag{4.29}$$

The yield condition for a cohesive Coulomb material is (*Malvern, 1977*)

$$\left[\frac{1}{2}(\sigma_{zz} - \sigma_{xx}) \right]^2 + \sigma_{xz}^2 - \left[S(x, z) \cos \theta(x, z) - \frac{1}{2}(\sigma_{xx} + \sigma_{zz} + 2p_f) \sin \theta(x, z) \right]^2 = 0 ,\tag{4.30}$$

where S is the cohesion and θ is the angle of internal friction within the wedge; both are allowed to vary with position. Next, make the assumption

$$2|\sigma_{xz}| \ll |\sigma_{zz} - \sigma_{xx}| .\tag{4.31}$$

This condition can also be checked *a posteriori* and is again implied by use of the small angle approximation. Using this approximation, the yield criterion can be rewritten for σ_{xx} as

$$\sigma_{xx} = C + 2(\sigma_{zz} - p_f) \frac{\sin \theta}{1 - \sin \theta} + \sigma_{zz} ,\tag{4.32}$$

where the uniaxial compressive strength C is defined as

$$C(x, z) = \frac{2 \cos \theta}{1 - \sin \theta} S ,\tag{4.33}$$

keeping in mind that the angle of internal friction θ and the cohesion S may both be functions of x and z within the wedge.

Now, define the pore pressure ratio as

$$\lambda(x, z) = \frac{p_f - p_f(x, z_u)}{\sigma_{zz} - p_f(x, z_u)}, \quad (4.34)$$

which is a convenient way of expressing the pore pressure, and essentially references the pressure in the wedge to that at the seafloor. Using this definition, along with the expression for σ_{zz} , equation (4.32) may be written as

$$\sigma_{xx}(x, z) = C(x, z) + g\rho_f(D - z_u) + g\Lambda(x, z) \int_z^{z_u} \rho(x, \xi) d\xi, \quad (4.35)$$

where

$$\Lambda(x, z) = 1 + 2(1 - \lambda) \frac{\sin \theta}{1 - \sin \theta}. \quad (4.36)$$

Now to deal with the other equilibrium equation by taking the derivative of equation (4.35) with respect to x , substituting the result into equation (4.23), and integrating with respect to z

$$\sigma_{xz}(x, z) = - \int_{z_b}^z \left[\frac{\partial C}{\partial x} - g\rho_f \frac{dz_u}{dx} + g \frac{\partial}{\partial x} \left(\Lambda \int_{z'}^{z_u} \rho d\xi \right) \right] dz' + G(x). \quad (4.37)$$

The function $G(x)$ can be found by using the boundary condition for the shear stress τ_b on the basal surface. Since the basal surface is inclined relative to the coordinate axes, the shear stress there can be written in terms of the stress tensor components and z_b by using the tensor transformation equation

$$\bar{\mathbf{T}} = \mathbf{A}^T \mathbf{T} \mathbf{A}, \quad (4.38)$$

where A is the matrix of direction cosines. Making use of the small angle approximation, the result is

$$\tau_b(x) = \sigma_{xz} + (\sigma_{zz} - \sigma_{xx})\beta(x) + \mathcal{O}(\beta^2) \quad (4.39)$$

where $\beta(x)$ is the dip angle of the basal surface. Then setting $\beta = -dz_b/dx$, the boundary condition on the shear stress at the basal surface becomes

$$\sigma_{xz}(x, z_b) = \tau_b(x) - [\sigma_{zz} - \sigma_{xx}]|_{(x, z_b)} \frac{dz_b}{dx} \quad (4.40)$$

Now $G(x)$ can be found by evaluating equation (4.37) at z_b and making use of basal boundary condition along with the definitions of σ_{xx} and σ_{zz} evaluated at z_b as well.

So that,

$$G(x) = \left[C(x, z_b) - g(1 - \Lambda(x, z_b)) \int_{z_b}^{z_u} \rho dz \right] \frac{dz_b}{dx} + \tau_b. \quad (4.41)$$

The shear stress within the wedge can now be written as

$$\begin{aligned} \sigma_{xz}(x, z) = & - \int_{z_b}^z \left[\frac{\partial C}{\partial x} - g\rho_f \frac{dz_u}{dx} + g \frac{\partial}{\partial x} \left(\Lambda \int_{z'}^{z_u} \rho d\xi \right) \right] dz' \\ & + \left[C(x, z_b) - g(1 - \Lambda(x, z_b)) \int_{z_b}^{z_u} \rho dz \right] \frac{dz_b}{dx} + \tau_b. \end{aligned} \quad (4.42)$$

The boundary condition on the shear stress on the upper surface provides the final equation for the equilibrium state of the wedge. Shear stress must vanish on the upper surface, so making use of the small angle approximation, the result is

$$0 = -\sigma_{xz} + (\sigma_{xx} - \sigma_{zz})\alpha(x) + \mathcal{O}(\alpha^2). \quad (4.43)$$

Then setting $\alpha = dz_u/dx$, the boundary condition for the shear stress at the upper surface becomes

$$\sigma_{xz}(x, z_u) = [\sigma_{xx} - \sigma_{zz}]_{(x, z_u)} \frac{dz_u}{dx} = C(x, z_u) \frac{dz_u}{dx}, \quad (4.44)$$

where the final equality comes from substituting in the definitions of σ_{xx} and σ_{zz} , evaluated at z_u . The equilibrium state of the wedge is found by evaluating equation (4.42) at z_u and substituting the result into equation (4.44), to get

$$\begin{aligned} & - \int_{z_b}^{z_u} \left[\frac{\partial C}{\partial x} - g\rho_f \frac{dz_u}{dx} + g \frac{\partial}{\partial x} \left(\Lambda \int_{z'}^{z_u} \rho d\xi \right) \right] dz' \\ & + \left[C(x, z_b) - g(1 - \Lambda(x, z_b)) \int_{z_b}^{z_u} \rho dz \right] \frac{dz_b}{dx} + \tau_b = C(x, z_u) \frac{dz_u}{dx}; \end{aligned} \quad (4.45)$$

Equation (4.45) can be simplified by setting $H(x) = z_u - z_b$ and defining depth averaged parameters (e.g. *Dahlen, 1990*)

$$\bar{\rho} = \frac{1}{z_u - z_b} \int_{z_b}^{z_u} \rho dz, \quad (4.46)$$

$$\bar{C} = \frac{1}{z_u - z_b} \int_{z_b}^{z_u} C dz, \quad (4.47)$$

and

$$\Gamma = \frac{2}{H^2} \int_{z_b}^{z_u} \Lambda(x, z) \left(\int_z^{z_u} \rho(x, z') dz' \right) dz. \quad (4.48)$$

Using these definitions and applying the Leibniz integration rule, equation (4.45) can be written for the basal shear stress as

$$\tau_b(x) = [g(\bar{\rho} - \Gamma)H - \bar{C}] \frac{dz_b}{dx} - [g(\rho_f - \Gamma)H - \bar{C}] \frac{dz_u}{dx} + H \frac{d\bar{C}}{dx} + \frac{1}{2}gH^2 \frac{d\Gamma}{dx}. \quad (4.49)$$

4.6. Simplified Solutions

We are interested in the conditions along the basal surface that are required to satisfy input values of the coefficient of friction, pore pressure, and bulk density within the wedge, under the simplifying assumption that all material within the wedge is cohesionless. In this case the equilibrium equation takes the form

$$F(x) = \frac{\Gamma - \rho_f}{\bar{\rho}} \frac{dz_u}{dx} - \frac{\Gamma - \bar{\rho}}{\bar{\rho}} \frac{dz_b}{dx} + \frac{H(x)}{2\bar{\rho}} \frac{d\Gamma}{dx}, \quad (4.50)$$

where the normalized basal shear stress is defined as

$$F \equiv \frac{\tau_b}{g\bar{\rho}H} = \mu_b(1 - \lambda_b) + \frac{S_b}{g\bar{\rho}H}, \quad (4.51)$$

and where λ_b , μ_b , and S_b are the values of pore pressure ratio, friction coefficient, and cohesion along the basal surface. To solve equation (4.50), the integral Γ and its derivative in the x direction must be computed. We present the results as corrections to the depth-averaged case, such that the normalized basal shear stress in the heterogeneous case is written as $F_i = \bar{F}_i(1 + \varepsilon_i)$, where the subscript $i = \lambda, \phi$ indicates the parameter that is allowed to vary. From equation (4.50), the correction can be written as

$$\varepsilon_i(x) = \frac{(\Gamma_i - \bar{\Gamma}_i)(\alpha + \beta) + \frac{H}{2} \frac{d}{dx} (\Gamma_i - \bar{\Gamma}_i)}{(\bar{\Gamma}_i - \bar{\rho})(\alpha + \beta) + (\bar{\rho} - \rho_f)\alpha + \frac{H}{2} \frac{d\bar{\Gamma}_i}{dx}}. \quad (4.52)$$

In the main text we also give results for the effects of heterogeneity on the location of the basal surface z_b , which we present as a correction to the basal dip angle of a triangular wedge, of the form $\beta_i = \bar{\beta}_i(1 + \delta_i)$. Equation (4.50) can be written as a

solution for the location of z_b so that

$$\frac{dz_b}{dx} = \frac{\bar{\rho}}{\Gamma - \bar{\rho}} \left[\left(\frac{z_u - z_b}{2\bar{\rho}} \right) \frac{d\Gamma}{dx} + \left(\frac{\Gamma - \rho_f}{\bar{\rho}} \right) \frac{dz_u}{dx} - F \right], \quad (4.53)$$

which is a first order ODE for z_b . In general, equation (4.53) must be solved numerically. However, when the depth-averaged and heterogeneous effective densities do not depend on x , as in the linear pore pressure ratio example, then equation (4.53) becomes

$$\beta_i = \frac{\bar{\rho}F - (\Gamma_i - \rho_f)\alpha}{\Gamma_i - \bar{\rho}}, \quad (4.54)$$

and the dip angle correction can be written as

$$\delta_i = \frac{(\chi_i - 1)\bar{\rho}F + [(\bar{\Gamma}_i - \rho_f) - \chi(\Gamma_i - \rho_f)]\alpha}{\bar{\rho}F - (\bar{\Gamma}_i - \rho_f)\alpha}, \quad (4.55)$$

where $\chi_i = (\bar{\Gamma}_i - \bar{\rho})/(\Gamma_i - \bar{\rho})$.

4.6.1. Pore Pressure Ratio

In the first example, we assume that friction and porosity are constant, and that the pore pressure ratio is described by

$$\lambda(x, z) = \frac{z_u - z}{H} [\lambda_b(x) - \lambda_h] + \lambda_h, \quad (4.56)$$

with depth-average $\bar{\lambda}(x) = (\lambda_b + \lambda_h)/2$. Inserting this into equation (4.48), the effective density is

$$\Gamma_\lambda = \bar{\rho} + \frac{4\bar{\rho}}{H^2} \frac{\sin \theta}{1 - \sin \theta} \int_{z_b}^{z_u} (z_u - z) \left[1 - \frac{z - z_u}{H} (\lambda_b - \lambda_h) + \lambda_h \right] dz, \quad (4.57)$$

which has the solution

$$\Gamma_\lambda(x) = \rho \left[1 + 2 \left(1 - \frac{2\lambda_b(x) + \lambda_h}{3} \right) \frac{\sin \theta}{1 - \sin \theta} \right]. \quad (4.58)$$

The lateral gradient of Γ_λ is

$$\frac{d\Gamma_\lambda}{dx} = -\frac{4}{3} \left(\frac{\bar{\rho} \sin \theta}{1 - \sin \theta} \right) \frac{d\lambda_b}{dx}. \quad (4.59)$$

As mentioned in the main text, the effective density in the depth-averaged state $\bar{\Gamma}_\lambda$ has the same form as equation (4.58), with $(2\lambda_b + \lambda_h)/3$ replaced by $(\lambda_b + \lambda_h)/2$.

Therefore its lateral gradient is

$$\frac{d\bar{\Gamma}_\lambda}{dx} = -\left(\frac{\bar{\rho} \sin \theta}{1 - \sin \theta} \right) \frac{d\lambda_b}{dx}. \quad (4.60)$$

With this information, the heterogeneous and homogeneous normalized basal shear stresses can be written as

$$F_\lambda(x) = \left(1 - \frac{\rho_f}{\bar{\rho}} \right) \alpha + \frac{2 \sin \theta}{1 - \sin \theta} \left[\left(1 - \frac{2\lambda_b(x) + \lambda_h}{3} \right) (\alpha + \beta) - \frac{H}{3} \frac{d\lambda_b}{dx} \right], \quad (4.61)$$

$$\bar{F}_\lambda(x) = \left(1 - \frac{\rho_f}{\bar{\rho}} \right) \alpha + \frac{2 \sin \theta}{1 - \sin \theta} \left[\left(1 - \frac{\lambda_b(x) + \lambda_h}{2} \right) (\alpha + \beta) - \frac{H}{2} \frac{d\lambda_b}{dx} \right], \quad (4.62)$$

Substituting the expressions for Γ_λ and $\bar{\Gamma}_\lambda$ and their lateral gradients into equation (4.52) leads to equation (4.12) in the main text for the basal shear stress correction ϵ_λ . Additionally, substituting these expressions into equation (4.55) leads to equation (4.19) in the main text for the basal dip correction δ_λ .

4.6.2. Porosity

In the second example, we assume that friction and the pore pressure ratio are constant, and that the porosity is described by

$$\phi(x, z) = (\phi_0 - \phi_c)e^{-b(z_u - z)} + \phi_c, \quad (4.63)$$

with depth-average

$$\bar{\phi}(x) = \frac{\phi_0 - \phi_c}{bH} (1 - e^{-bH}) + \phi_c, \quad (4.64)$$

The effective density can be calculated by using the definition of bulk density $\rho = \rho_s + (\rho_f - \rho_s)\phi$, and computing the double integral in equation (4.48). After a good amount of algebra, the solution can be expressed as

$$\Gamma_\phi(x) = \Lambda \left[\rho_c + \frac{2}{bH}(\rho_0 - \bar{\rho}) \right] = \Lambda \hat{\rho}(x), \quad (4.65)$$

with lateral gradient

$$\begin{aligned} \frac{d\Gamma_\phi}{dx} &= -\frac{2\Lambda}{bH} \left[\frac{d\bar{\rho}}{dx} + \frac{\rho_0 - \bar{\rho}}{H} \frac{dH}{dx} \right], \\ &= -(\hat{\rho} - \bar{\rho}) \frac{2\Lambda}{H} \frac{dH}{dx}, \end{aligned} \quad (4.66)$$

where we've used the relation

$$\frac{d\bar{\rho}}{dx} = (\rho_s - \rho_f) \frac{d\bar{\phi}}{dx} = [\rho_0 - \bar{\rho} + bH(\rho_c - \bar{\rho})] \frac{1}{H} \frac{dH}{dx}. \quad (4.67)$$

Finally, the homogeneous effective density is given by

$$\bar{\Gamma}_\phi = \Lambda \bar{\rho}, \quad (4.68)$$

with lateral gradient

$$\frac{d\bar{\Gamma}_\phi}{dx} = \Lambda \frac{d\bar{\rho}}{dx}. \quad (4.69)$$

Substituting equations (4.65) and (4.66) into equation (4.50) gives a heterogeneous normalized basal shear stress of

$$F_\phi(x) = \left(1 - \frac{\rho_f}{\bar{\rho}}\right) \alpha + (\Lambda - 1) (\alpha + \beta). \quad (4.70)$$

The corresponding homogeneous state normalized basal shear stress is found by substituting equations (4.68) and (4.69) into equation (4.50), and is given by

$$\bar{F}_\phi(x) = \left(1 - \frac{\rho_f}{\bar{\rho}}\right) \alpha + (\Lambda - 1) (\alpha + \beta) + \frac{\Lambda H}{2\bar{\rho}} \frac{d\bar{\rho}}{dx}. \quad (4.71)$$

Substituting the expressions for Γ_ϕ and $\bar{\Gamma}_\phi$ and their lateral gradients into equation (4.52) leads to equation (4.18) in the main text for the basal shear stress correction ϵ_ϕ . Because of the dependence of Γ_ϕ and $\bar{\Gamma}_\phi$ on x (or wedge thickness H), we calculate the basal dip correction δ_ϕ numerically.

4.7. Proofs

Here we prove the statements in the main text that any spatial distributions of pore pressure ratio, porosity, and friction coefficient that satisfy the following conditions are guaranteed to result in a lower basal shear stress relative to the depth-

averaged state:

$$\frac{\partial \lambda}{\partial z} < 0, \quad \frac{\partial \phi}{\partial z} > 0, \quad \frac{\partial \mu}{\partial z} > 0, \quad (4.72)$$

$$\frac{d\bar{\lambda}}{dx} \geq 0, \quad \frac{d\bar{\phi}}{dx} \leq 0, \quad \frac{d\bar{\mu}}{dx} \leq 0.$$

We further assume that $\lambda(x, z_u)$, $\phi(x, z_u)$, and $\mu(x, z_u)$ are constants. To address this topic we first note that equation (4.52) for the basal shear stress correction can be written as

$$\epsilon_i(x) = \frac{1}{F_i} \left[(\Gamma_i - \bar{\Gamma}) (\alpha + \beta) + \frac{H}{2} \frac{d}{dx} (\Gamma_i - \bar{\Gamma}) \right]. \quad (4.73)$$

Furthermore, from equation (4.48), the lateral gradient of the effective density is

$$\begin{aligned} \frac{d\Gamma}{dx} &= -\frac{4}{H^3} \frac{dH}{dx} \int_{z_b}^{z_u} \Lambda \left(\int_z^{z_u} \rho dz \right) dz' + \frac{2}{H^2} \frac{d}{dx} \left[\int_{z_b}^{z_u} \Lambda \left(\int_z^{z_u} \rho dz \right) dz' \right] \\ &= -\frac{2\Gamma}{H} (\alpha + \beta) + \frac{2}{H^2} \frac{d}{dx} \left[\int_{z_b}^{z_u} \Lambda \left(\int_z^{z_u} \rho dz \right) dz' \right]. \end{aligned} \quad (4.74)$$

So the basal correction becomes

$$\epsilon_i = \frac{\frac{d}{dx} [\psi_i - \bar{\psi}_i]}{H F_i}, \quad (4.75)$$

where

$$\psi = \int_{z_b}^{z_u} \Lambda \left(\int_z^{z_u} \rho dz \right) dz'. \quad (4.76)$$

Since the basal shear stress is assumed to always be positive, showing that the correction is negative amounts to showing that $d(\psi_i - \bar{\psi}_i)/dx < 0$.

4.7.1. Pore Pressure Ratio

First we address the pore pressure ratio case, which compares wedges with pore pressure ratio monotonically increasing with depth, to wedges with pore pressure ratio equal to the average value of the depth dependent case. Both cases have the same constant values for porosity and friction coefficient. Then we must show

$$\begin{aligned} \frac{d}{dx}[\psi_\lambda - \bar{\psi}_\lambda] &= \bar{\rho} \frac{d}{dx} \left\{ \int_{z_b}^{z_u} \left[1 + 2(1 - \lambda) \frac{\sin \theta}{(1 - \sin \theta)} \right] (z_u - z) dz \right. \\ &\quad \left. - \int_{z_b}^{z_u} \left[1 + 2(1 - \bar{\lambda}) \frac{\sin \theta}{(1 - \sin \theta)} \right] (z_u - z) dz \right\} < 0, \end{aligned} \quad (4.77)$$

which reduces to

$$\begin{aligned} \frac{d}{dx}[\psi_\lambda - \bar{\psi}_\lambda] &= \frac{2\bar{\rho} \sin \theta}{(1 - \sin \theta)} \frac{d}{dx} \left\{ \int_{z_b}^{z_u} (z - z_u) [\lambda(x, z) - \bar{\lambda}(x)] dz \right\}, \\ &= \frac{2\bar{\rho} \sin \theta}{(1 - \sin \theta)} \frac{d}{dx} \left\{ \int_{z_b}^{z_u} (z - z_u) g_\lambda(x, z) dz \right\} = \frac{2\bar{\rho} \sin \theta}{(1 - \sin \theta)} \frac{dI_\lambda}{dx} < 0, \end{aligned} \quad (4.78)$$

where we have defined $g_\lambda(x, z) = \lambda(x, z) - \bar{\lambda}(x)$. It's now sufficient to show $dI_\lambda/dx < 0$.

First we apply the Liebniz integration rule to write

$$\begin{aligned} \frac{dI_\lambda}{dx} &= H(\lambda_b - \bar{\lambda}) \frac{dz_b}{dx} + \int_{z_b}^{z_u} \frac{\partial}{\partial x} [(z - z_u) g_\lambda(x, z)] dz, \\ &= H(\lambda_b - \bar{\lambda}) \frac{dz_b}{dx} - \frac{dz_u}{dx} \int_{z_b}^{z_u} g_\lambda(x, z) dz + \int_{z_b}^{z_u} (z - z_u) \frac{\partial g_\lambda}{\partial x} dz. \end{aligned} \quad (4.79)$$

The second term in equation (4.79) is zero, because $\bar{g}_\lambda = 0$ by definition. Then we have

$$\frac{dI_\lambda}{dx} = H(\lambda_b - \bar{\lambda}) \frac{dz_b}{dz_u} + (Z' - z_u) \int_{z_b}^{z_u} \frac{\partial g_\lambda}{\partial x} dz, \quad (4.80)$$

where we have applied the mean value theorem to the last term, with $z_b \leq Z' \leq z_u$.

To proceed we note that

$$\int_{z_b}^{z_u} \frac{\partial g_\lambda}{\partial x} dz = \int_{z_b}^{z_u} \left(\frac{\partial \lambda}{\partial x} - \frac{d\bar{\lambda}}{dx} \right) dz = \int_{z_b}^{z_u} \frac{\partial \lambda}{\partial x} dz - H \frac{d\bar{\lambda}}{dx}. \quad (4.81)$$

Inserting the definition of $\bar{\lambda}$ and differentiating we have

$$\begin{aligned} \int_{z_b}^{z_u} \frac{\partial g_\lambda}{\partial x} dz &= \int_{z_b}^{z_u} \frac{\partial \lambda}{\partial x} dz - H \frac{d}{dx} \left[\frac{1}{H} \int_{z_b}^{z_u} \lambda(x, z) dz \right] \\ &= \int_{z_b}^{z_u} \frac{\partial \lambda}{\partial x} dz + \frac{1}{H} \frac{dH}{dx} \int_{z_b}^{z_u} \lambda(x, z) dz - \frac{\partial}{\partial x} \left[\int_{z_b}^{z_u} \lambda(x, z) dz \right] \\ &= \int_{z_b}^{z_u} \frac{\partial \lambda}{\partial x} dz + \bar{\lambda} \frac{dH}{dx} - \left[\lambda_h \frac{dz_u}{dx} - \lambda_b \frac{dz_b}{dx} + \int_{z_b}^{z_u} \frac{\partial \lambda}{\partial x} dz \right]. \end{aligned} \quad (4.82)$$

The first and last terms in equation (4.82) cancel, leaving

$$\int_{z_b}^{z_u} \frac{\partial g_\lambda}{\partial x} dz = (\bar{\lambda} - \lambda_h) \frac{dz_u}{dx} + (\lambda_b - \bar{\lambda}) \frac{dz_b}{dx}, \quad (4.83)$$

Finally, inserting equation (4.83) into equation (4.80) gives

$$\begin{aligned} \frac{dI_\lambda}{dx} &= (z_u - z_b)(\lambda_b - \bar{\lambda}) \frac{dz_b}{dx} + (Z' - z_u) \left[(\bar{\lambda} - \lambda_u) \frac{dz_u}{dx} + (\lambda_b - \bar{\lambda}) \frac{dz_b}{dx} \right] \\ &= -(z_u - Z')(\bar{\lambda} - \lambda_h) \frac{dz_u}{dx} + (Z' - z_b)(\lambda_b - \bar{\lambda}) \frac{dz_b}{dx} < 0, \end{aligned} \quad (4.84)$$

which concludes the argument since both terms in equation (4.84) are less than zero.

4.7.2. Porosity

Now we address the porosity case. Since porosity affects the equations through bulk density terms, equivalent statements to those for porosity in inequalities (4.72) are

$$\frac{\partial \rho}{\partial z} < 0, \quad \text{and} \quad \frac{d\bar{\rho}}{dx} > 0,$$

with $\rho(x, z_u)$ a constant. Then we must show that

$$\begin{aligned} \frac{d}{dx} [\psi_\phi - \bar{\psi}_\phi] &= \frac{d}{dx} \left[\Lambda \int_{z_b}^{z_u} \left(\int_z^{z_u} \rho(x, z') dz' \right) dz - \Lambda \int_{z_b}^{z_u} \left(\int_z^{z_u} \bar{\rho}(x) dz' \right) dz \right] \\ &= \Lambda \frac{d}{dx} \left[\int_{z_b}^{z_u} \left(\int_z^{z_u} g_\rho(x, z') dz' \right) dz \right] \\ &= \Lambda \frac{d}{dx} \left[\int_{z_b}^{z_u} G(x, z) dz \right] < 0, \end{aligned} \quad (4.85)$$

where $g_\rho(x, z) = \rho(x, z) - \bar{\rho}(x)$. The proof is accomplished by the following statements: since 1) $G(x, z)$ is a convex function of z that 2) is always less than zero with 3) a minimum value that decreases with x , then the lateral gradient of the integral in

equation (4.85) is less than zero because the thickness interval $[z_b, z_u]$ increases with x .

First, note that $\partial g_\rho / \partial z < 0$ and $g_\rho(x, z_u) < 0$. Then since $\bar{g}_\rho = 0$ we have

$$G(x, z) \equiv \int_z^{z_u} g_\rho(x, z') dz' \leq \int_{z_b}^{z_u} g_\rho(x, z) dz = 0. \quad (4.86)$$

Second because $G(x, z_u) = G(x, z_b) = 0$ and $G < 0$ over the interval (z_b, z_u) , then G will take on its minimum value at some depth z'' , where $g_\rho(x, z'') = \bar{g}_\rho = 0$. The minimum of G then changes with x as

$$\left. \frac{dG}{dx} \right|_{z''} = \frac{d}{dx} \int_{z''}^{z_u} g_\rho(x, z) dz = g_\rho(x, z_u) \frac{dz_u}{dx} - g_\rho(x, z'') \frac{dz''}{dx} + \int_{z''}^{z_u} \frac{\partial g_\rho}{\partial x} dz < 0. \quad (4.87)$$

Clearly the first term in the above equation is less than zero and the second term is equal to zero. The third term is also less than zero. This can be seen by noting that we have required $d\bar{\rho}/dx > 0$ and $d\rho_0/dx = 0$. Then since $\rho(x, z)$ is a smoothly increasing function of depth (i.e. smoothly decreasing with z), $\partial g_\rho / \partial x \leq 0$ over the interval $[z'', z_u]$ and inequalities (4.87) and (4.85) are true.

4.7.3. Friction Coefficient

Finally, we address the friction coefficient case. Here we must show

$$\begin{aligned} \frac{d}{dx} [\psi_\mu - \bar{\psi}_\mu] = \bar{\rho} \frac{d}{dx} \left\{ \int_{z_b}^{z_u} \left[1 + 2(1 - \lambda) \frac{\sin \theta}{(1 - \sin \theta)} \right] (z_u - z) dz \right. \\ \left. - \int_{z_b}^{z_u} \left[1 + 2(1 - \lambda) \frac{\sin \bar{\theta}}{(1 - \sin \bar{\theta})} \right] (z_u - z) dz \right\} < 0, \quad (4.88) \end{aligned}$$

which becomes

$$\begin{aligned} \frac{d}{dx}[\psi_\mu - \bar{\psi}_\mu] &= 2\rho(1 - \lambda) \frac{d}{dx} \left\{ \int_{z_b}^{z_u} (z_u - z) \left[\frac{\mu}{(\mu^2 + 1)^{1/2} - \mu} - \frac{\bar{\mu}}{(\bar{\mu}^2 + 1)^{1/2} - \bar{\mu}} \right] dz \right\}, \\ &= 2\rho(1 - \lambda) \frac{d}{dx} \left\{ \int_{z_b}^{z_u} (z_u - z) g_\mu(x, z) dz \right\} = 2\rho(1 - \lambda) \frac{dI_\mu}{dx} < 0, \end{aligned} \quad (4.89)$$

where we have used the definition of the friction angle $\theta = \tan^{-1} \mu$, as well as the relation

$$\tan^{-1} x = \sin^{-1} \left(\frac{x}{\sqrt{x^2 + 1}} \right), \quad (4.90)$$

and defined

$$g_\mu(x, z) = \frac{\mu}{(\mu^2 + 1)^{1/2} - \mu} - \frac{\bar{\mu}}{(\bar{\mu}^2 + 1)^{1/2} - \bar{\mu}}. \quad (4.91)$$

Equation (4.91) has the same form as equation (4.78), and our argument for the friction case follows along the same lines as that for the pore pressure ratio case.

It suffices to show $dI_\mu/dx < 0$. Applying the Liebnez integration rule and using the mean value theorem yields

$$\begin{aligned} \frac{dI_\mu}{dx} &= -H g_\mu(x, z_b) \frac{dz_b}{dx} + \frac{dz_u}{dx} \int_{z_b}^{z_u} g_\mu(x, z) dz + \int_{z_b}^{z_u} (z_u - z) \frac{\partial g_\mu}{\partial x} dz \\ &= -H g_\mu(x, z_b) \frac{dz_b}{dx} + H \bar{g}_\mu \frac{dz_u}{dx} + (z_u - Z') \int_{z_b}^{z_u} \frac{\partial g_\mu}{\partial x} dz, \end{aligned} \quad (4.92)$$

where

$$\begin{aligned}
\bar{g}_\mu &= \frac{1}{H} \int_{z_b}^{z_u} \left[\frac{\mu}{(\mu^2 + 1)^{1/2} - \mu} - \frac{\bar{\mu}}{(\bar{\mu}^2 + 1)^{1/2} - \bar{\mu}} \right] dz , \\
&= \frac{1}{H} \int_{z_b}^{z_u} \frac{\mu}{(\mu^2 + 1)^{1/2} - \mu} dz - \frac{\bar{\mu}}{(\bar{\mu}^2 + 1)^{1/2} - \bar{\mu}} \\
&= \overline{f(\mu)} - f(\bar{\mu}) > 0 , \tag{4.93}
\end{aligned}$$

and where we have defined

$$f(\mu) = \frac{\mu}{(\mu^2 + 1)^{1/2} - \mu} . \tag{4.94}$$

Inequality (4.93) comes from application of Jensen's inequality, and relies on the fact that $f(\mu)$ is a convex function of μ (*Hardy et al.*, 1952).

We proceed in an analogous fashion to the pore pressure ratio case and arrive at

$$\int_{z_b}^{z_u} \frac{\partial g_\mu}{\partial x} dz = (\bar{f} - f_u) \frac{dz_u}{dx} + (f_b - \bar{f}) \frac{dz_b}{dx} . \tag{4.95}$$

where f_u and f_b correspond to the function $f(\mu)$ evaluated at $\mu(x, z_u)$ and $\mu(x, z_b)$ respectively. Inserting equations (4.93), (4.94), and (4.95) into equation (4.92) yields

$$\begin{aligned}
\frac{dI_\mu}{dx} &= (z_u - z_b) \left[(\bar{f} - f_b) \frac{dz_b}{dx} + (\bar{f} - f(\bar{\mu})) \frac{dz_u}{dx} \right] + (z_u - Z') \left[(\bar{f} - f_u) \frac{dz_u}{dx} + (f_b - \bar{f}) \frac{dz_b}{dx} \right] \\
&= (Z' - z_b)(\bar{f} - f_b) \frac{dz_b}{dx} + [(z_u - z_b)(\bar{f} - f(\bar{\mu})) + (z_u - Z')(\bar{f} - f_u)] \frac{dz_u}{dx} < 0 . \tag{4.96}
\end{aligned}$$

Inequality (4.96) can be rewritten as

$$(z_u - z_b)(\bar{f} - f(\bar{\mu}))\frac{dz_u}{dx} < (Z' - z_b)(f_b - \bar{f})\frac{dz_b}{dx} + (z_u - Z')(f_u - \bar{f})\frac{dz_u}{dx}, \quad (4.97)$$

where the LHS and both terms on the RHS are greater than zero, since $f(\mu)$ is an increasing function of μ , and we have assumed $\partial\mu/\partial z > 0$. Thus, we can state two conditions that will make inequality (4.96) true. First we have

$$(z_u - z_b)(\bar{f} - f(\bar{\mu}))\frac{dz_u}{dx} < (z_u - Z')(f_u - \bar{f})\frac{dz_u}{dx}$$

$$\frac{\bar{f} - f(\bar{\mu})}{f_u - \bar{f}} < \frac{z_u - Z'}{z_u - z_b} < 1. \quad (4.98)$$

And second we have

$$(z_u - z_b)(\bar{f} - f(\bar{\mu}))\frac{dz_u}{dx} < (Z' - z_b)(f_b - \bar{f})\frac{dz_b}{dx},$$

$$\frac{(\bar{f} - f(\bar{\mu}))\frac{dz_u}{dx}}{(\bar{f} - f_b)\frac{dz_b}{dx}} + 1 < \frac{z_u - Z'}{z_u - z_b} < 1, \quad (4.99)$$

where we have added and subtracted the term $z_u(\bar{f} - f_b)dz_b/dx$ to arrive at inequality (4.99). If either inequalities (4.98) and (4.99) are true then inequality (4.96) will be as well. However, if both inequalities (4.98) and (4.99) are false, it is still possible that inequality (4.96) is true. The inequalities can be straightforwardly checked for a given functional form of $\mu(x, z)$. It is easy to show that inequality (4.96) is true when $\mu(x, z)$ decreases linearly with depth, and in a subsequent paper we will also show that it is true when $\mu(x, z)$ decreases exponentially with depth.

CHAPTER V

CONCLUSION

This dissertation is concerned with the mechanics of slow slip and tremor in subduction zones. Chapter II focuses on heterogeneous frictional controls on the generation and propagation of slow sliding transients. This model is motivated by geologic observations indicating that shear at the plate interface in the slow slip zone is distributed over broad zones ($\sim 10\text{--}10^3$ m) composed of rocks with marked differences in mechanical properties. Chapter III makes further use of this concept to examine the conditions that lead to the generation and maintenance of large fluid pressures in the slow slip zone. While Chapters II and III detail the mechanics of slow slip located down-dip of the seismogenically locked zone, Chapter IV looks at the mechanics of submarine accretionary prisms, where slow slip and tremor can occur up-dip of the locked zone.

In Chapter II, I present a model for quasi-dynamic rupture along faults composed of material mixtures characterized by different rate-and-state-dependent frictional properties to determine the parameter regime capable of producing slow slip in an idealized subduction zone setting. Keeping other parameters fixed, the relative proportions of velocity-weakening (VW) and velocity-strengthening (VS) materials control the sliding character (stable, slow, or dynamic) along the fault. The stability boundary between slow and dynamic is accurately described by linear analysis of a double spring-slider system with VW and VS blocks. The results place bounds on the volume fractions of VW material present in heterogeneous geological assemblages that host slow slip and tremor in subduction zones.

In Chapter III, I model the compaction of low porosity material subducting through the slow slip and tremor zone in the presence of pressure and temperature-dependent dehydration reactions. Pore pressures in excess of lithostatic values are a robust feature of simulations that employ parameters consistent with the geometry of the Cascadia subduction margin, and bulk permeabilities in the range $10^{-25} \leq k \leq 10^{-23} \text{ m}^2$. In these calculations, the dehydration fluid source is parameterized using the predictions of previous studies that have calculated the amount of bound H_2O lost from subducting oceanic crust as a result of a generalized basalt dehydration reaction. We also report the predictions of simulations that include a viscous component to deformation and dehydration of antigorite serpentinite through a nonlinear kinetic law. Simulations that include viscous deformation uniformly generate traveling porosity waves that transport increased fluid pressures within the slow slip region. Our results indicate that processes must be active in the slow slip region of subduction zones that are responsible, perhaps periodically, for alleviating excess pore pressures generated by dehydration reactions. Candidate mechanisms include hydraulic fracturing within or below the plate interface, lateral and/or focused fluid migration, or increases in permeability during slow slip events.

In Chapter IV, I consider the mechanics of submarine accretionary wedges, and in particular examine how spatial variations in pore pressure, porosity, and internal friction coefficient affect predictions of basal shear stress, taper angle, and internal slip surface geometry. Compared to wedges with depth-averaged parameter values, the basal shear stress will be lower or the taper angle will be larger if: i) the pore pressure ratio increases monotonically with depth, ii) the porosity decreases monotonically with depth, or iii) the internal friction coefficient decreases monotonically with depth. The first two conditions can be considered first-order descriptions of many natural

settings. To illustrate their effects I consider two specific functional forms: a linear increase in the pore pressure ratio, and an exponential decrease in porosity with depth. The results suggest that assuming an average porosity throughout the wedge may be a good approximation in many cases, but assuming an average value for the pore pressure ratio can cause significant errors. Because of their large affect on calculations made with Coulomb wedge theories, spatial variations in pore pressure should be accounted for whenever possible.

The unifying thread of the chapters contained here has been the effort to develop theories of slow slip and tremor from a geologic perspective. In addition to the inherent scientific merit of studying the mechanics of subduction zone plate boundaries, there is also the potential for societal benefit. The world's largest earthquakes occur at subduction zones, and there is still much to be learned about the mechanisms that lead to these events.

REFERENCES CITED

- Ague, J. J., J. Park, and D. M. Rye (1998), Regional metamorphic dehydration and seismic hazard, *Geophys. Res. Lett.*, *25*(22), 4221–4224, doi:10.1029/1998GL900124.
- Ampuero, J.-P., and A. M. Rubin (2008), Earthquake nucleation on rate and state faults - Aging and slip laws, *J. Geophys. Res.*, *113*, B01302, doi:10.1029/2007JB005082.
- Ando, M., Y. Tu, H. Kumagai, Y. Yamanaka, and C.-H. Lin (2012), Very low frequency earthquakes along the ryukyu subduction zone, *Geophys. Res. Lett.*, *39*(4), doi:10.1029/2011GL050559, 104303.
- Ando, R., R. Nakata, and T. Hori (2010), A slip pulse model with fault heterogeneity for low-frequency earthquakes and tremor along plate interfaces, *Geophys. Res. Lett.*, *37*, L10310, doi:10.1029/2010GL043056.
- Audet, P., M. G. Bostock, N. I. Christensen, and S. M. Peacock (2009), Seismic evidence for overpressured subducted oceanic crust and megathrust fault sealing, *Nature*, *457*(7678), doi:10.1038/nature07650.
- Audet, P., M. G. Bostock, D. C. Boyarko, M. R. Brudzinski, and R. M. Allen (2010), Slab morphology in the cascadia fore arc and its relation to episodic tremor and slip, *J. Geophys. Res.*, *115*(B4), doi:10.1029/2008JB006053.
- Bangs, N. L., G. K. Westbrook, J. W. Ladd, and P. Buhl (1990), Seismic velocities from the Barbados Ridge Complex: Indicators of high pore fluid pressures in an accretionary complex, *J. Geophys. Res.*, *95*(B6), 8767–8782, doi:10.1029/JB095iB06p08767.
- Barcilon, V., and F. M. Richter (1986), Nonlinear waves in compacting media, *Journal of Fluid Mechanics*, *164*, 429–448, doi:10.1017/S0022112086002628.
- Barker, D. H. N., R. Sutherland, S. Henrys, and S. Bannister (2009), Geometry of the Hikurangi subduction thrust and upper plate, North Island, New Zealand, *Geochem. Geophys. Geosys.*, *10*(2), Q02007, doi:10.1029/2008GC002153.
- Bartlow, N. M., S. Miyazaki, A. M. Bradley, and P. Segall (2011), Space-time correlation of slip and tremor during the 2009 Cascadia slow slip event, *Geophys. Res. Lett.*, *38*, L18309, doi:10.1029/2011GL048714.

- Bebout, G. E., and M. D. Barton (2002), Tectonic and metasomatic mixing in a high-t subduction zone melange: Insights into the geochemical evolution of the slab-mantle interface, *Chemical Geology*, 187, 79–106, doi:10.1016/S0009-2541(02)00019-0.
- Behrmann, J. H., and A. Kopf (1993), Textures and microfabrics in fine-grained muds and mudstones from Site 808, Nankai accretionary prism, *Proc. Ocean Drill. Program Sci. Results*, 131, 45–55.
- Bekins, B. A., and S. J. Dreiss (1992), A simplified analysis of parameters controlling dewatering in accretionary prisms, *Earth Planet. Sci. Lett.*, 109(3–4), 275 – 287, doi:http://dx.doi.org/10.1016/0012-821X(92)90092-A.
- Bercovici, D., and Y. Ricard (2003), Energetics of a two-phase model of lithospheric damage, shear localization and plate-boundary formation, *Geophys. J. Int.*, 152(3), 581–596, doi:10.1046/j.1365-246X.2003.01854.x.
- Beroza, G. C., and S. Ide (2011), Slow earthquakes and nonvolcanic tremor, *Annual Review of Earth and Planetary Sciences*, 39(1), 271–296, doi:10.1146/annurev-earth-040809-152531.
- Blake, M. C. J., D. E. Moore, and A. S. Jayko (1995), The role of serpentinite melanges in the unroofing of uhp rocks: An example from the western alps of italy, in *Ultrahigh Pressure Metamorphism*, edited by R. G. Coleman and X. Wang, pp. 182–205, Cambridge University Press.
- Blanco-Quintero, I., J. A. P. Fernández, A. G. Casco, E. Tauler, et al. (2011), Serpentinites and serpentinites within a fossil subduction channel: La corea mélange, eastern Cuba, *Geologica Acta*, 9(3).
- Brace, W. F. (1977), Permeability from resistivity and pore shape, *J. Geophys. Res.*, 82(23), 3343–3349, doi:10.1029/JB082i023p03343.
- Brantut, N., J. Sulem, and A. Schubnel (2011), Effect of dehydration reactions on earthquake nucleation: Stable sliding, slow transients, and unstable slip, *J. Geophys. Res.*, 116(B5), doi:10.1029/2010JB007876, b05304.
- Bray, C. J., and D. E. Karig (1985), Porosity of sediments in accretionary prisms and some implications for dewatering processes, *J. Geophys. Res.*, 90(B1), 768–778, doi:10.1029/JB090iB01p00768.
- Breeding, C. M., J. J. Ague, M. Brocker, and E. W. Bolton (2003), Blueschist preservation in a retrograded, high-pressure, low-temperature metamorphic terrane, Tinos, Greece: Implications for fluid flow paths in subduction zones, *Geochem., Geophys., Geosys.*, 4(1), doi:10.1029/2002GC000380, 9002.

- Breen, N. A., and D. L. Orange (1992), The effects of fluid escape on accretionary wedges 1. Variable porosity and wedge convexity, *J. Geophys. Res.*, *97*(B6), 9265–9275, doi:10.1029/91JB02767.
- Burgette, R. J., R. J. Weldon, and D. A. Schmidt (2009), Interseismic uplift rates for western oregon and along-strike variation in locking on the cascadia subduction zone, *J. Geophys. Res.*, *114*(B1), doi:10.1029/2008JB005679.
- Calahorrano, A. B., V. SallarAls, J.-Y. Collot, F. Sage, and C. R. Ranero (2008), Nonlinear variations of the physical properties along the southern Ecuador subduction channel: Results from depth-migrated seismic data, *Earth Planet. Sci. Lett.*, *267*(3–4), 453 – 467, doi:http://dx.doi.org/10.1016/j.epsl.2007.11.061.
- Cloos, M. (1986), Blueschists in the franciscan complex of california: Petrotectonic constraints on uplift mechanisms, *Geological Society of America Memoirs*, *164*, 77–94, doi:10.1130/MEM164-p77.
- Cloos, M., and R. L. Shreve (1988), Subduction-channel model of prism accretion, melange formation, sediment subduction, and subduction erosion at convergent plate margins: 1. Background description, *Pure. Appl. Geophys.*, *128*, 501–545.
- Collettini, C. (2011), The mechanical paradox of low-angle normal faults: Current understanding and open questions, *Tectonophysics*, *510*(3–4), 253 – 268, doi:http://dx.doi.org/10.1016/j.tecto.2011.07.015.
- Collettini, C., A. Niemeijer, C. Viti, S. A. F. Smith, and C. Marone (2011), Fault structure, frictional properties and mixed-mode fault slip behavior, *Earth Plan. Sci. Lett.*, *311*(3–4), 316–327, doi:10.1016/j.epsl.2011.09.020.
- Connolly, J., and Y. Podladchikov (1998), Compaction-driven fluid flow in viscoelastic rock, *Geodinamica Acta*, *11*(2–3), 55–84, doi:http://dx.doi.org/10.1016/S0985-3111(98)80006-5.
- Connolly, J. A. D. (1997), Devolatilization-generated fluid pressure and deformation-propagated fluid flow during prograde regional metamorphism, *J. Geophys. Res.*, *102*(B8), 18,149–18,173, doi:10.1029/97JB00731.
- Cuffey, K., and W. S. B. Paterson (2010), *The Physics of Glaciers*, 4th ed., Academic Press, Amsterdam.
- Dahlen, F. A. (1990), Critical taper model of fold-and-thrust belts and accretionary wedges, *Annu. Rev. Earth Planet. Sci.*, *18*, 55–99, doi:10.1146/annurev.ea.18.050190.000415.
- Dahlen, F. A. (1992), Metamorphism of nonhydrostatically stressed rocks, *Am. J. Sci.*, *292*(3), 184–198, doi:10.2475/ajs.292.3.184.

- Dahlen, F. A., and J. Suppe (1984), Mechanics of fold-and-thrust belts and accretionary wedges: Cohesive Coulomb theory, *J. Geophys. Res.*, *89*(B12), 10,087–10,101, doi:10.1029/JB089iB12p10087.
- Daub, E. G., D. R. Shelly, R. A. Guyer, and P. A. Johnson (2011), Brittle and ductile friction and the physics of tectonic tremor, *Geophys. Res. Lett.*, *38*, L10301, doi:10.1029/2011GL046866.
- Davis, D., J. Suppe, and F. A. Dahlen (1984), Mechanics of fold-and-thrust belts and accretionary wedges, *J. Geophys. Res.*, *88*(B2), 1153–1172, doi:10.1029/JB088iB02p01153.
- Davis, E. E., and R. D. Hyndman (1989), Accretion and recent deformation of sediments along the northern Cascadia subduction zone, *Geol. Soc. Am. Bull.*, *101*(11), 1465–1480, doi:10.1130/0016-7606(1989)101<1465:AARDOS>2.3.CO;2.
- Dieterich, J. H. (1992), Earthquake nucleation on faults with rate- and state-dependent strength, *Tectonophysics*, *211*(1-4), 115–134, doi:10.1016/0040-1951(92)90055-B.
- Dimanov, A., and G. Dresen (2005), Rheology of synthetic anorthite-diopside aggregates: Implications for ductile shear zones, *J. Geophys. Res.*, *110*, B07293, doi:10.1029/2004JB003431.
- Eberhart-Phillips, D., and M. Reyners (1999), Plate interface properties in the northeast Hikurangi subduction zone, New Zealand, from converted seismic waves, *Geophys. Res. Lett.*, *26*, 2565–2568.
- Ellis, S. M., Å. Fagereng, D. M. Saffer, D. H. Barker, S. A. Henrys, C. A. Williams, L. Wallace, and S. J. Buiter (2013), Fluid budgets along the northern Hikurangi subduction margin, New Zealand: the effect of a subducting seamount on fluid pressure, Abstract T43E-2707, AGU Fall Meeting, 2013.
- Engquist, B., and A. Majda (1977), Absorbing boundary conditions for numerical simulation of waves, *Proceedings of the National Academy of Sciences*, *74*(5), 1765–1766.
- Escartín, J., G. Hirth, and B. Evans (1997), Nondilatant brittle deformation of serpentinites: Implications for Mohr-Coulomb theory and the strength of faults, *J. Geophys. Res.*, *102*(B2), 2897–2913, doi:10.1029/96JB02792.
- Escartín, J., G. Hirth, and B. Evans (2001), Strength of slightly serpentinitized peridotites: Implications for the tectonics of oceanic lithosphere, *Geology*, *29*(11), 1023–1026, doi:10.1130/0091-7613(2001)029<1023:SOSSPI>2.0.CO;2.

- Fagereng, Å. (2011), Frequency-size distribution of competent lenses in a block-in-matrix mélange: Imposed length scales of brittle deformation?, *J. Geophys. Res.*, *116*, B05302, doi:10.1029/2010JB007775.
- Fagereng, Å., and J. F. Diener (2011), Non-volcanic tremor and discontinuous slab dehydration, *Geophys. Res. Lett.*, *38*(15).
- Fagereng, Å., and R. H. Sibson (2010), Mélange rheology and seismic style, *Geology*, *38*(8), doi:10.1130/G30868.1.
- Fagereng, Å., F. Remitti, and R. H. Sibson (2011), Incrementally developed slickenfibers - Geological record of repeating low stress-drop seismic events?, *Tectonophysics*, *510*(3-4), doi:10.1016/j.tecto.2011.08.015.
- Ferris, A., G. A. Abers, D. H. Christensen, and E. Veenstra (2003), High resolution image of the subducted Pacific (?) plate beneath central Alaska, 50–150 km depth, *Earth Planet. Sci. Lett.*, *214*(3-4), 575 – 588, doi:http://dx.doi.org/10.1016/S0012-821X(03)00403-5.
- Fletcher, R. C. (1989), Approximate analytical solutions for a cohesive fold-and-thrust wedge: Some results for lateral variation in wedge properties and for finite wedge angle, *J. Geophys. Res.*, *94*(B8), 10,347–10,354, doi:10.1029/JB094iB08p10347.
- Flueh, E. R., M. A. Fisher, J. Bialas, J. R. Childs, D. Klaeschen, N. Kukowski, T. Parsons, D. W. Scholl, U. t. Brink, A. M. Trehu, and N. Vidal (1998), New seismic images of the Cascadia subduction zone from cruise SO108 - ORWELL, *Tectonophysics*, *293*(1-2), 69–84, doi:10.1016/S0040-1951(98)00091-2.
- Gao, H., D. A. Schmidt, and R. J. Weldon (2012), Scaling relationships of source parameters for slow slip events, *Bull. Seismol. Soc. Am.*, *102*, 352–360, doi:10.1785/0120110096.
- Gerya, T. V., B. Stöckhert, and A. L. Perchuk (2002), Exhumation of high-pressure metamorphic rocks in a subduction channel: A numerical simulation, *Tectonics*, *21*(6), 6–1–6–19, doi:10.1029/2002TC001406.
- Ghosh, A., J. E. Vidale, J. R. Sweet, K. C. Creager, A. G. Wech, and H. Houston (2010), Rapid, continuous streaking of tremor in Cascadia, *Geochem. Geophys. Geosyst.*, *11*, Q12010, doi:10.1029/2010GC003305.
- Guillot, S., K. Hattori, P. Agard, S. Schwartz, and O. Vidal (2009), Exhumation processes in oceanic and continental subduction contexts: A review, in *Subduction Zone Geodynamics*, edited by S. Lallemand and F. Funiciello, Frontiers in Earth Sciences, pp. 175–205, Springer Berlin Heidelberg, doi:10.1007/978-3-540-87974-9_10.

- Hacker, B. R., G. A. Abers, and S. M. Peacock (2003), Subduction factory 1. theoretical mineralogy, densities, seismic wave speeds, and h₂o contents, *J. Geophys. Res.*, *108*(B1), doi:10.1029/2001JB001127.
- Hansen, R. T., M. G. Bostock, and N. I. Christensen (2012), Nature of the low velocity zone in Cascadia from receiver function waveform inversion, *Earth Planet. Sci. Lett.*, *337-338*(0), 25 – 38, doi:http://dx.doi.org/10.1016/j.epsl.2012.05.031.
- Hardy, G. H., J. E. Littlewood, and G. Polya (1952), *Inequalities*, Cambridge University Press, Cambridge.
- Henry, P., L. Jouniaux, E. J. Screaton, S. Hunze, and D. M. Saffer (2003), Anisotropy of electrical conductivity record of initial strain at the toe of the nankai accretionary wedge, *J. Geophys. Res.*, *108*(B9), doi:10.1029/2002JB002287.
- Hermann, J., O. Muntener, and M. Scambelluri (2000), The importance of serpentinite mylonites for subduction and exhumation of oceanic crust, *Tectonophysics*, *327*(3-4), 225 – 238, doi:http://dx.doi.org/10.1016/S0040-1951(00)00171-2.
- Hilaret, N., and B. Reynard (2009), Stability and dynamics of serpentinite layer in subduction zone, *Tectonophysics*, *465*(1-4), 24 – 29, doi:http://dx.doi.org/10.1016/j.tecto.2008.10.005.
- Hilaret, N., B. Reynard, Y. Wang, I. Daniel, S. Merkel, N. Nishiyama, and S. Petitgirard (2007), High-pressure creep of serpentine, interseismic deformation, and initiation of subduction, *Science*, *318*(5858), 1910–1913, doi:10.1126/science.1148494.
- Hirth, G., and J. Tullis (1992), Dislocation creep regimes in quartz aggregates, *J. Struct. Geol.*, *13*, 145–159.
- Housen, B. A., H. J. Tobin, P. Labaume, E. C. Leitch, A. J. Maltman, and the Ocean Drilling Program Leg 156 Shipboard Science Party (1996), Strain decoupling across the decollement of the barbados accretionary prism, *Geology*, *24*(2), 127–130, doi:10.1130/0091-7613(1996)024<0127:SDATDO>2.3.CO;2.
- Hyndman, R. D., and S. M. Peacock (2003), Serpentinization of the forearc mantle, *Earth Planet. Sci. Lett.*, *212*, 417–432, doi:10.1016/S0012-821X(03)00263-2.
- Ide, S., D. R. Shelly, and G. C. Beroza (2007), Mechanism of deep low frequency earthquakes: Further evidence that deep non-volcanic tremor is generated by shear slip on the plate interface, *Geophys. Res. Lett.*, *34*, L03308, doi:10.1029/2006GL028890.

- Ito, Y., and K. Obara (2006a), Very low frequency earthquakes within accretionary prisms are very low stress-drop earthquakes, *Geophys. Res. Lett.*, *33*, L09302, doi:10.1029/2006GL025883.
- Ito, Y., and K. Obara (2006b), Dynamic deformation of the accretionary prism excites very low frequency earthquakes, *Geophys. Res. Lett.*, *33*(2), doi:10.1029/2005GL025270, 102311.
- Ito, Y., R. Hino, M. Kido, H. Fujimoto, Y. Osada, D. Inazu, Y. Ohta, T. Iinuma, M. Ohzono, S. Miura, et al. (2013), Episodic slow slip events in the Japan subduction zone before the 2011 Tohoku–Oki earthquake, *Tectonophysics*, *600*, 14–26.
- Jaeger, J. C., and N. G. W. Cook (1969), *Fundamentals of Rock Mechanics*, 87-91 pp., Methuen, London.
- Johnson, J. W., E. H. Oelkers, and H. C. Helgeson (1992), Supcrt92: A software package for calculating the standard molal thermodynamic properties of minerals, gases, aqueous species, and reactions from 1 to 5000 bar and 0 to 1000°C, *Comput. Geosci.*, *18*(7), 899 – 947, doi:http://dx.doi.org/10.1016/0098-3004(92)90029-Q.
- Katayama, I., T. Terada, K. Okazaki, and W. Tanikawa (2012), Episodic tremor and slow slip potentially linked to permeability contrasts at the Moho, *Nat. Geosci.*, *5*(10), 731–734, doi:10.1038/ngeo1559.
- Kato, A., T. Iidaka, R. Ikuta, Y. Yoshida, K. Katsumata, T. Iwasaki, S. Sakai, C. Thurber, N. Tsumura, K. Yamaoka, T. Watanabe, T. Kunitomo, F. Yamazaki, M. Okubo, S. Suzuki, and N. Hirata (2010), Variations of fluid pressure within the subducting oceanic crust and slow earthquakes, *Geophys. Res. Lett.*, *37*(14), doi:10.1029/2010GL043723, 114310.
- Kawakatsu, H., and S. Watada (2007), Seismic evidence for deep-water transportation in the mantle, *Science*, *316*(5830), 1468–1471, doi:10.1126/science.1140855.
- Kawano, S., I. Katayama, and K. Okazaki (2011), Permeability anisotropy of serpentinite and fluid pathways in a subduction zone, *Geology*, *39*(10), 939–942, doi:10.1130/G32173.1.
- Kitajima, H., and D. Saffer (2014), Quantification of in situ stress and pore pressure in the Nankai subduction zone: Effects of lithology and loading path, Abstract T43D-03, AGU Fall Meeting, 2014.

- Kitajima, H., and D. M. Saffer (2012), Elevated pore pressure and anomalously low stress in regions of low frequency earthquakes along the Nankai Trough subduction megathrust, *Geophys. Res. Lett.*, *39*(23), doi:10.1029/2012GL053793.
- Kitamura, M., H. Kitajima, P. Henry, R. Valdez, M. Josh, H. Tobin, D. Saffer, T. Hirose, S. Toczko, and L. Maeda (2014), Physical properties of the Nankai inner accretionary prism sediments at Site C0002, IODP Expedition 348, Abstract T51A-4574, AGU Fall Meeting, 2014.
- Kodiara, S., T. Iidaka, A. Kato, J. Park, T. Iwasaki, and Y. Kaneda (2004), High pore fluid pressure may cause silent slip in the Nankai Trough, *Science*, *304*(5675), 1295–1298, doi:10.1126/science.1096535.
- Lallemand, S. E., P. Schnurle, and J. Malavieille (1994), Coulomb theory applied to accretionary and nonaccretionary wedges: Possible causes for tectonic erosion and/or frontal accretion, *J. Geophys. Res.*, *99*(B6), 12,033–12,055, doi:10.1029/94JB00124.
- Lasaga, A. C., and D. M. Rye (1993), Fluid flow and chemical reaction kinetics in metamorphic systems, *Am. J. Sci.*, *293*, 361–361.
- Li, X., G. Bock, A. Vafidis, R. Kind, H.-P. Harjes, W. Hanka, K. Wylegalla, M. Van Der Meijde, and X. Yuan (2003), Receiver function study of the Hellenic subduction zone: imaging crustal thickness variations and the oceanic Moho of the descending African lithosphere, *Geophys. J. Int.*, *155*(2), 733–748, doi:10.1046/j.1365-246X.2003.02100.x.
- Liu, Y., and J. R. Rice (2005), Aseismic slip transients emerge spontaneously in three-dimensional rate and state modeling of subduction earthquake sequences, *J. Geophys. Res.*, *110*, B08307, doi:10.1029/2004JB003424.
- Liu, Y., and J. R. Rice (2007), Spontaneous and triggered aseismic deformation transients in a subduction fault model, *J. Geophys. Res.*, *112*, B09404, doi:10.1029/2007jb004930.
- Liu, Y., and A. M. Rubin (2010), Role of fault gouge dilatancy on aseismic deformation transients, *J. Geophys. Res.*, *115*, B10414, doi:10.1029/2010JB007522.
- Lowry, A. R. (2006), Resonant slow fault slip in subduction zones forced by climatic load stress, *Nature*, *442*(7104), 802–805.
- Malvern, L. E. (1977), *Introduction to the Mechanics of a Continuous Medium*, Prentice-Hall.

- Martin, S., and A. Rietbrock (2006), Guided waves at subduction zones: Dependencies on slab geometry, receiver locations, and earthquake sources, *Geophys. J. Int.*, *167*, 693–704.
- Matsubara, M., K. Obara, and K. Kasahara (2009), High- V_P/V_S zone accompanying non-volcanic tremors and slow-slip events beneath southwestern Japan, *Tectonophysics*, *472*(1-4), 6–17, doi:10.1016/j.tecto.2008.06.013.
- McKenzie, D. (1984), The generation and compaction of partially molten rock, *Journal of Petrology*, *25*(3), 713–765, doi:10.1093/petrology/25.3.713.
- Mehl, L., and G. Hirth (2008), Plagioclase preferred orientation in layered mylonites: Evaluation of flow laws for the lower crust, *J. Geophys. Res.*, *113*, B05202, doi:10.1029/2007JB005075.
- Meneghini, F., M. Marroni, J. C. Moore, L. Pandolfi, and C. D. Rowe (2009), The process of underthrusting and underplating in the geologic record: Structural diversity between the Franciscan Complex (California), the Kodiak Complex (Alaska), and the Internal Ligurian Units (Italy), *Geol. J.*, *44*, 126–152, doi:10.1002/gj.1144.
- Moore, G. F., A. Taira, N. L. Bangs, S. Kuramoto, T. H. Shipley, C. M. Alex, S. S. Gulick, D. J. Hills, T. Ike, S. Ito, S. C. Leslie, A. J. McCutcheon, K. Mochizuki, S. Morita, Y. Nakamura, J. O. Park, B. L. Taylor, G. Toyama, H. Yagi, and Z. Zhao (2001), Data report: Structural setting of the Leg 190 Muroto Transect, *Proc. Ocean Drill. Program Init. Rep.*, *190*, 1–14.
- Moore, G. F., J. O. Park, N. L. Bangs, S. P. Gulick, H. J. Tobin, Y. Nakamura, S. Stao, T. Tsuji, T. Yoro, H. Tanaka, S. Uraki, K. Y. Y. Sanada, S. Kuramoto, and A. Taira (2009), Structural and seismic framework of the NanTroSEIZE Stage 1 transect, in *Proceedings of the Integrated Ocean Drilling Program*, vol. 314/315/316, edited by M. Kinoshita, H. Tobin, J. Ashi, G. Kimura, S. Lallement, E. J. Screaton, D. Curewitz, H. Masago, K. T. Moe, and the Expedition 314/315/316 Scientists, Integrated Ocean Drilling Program Management International, Inc., Washington D. C., doi:10.2204/iodp.proc.314315316.102.2009.
- Moore, G. F., D. Saffer, M. Studer, and P. Costa Pisani (2011), Structural restoration of thrusts at the toe of the nankai trough accretionary prism off shikoku island, japan: Implications for dewatering processes, *Geochemistry, Geophysics, Geosystems*, *12*(5), doi:10.1029/2010GC003453.
- Moore, J. C., and T. Byrne (1987), Thickening of fault zones: A mechanism of melange formation in accreting sediments, *Geology*, *15*(11), 1040–1043, doi:10.1130/0091-7613(1987)15<1040:TOFZAM>2.0.CO;2.

- Moore, J. C., and H. Tobin (1997), Estimated fluid pressures of the Barbados accretionary prism and adjacent sediments, in *Proc. ODP, Sci. Results*, vol. 156, edited by T. H. Shipley, Y. Ogawa, P. Blum, and J. M. Bahr, pp. 229–238, College Station, TX (Ocean Drilling Program), doi:10.2973/odp.proc.sr.156.030.1997.
- Moore, J. C., and P. Vrolijk (1992), Fluids in accretionary prisms, *Reviews of Geophysics*, 30(2), 113–135, doi:10.1029/92RG00201.
- Nakata, R., R. Ando, T. Hori, and S. Ide (2011), Generation mechanism of slow earthquakes: Numerical analysis based on a dynamic model with brittle-ductile mixed fault heterogeneity, *J. Geophys. Res.*, 116, B08308, doi:10.1029/2010JB008188.
- Nakatani, M. (2001), Conceptual and physical clarification of rate and state friction: Frictional sliding as a thermally activated rheology, *J. Geophys. Res.*, 106(B7), 13,347–13,380, doi:10.1029/2000JB900453.
- Obara, K. (2002), Nonvolcanic deep tremor associated with subduction in southwest Japan, *Science*, 296(5573), 1679–1681, doi:10.1126/science.1070378.
- Obara, K. (2010), Phenomenology of deep slow earthquake family in southwest japan: Spatiotemporal characteristics and segmentation, *J. Geophys. Res.*, 115, B00A25, doi:10.1029/2008JB006048.
- Okazaki, K., I. Katayama, and H. Noda (2013), Shear-induced permeability anisotropy of simulated serpentinite gouge produced by triaxial deformation experiments, *Geophys. Res. Lett.*, 40(7), 1290–1294, doi:10.1002/grl.50302.
- Peacock, S. M. (2009), Thermal and metamorphic environment of subduction zone episodic tremor and slip, *J. Geophys. Res.*, 114(B8), doi:10.1029/2008JB005978.
- Peacock, S. M., N. I. Christensen, M. G. Bostock, and P. Audet (2011), High pore pressures and porosity at 35 km depth in the Cascadia subduction zone, *Geology*, doi:10.1130/G31649.1.
- Peng, Z., and J. Gomberg (2010), An integrated perspective of the continuum between earthquakes and slow-slip phenomena, *Nat. Geosci.*, 3(9), 599–607, doi:10.1038/ngeo940.
- Petersen, M., M. Moschetti, P. Powers, C. Mueller, K. Haller, A. Frankel, Y. Zeng, S. Rezaeian, S. Harmsen, O. Boyd, N. Field, R. Chen, K. Rukstales, N. Luco, R. Wheeler, R. Williams, and A. Olsen (2014), Documentation for the 2014 update of the United States national seismic hazard maps, *U.S. Geological Survey Open-File Report, 2014–1091*, 243p.

- Poulet, T., E. Veveakis, K. Regenauer-Lieb, and D. A. Yuen (2014), Thermo-poro-mechanics of chemically active creeping faults: 3. The role of serpentinite in episodic tremor and slip sequences, and transition to chaos, *J. Geophys. Res.*, *119*(6), 4606–4625, doi:10.1002/2014JB011004.
- Regenauer-Lieb, K., and D. Yuen (2008), Multiscale brittle-ductile coupling and genesis of slow earthquakes, *Pure Appl. Geophys.*, *165*(3-4), 523–543, doi:10.1007/s00024-008-0326-8.
- Reiner, M. (1964), The Deborah number, *Physics Today*, *17*(1), 62, doi:10.1063/1.3051374.
- Rice, J. R. (1993), Spatiotemporal complexity of slip on a fault, *J. Geophys. Res.*, *98*(B6), 9885–9907, doi:10.1029/93JB00191.
- Rice, J. R. (2006), Heating and weakening of faults during earthquake slip, *J. Geophys. Res.*, *111*, B05311, doi:10.1029/2005JB004006.
- Rice, J. R., and M. P. Cleary (1976), Some basic stress diffusion solutions for fluid-saturated elastic porous media with compressible constituents, *Reviews of Geophysics*, *14*(2), 227–241.
- Richter, F. M., and D. McKenzie (1986), Dynamic models for melt segregation from a deformable matrix, *J. Geol.*, *92*, 729–740.
- Rondenay, S., G. A. Abers, and P. E. van Keken (2008), Seismic imaging of subduction zone metamorphism, *Geology*, *36*(4), 275–278, doi:10.1130/G24112A.1.
- Rowe, K. T., E. J. Screaton, and S. Ge (2012), Coupled fluid flow and deformation modeling of the frontal thrust region of the kumano basin transect, japan: Implications for fluid pressures and decollement downstepping, *Geochem., Geophys., Geosys.*, *13*(3), doi:10.1029/2011GC003861.
- Royer, A. A., A. M. Thomas, and M. G. Bostock (2015), Tidal modulation and triggering of low-frequency earthquakes in northern Cascadia, *J. Geophys. Res.*, *120*(1), 384–405, doi:10.1002/2014JB011430, 2014JB011430.
- Rubin, A. M. (2008), Episodic slow slip events and rate-and-state friction, *J. Geophys. Res.*, *113*, B11414, doi:10.1029/1008JB005642.
- Rubin, A. M., and J.-P. Ampuero (2005), Earthquake nucleation on (ageing) rate and state faults, *J. Geophys. Res.*, *110*, B11312, doi:10.1029/2005JB003686.
- Rubinstein, J. L., J. E. Vidale, J. Gomberg, P. Bodin, K. C. Creager, and S. D. Malone (2007), Non-volcanic tremor driven by large transient shear stresses, *Nature*, *448*, 579–582, doi:10.1038/nature06017.

- Rubinstein, J. L., M. La Rocca, J. E. Vidale, K. C. Creager, and A. G. Wech (2008), Tidal modulation of nonvolcanic tremor, *Science*, *319*, 186–189, doi:10.1126/science.1150558.
- Ruina, A. (1983), Slip instability and state variable friction laws, *J. Geophys. Res.*, *88*, 10,359–10,370.
- Saffer, D. M. (2003), Pore pressure development and progressive dewatering in underthrust sediments at the Costa Rican subduction margin: Comparison with northern Barbados and Nankai, *J. Geophys. Res.*, *108*(B5), doi:10.1029/2002JB001787.
- Saffer, D. M., and B. A. Bekins (1998), Episodic fluid flow in the Nankai accretionary complex: Timescale, geochemistry, flow rates, and fluid budget, *J. Geophys. Res.*, *103*(B12), 30,351–30,370, doi:10.1029/98JB01983.
- Saffer, D. M., and B. A. Bekins (2006), An evaluation of factors influencing pore pressure in accretionary complexes: Implications for taper angle and wedge mechanics, *J. Geophys. Res.*, *111*(B4), doi:10.1029/2005JB003990.
- Saffer, D. M., and C. Marone (2003), Comparison of smectite- and illite-rich gouge frictional properties: application to the updip limit of the seismogenic zone along subduction megathrusts, *Earth Planet. Sci. Lett.*, *215*(1–2), 219 – 235, doi:http://dx.doi.org/10.1016/S0012-821X(03)00424-2.
- Saffer, D. M., and H. J. Tobin (2011), Hydrogeology and mechanics of subduction zone forearcs: Fluid flow and pore pressure, *Annu. Rev. Earth Planet Sci.*, *39*(1), 157–186, doi:10.1146/annurev-earth-040610-133408.
- Saito, T., K. Ujiie, A. Tsutsumi, J. Kameda, and B. Shibazaki (2013), Geological and frictional aspects of very-low-frequency earthquakes in an accretionary prism, *Geophys. Res. Lett.*, *40*(4), 703–708, doi:10.1002/grl.50175.
- Schwartz, S., P. Allemand, and S. Guillot (2001), Numerical model of the effect of serpentinites on the exhumation of eclogitic rocks: insights from the Monviso ophiolitic massif Western Alps, *Tectonophysics*, *342*(1-2), 193 – 206, doi:http://dx.doi.org/10.1016/S0040-1951(01)00162-7, exhumation of high-pressure rocks: kinetic, thermal and mechanical constraints.
- Schwartz, S. Y., and J. M. Rokyosky (2007), Slow slip events and seismic tremor at circum-pacific subduction zones, *Reviews of Geophysics*, *45*(3), doi:10.1029/2006RG000208.
- Scott, D. R., and D. J. Stevenson (1984), Magma solitons, *Geophys. Res. Lett.*, *11*(11), 1161–1164, doi:10.1029/GL011i011p01161.

- Scott, D. R., and D. J. Stevenson (1986), Magma ascent by porous flow, *J. Geophys. Res.*, *91*(B9), 9283–9296, doi:10.1029/JB091iB09p09283.
- Screaton, E., D. Saffer, P. Henry, and S. Hunze (2002), Porosity loss within the underthrust sediments of the Nankai accretionary complex: Implications for overpressures, *Geology*, *30*(1), 19–22, doi:10.1130/0091-7613(2002)030<0019:PLWTUS>2.0.CO;2.
- Segall, P., and A. M. Bradley (2012), Slow-slip evolves into megathrust earthquakes in 2D numerical simulations, *Geophys. Res. Lett.*, *39*(18).
- Segall, P., A. M. Rubin, A. M. Bradley, and J. R. Rice (2010), Dilatant strengthening as a mechanism for slow slip events, *J. Geophys. Res.*, *115*, B12305, doi:10.1029/2010JB007449.
- Shelly, D. R., G. C. Beroza, S. Ide, and S. Nakamura (2006), Low-frequency earthquakes in Shikoku, Japan, and their relationship to episodic tremor and slip, *Nature*, *442*, 188–191, doi:10.1038/nature04931.
- Shelly, D. R., G. C. Beroza, and S. Ide (2007a), Complex evolution of transient slip derived from precise tremor locations in western Shikoku, Japan, *Geochem. Geophys. Geosyst.*, *8*, Q10014, doi:10.1029/2007GC001640.
- Shelly, D. R., G. C. Beroza, and S. Ide (2007b), Non-volcanic tremor and low-frequency earthquake swarms, *Nature*, *446*, 305–307, doi:10.1038/nature05666.
- Shen, Z.-K., Q. Wang, R. Bürgmann, Y. Wan, and J. Ning (2005), Pole-tide modulation of slow slip events at circum-pacific subduction zones, *Bulletin of the Seismological Society of America*, *95*(5), 2009–2015, doi:10.1785/0120050020.
- Shibazaki, B., and Y. Iio (2003), On the physical mechanism of silent slip events along the deeper part of the seismogenic zone, *Geophys. Res. Lett.*, *30*(9), 1498, doi:10.1029/GL017047.
- Shibazaki, B., and T. Shimamoto (2007), Modeling of short-interval silent slip events in deeper subduction interfaces considering the frictional properties at the unstable-stable transition regime, *Geophys. J. Int.*, *171*, 191–205, doi:10.1111/j.1365-246X.2007.03434.x.
- Shreve, R. L., and M. Cloos (1986), Dynamics of sediment subduction, melange formation, and prism accretion, *J. Geophys. Res.*, *91*(B10), 10,229–10,245.

- Skarbek, R. M., and A. W. Rempel (2013), Thermal consolidation with chemical dehydration reactions: Pore pressure generation in the slow slip region of subduction zones, in *Poromechanics V: Proceedings of the Fifth Biot Conference on Poromechanics*, edited by C. Hellmich, B. Pichler, and D. Adam, pp. 499–506, American Society of Civil Engineers, Reston, VA, doi:10.1061/9780784412992.059.
- Skarbek, R. M., and D. M. Saffer (2009), Pore pressure development beneath the décollement at the Nankai subduction zone: Implications for plate boundary fault strength and sediment dewatering, *J. Geophys. Res.*, *114*(B7), doi:10.1029/2008JB006205.
- Skarbek, R. M., A. W. Rempel, and D. A. Schmidt (2012), Geologic heterogeneity can produce aseismic slip transients, *Geophys. Res. Lett.*, *39*(21), doi:10.1029/2012GL053762.
- Smith, G., L. McNeill, T. J. Henstock, and J. Bull (2012), The structure and fault activity of the Makran accretionary prism, *J. Geophys. Res.*, *117*, B07407, doi:2012JB009312.
- Spiegelman, M. (1993a), Flow in deformable porous media. part 1 simple analysis, *Journal of Fluid Mechanics*, *247*, 17–38, doi:10.1017/S0022112093000369.
- Spiegelman, M. (1993b), Flow in deformable porous media. part 2 numerical analysis - the relationship between shock waves and solitary waves, *Journal of Fluid Mechanics*, *247*, 39–63, doi:10.1017/S0022112093000370.
- Spiegelman, M. (1993c), Physics of melt extraction: Theory, implications and applications, *Phil. Trans. R. Soc. Lond. A.*, *342*(1663), 23–41, doi:10.1098/rsta.1993.0002.
- Spinelli, G. A., and D. M. Saffer (2004), Along-strike variations in underthrust sediment dewatering on the Nicoya margin, Costa Rica related to the updip limit of seismicity, *Geophys. Res. Lett.*, *31*(4), doi:10.1029/2003GL018863.
- Sugioka, H., T. Okamoto, T. Nakamura, Y. Ishihara, A. Ito, K. Obana, M. Kinoshita, K. Nakahigashi, M. Shinohara, and Y. Fukao (2012), Tsunamigenic potential of the shallow subduction plate boundary inferred from slow seismic slip, *Nat. Geosci.*, *5*(6), 414–418, doi:10.1038/ngeo1466.
- Suppe, J. (2007), Absolute fault and crustal strength from wedge tapers, *Geology*, *35*(12), 1127–1130, doi:10.1130/G24053A.1.
- Tenthorey, E., and S. F. Cox (2003), Reaction-enhanced permeability during serpentinite dehydration, *Geology*, *31*(10), 921–924, doi:10.1130/G19724.1.

- Thomas, A. M., R. M. Nadeau, and R. Bürgmann (2009), Tremor–tide correlations and near-lithostatic pore pressure on the deep San Andreas fault, *Nature*, *462*(7276), 1048–1051.
- Tibi, R., D. A. Wiens, and X. Yuan (2008), Seismic evidence for widespread serpentized forearc mantle along the Mariana convergence margin, *Geophys. Res. Lett.*, *35*(13), doi:10.1029/2008GL034163, 113303.
- Tobin, H. J., and M. Kinoshita (2006), NanTroSEIZE: The IODP Nankai Trough Seismogenic Zone Experiment, *Sci. Drill.*, *2*, 23–27, doi:10.2204/iodp.sd.2.06.2006.
- Tobin, H. J., and D. M. Saffer (2009), Elevated fluid pressure and extreme mechanical weakness of a plate boundary thrust, Nankai Trough subduction zone, *Geology*, *37*(8), 679–682, doi:10.1130/G25752A.1.
- Tréhu, A. M., J. Braunmiller, and J. L. Nabelek (2008), Probable low-angle thrust earthquakes on the Juan de Fuca-North America plate boundary, *Geology*, *36*(2), 127–130, doi:10.1130/G24145A.1.
- Tsuji, T., H. Tokuyama, P. Costa Pisani, and G. Moore (2008), Effective stress and pore pressure in the Nankai accretionary prism off the Muroto Peninsula, southwestern Japan, *J. Geophys. Res.*, *113*(B11), doi:10.1029/2007JB005002.
- Walder, J., and A. Nur (1984), Porosity reduction and crustal pore pressure development, *J. Geophys. Res.*, *89*(B13), 11,539–11,548, doi:10.1029/JB089iB13p11539.
- Wallace, L., S. Henrys, P. Barnes, D. Saffer, H. Tobin, N. Bangs, R. Bell, and the Hikurangi Margin Working Group (2011), Multiphase drilling project: Unlocking the secrets of slow slip by drilling at the northern Hikurangi subduction margin, New Zealand, *IODP Proposal 781-MDP*.
- Wang, K., and Y. Hu (2006), Accretionary prisms in subduction earthquakes cycles: The theory of dynamic Coulomb wedge, *J. Geophys. Res.*, *11*, B06410, doi:10.1029/2005JB004094.
- Wang, W.-H., and T. fong Wong (2003), Effects of reaction kinetics and fluid drainage on the development of pore pressure excess in a dehydrating system, *Tectonophysics*, *370*(1-4), 227 – 239, doi:http://dx.doi.org/10.1016/S0040-1951(03)00188-4, physical Properties of Rocks and other Geomaterials, a Special Volume to honour Professor H. Kern.
- Wech, A. G., and K. C. Creager (2007), Cascadia tremor polarization evidence for plate interface slip, *Geophys. Res. Lett.*, *34*, L22306, doi:10.1029/2007GL031167.

- Wech, A. G., and K. C. Creager (2008), Automated detection and location of cascadia tremor, *Geophys. Res. Lett.*, *35*, L20302, doi:10.1029/2008GL035458.
- Whitham, G. B. (2011), *Linear and nonlinear waves*, John Wiley & Sons.
- Wilson, C. R., M. Spiegelman, P. E. van Keken, and B. R. Hacker (2014), Fluid flow in subduction zones: The role of solid rheology and compaction pressure, *Earth Planet. Sci. Lett.*, *401*(0), 261 – 274, doi:http://dx.doi.org/10.1016/j.epsl.2014.05.052.
- Wong, T.-F., S.-C. Ko, and D. L. Olgaard (1997), Generation and maintenance of pore pressure excess in a dehydrating system 2. Theoretical analysis, *J. Geophys. Res.*, *102*(B1), 841–852, doi:10.1029/96JB02484.
- Yamasaki, T., and T. Seno (2003), Double seismic zone and dehydration embrittlement of the subducting slab, *J. Geophys. Res.*, *108*(B4), doi:10.1029/2002JB001918, 2212.
- Yuan, X., S. Sobolev, R. Kind, O. Oncken, G. Bock, G. Asch, B. Schurr, F. Graeber, A. Rudloff, W. Hanka, et al. (2000), Subduction and collision processes in the central andes constrained by converted seismic phases, *Nature*, *408*(6815), 958–961, doi:10.1038/35050073.
- Zhao, W. L., D. M. Davis, F. A. Dahlen, and J. Suppe (1986), Origin of convex accretionary wedges: Evidence from Barbados, *J. Geophys. Res.*, *91*(B10), 10,246–10,258, doi:10.1029/JB091iB10p10246.